Fabrication and characterization of direct and inverse opals for the manipulation of spontaneous emission in conjugated polymers

Tecla Arcidiacono

A dissertation submitted for the degree of Doctor in Philosophy

Department of Physics and Astronomy

London Centre for Nanotechnology

University College London

I, Tecla Arcidiacono, confirm that the work presented in this thesis is my own. Where information has been derived from other sources and work which has formed part of jointly-authored publications has been used I confirm that this has been indicated in the thesis.

August, 2020

Supervisor: Prof Franco Cacialli

Department of Physics and Astronomy and London Centre for Nanotechnology, University College London

Second Supervisor: Dr. Tracey Clarke,

Department of Chemistry, University College London

To my brother,

My strength and my love.

To my family.

Acknowledgments

First and foremost I would like to thank Prof. Franco Cacialli for the opportunity to work on this interesting project, for inspiration and guidance throughout my PhD. I would also like to express my gratitude to my second supervisor, Dr. Tracey Clarke, for her support and advices.

A special thanks goes to Prof. Davide Comoretto for his excellent guidance and mentorship throughout my secondment at University of Genova. He has been a constant source of motivation and encouragement for me. My sincere thanks goes also to Dr. Roman Kranhe for all the fruitful discussions I had with him, which always gave me a sense of direction in my research.

Another big thanks to Prof. Giuseppe Barillaro, Dr.Stefano Mariani, Prof. Harry L. Anderson, and all the people involved in the SYNCHRONICS project for the collaborations that made this project possible. In particular, I would like to thank my F9 mates Dr. Giovanni Cotella, Dr. Alex Rapidis, Dr. Alessandro Minotto, Dr. Giuseppe Carnicella, Dr. Andrea Zampetti, Dr. Giuseppe Paternó, Dr. Luca Santarelli, and Dr. Valentina Robbiano for the good time I had at UCL.

A special thanks goes to Dr. Bruno Tomasello for inspiring scientific discussions, for his support and friendship along the way.

Last but certainly not least, I thank my family for their continuous love and encouragement, and for their immense support during all of my life.

Research institutions & funding bodies

Abstract

In this work I investigated and improved a technique, known as vertical method, for growing synthetic opals by means of colloidal self-assembly of polymeric microparticles. This enables an unprecedentedly easy tuning of the opal photonic bands and thus enhanced control of the radiative properties of conjugated polymers after their infiltration into such photonic structures.

The first part of the thesis is dedicated to direct opals defined as a close-packed array of spherical particles. In particular, I present a study of the optical response of polystyrene opals across an extended energy range ($0.8 < a/\lambda < 1.8$, where a is the lattice parameter and λ is the wavelength of light), which I achieved by adopting the aforementioned vertical method technique. Furthermore, in addition to discussing the conventional photonic stop band (PSB), I highlight the high-energy photonic bands associated to the Van Hove singularities which demonstrate the fcc arrangement of the microparticles signalling the high-quality standard of fabricated opals.

The second part of the work is focused on inverse opals, namely a close-packed array of spherical voids. This is formed by co-growing a sacrificial opal template with a material of high refractive index (i.e. silica) and the removal of the spheres by calcination. Typically, the central frequency of the PSB is tuned by changing the sphere diameters of the opal template. In contrast, when keeping the sphere diameters fixed, I found that I could blue-shift the PSB by ~100 nm by varying the SiO_2/colloidal ratio.

To verify the performance of the photonic crystals obtained, I studied the spontaneous emission of luminescent organic polymers (i.e. PDPV, and the conjugated polyrotaxane $PDV_{10}Li$ β-CD) after their infiltration into the opals. I achieved, respectively for direct and inverse opals, a strong reshaping of the photoluminescence and a modification on the value of the radiative constant.

Impact statement

Photonic crystals (PhCs) are materials with highly ordered structures whose colours depend on the angle of observation. The angle-dependent coloration does not result from pigmentation but it is rather due to the interaction between light and micro/nanostructures with a periodicity similar to the wavelength of the light. This phenomenon is known as iridescence. Iridescent materials, ubiquitous in nature, can be found in gemstones, butterflies, and in many other creatures. PhCs are characterised by their dielectric periodicity, which determines the modes of propagation of photons. The ability of manipulating light by means of PhCs results from the occurrence of a *photonic stop band* (PSB), which, because of Bragg diffraction, inhibits light propagation. The majority of PhCs has a pseudo PSB capable of preventing the flow of photons along only specific directions. However, by increasing the dielectric contrast of the PhCs, the PSB can evolve into a full PSB that forbids light propagation in all directions.

The presence of the PSB and the possibility to tune its position in the visible spectrum, as well as the advantage of inhibiting or enhancing spontaneous emission, make PhCs good candidates for several technological applications such as optoelectronics and telecommunications, but also for storing and generating energy. For these reasons they are extensively used as optical devices including waveguides, lasers, light emitting diodes and filters, and also as dye sensitized solar cells and Li-ion batteries. Moreover, thanks to their interconnected porosity, PhCs are exploited as sensors and bio-sensors, as well as drug deliverers and scaffolds for tissue regeneration.

The attractive potentialities of photonic crystals stimulated the development of several bottom-up and top-down fabrication methods, including sophisticated and expensive lithography techniques. *Self-assembly* methods are still intensively studied,

however, because of their affordable costs and the natural tendency of particles to self-assemble. Among these, the *vertical deposition* method via evaporation leads to structures of very high quality compared to other self-assembled strategies. It relies on capillarity forces for driving particles on a substrate that is vertically removed from a colloidal solution. This is how synthetic *opals* are made: three-dimensional photonic crystals generated by vertical deposition of micro-particles, for example silica, or polymeric, as later discussed in this thesis. Synthetic opals are widespread in the study of spontaneous emission manipulation. This is mostly due to their ability to straightforwardly incorporate active materials (e.g. metal nanoparticles, semiconductor nanocrystals, conjugated polymers) by means of infiltration, co-growth or evaporation techniques.

Depending on their structure, synthetic opals can be generally classified as *direct* or *inverse*. The former refers to an ensemble of closely packed solid spheres, whilst the latter to an ensemble of closely empty spheres. In this thesis, the optical response of fluorescent direct opals is investigated across an energy range that includes the PSB, as well as photonic bands of more complex diffraction phenomena. On the other hand, inverse opals are tackled by studying the correlation between the modulation of their lattice constant and the position of the photonic stop band in the spectrum. The results obtained demonstrate the strength of self-assemble techniques for manipulating the optical properties of photonic crystals.

Contents

List of figures

Figure 3.6. Schematic representation of the diffusion of an exited state between adjacent molecules via (a) Förster and (b) Dexter mechanism.

Figure 3.7. Jablonski diagram. Schematic representation of the molecular energy levels and of the possible transitions between them. On the right, the speed of the radiative e non-radiative relaxation process is illustrated.

Figure 3.8. The diagram shows the Franck-Condon principle. The absorption transitions are represented by vertical orange arrows from the ground state, S_0, to the exited state, S_1, potential energy curve, while the emission transition by vertical green arrows from the S_1 to the S_0 energy level. The vibrational wave functions for each state are depicted in grey. Adapted from ref. [2].

Figure 3.9. Chemical structure of PDPV, poly(4-4'-diphenylene diphenylvinylene).

Figure 4.1. Schematic representation of molecular recognition due to hydrogen bonding N-H···O and N-H···N [30].

Figure 4.2. Representation of two supramolecular systems: (a) a molecular tweezer made of two rings (i.e. crown ether) connected by a central unit -N=N-. If irradiated by light, the molecule changes structure, passing from trans to cis. This allows the two rings to get closer and therefore act as a trap for potassium ion; (b) a catenane made of two interlocked macrocycles, A and B having two sites of bonding for the cupper ion Cu^+, A1 and B1. If the Cu^+ is electrochemical oxidised, the ring A will rotate by 180° so that the Cu^{++} will interact with A2 and B1. The reduction of the Cu^{++} into Cu^+ leads to the initial structure of the catenane. [30].

Figure 4.3. Schematic representation of rotaxane (a) and polyrotaxane (b) structures [34, 35].

Figure 4.4. Schematic representation of linear (a) and rotating (b) movement of polyrotaxane [30].

Figure 4.5. chemical structure of the PDV.Li $\subset \beta - CD$ (a); Time-integrated emission spectra of PDV.Li solution at 5×10^{-2} mgml^{-1} (open circle) 1×10^{-4} mgml^{-1} (open triangles) and of all the solutions of the unthreaded polymer (b); time-dependent decays of solutions of PDV.Li $\subset \beta - CD$ (top panel), and of unthreaded polymers (bottom panel). Insert: evolution of the photoluminescence quantum efficiency ϕ (%) as a function of concentration [47].

Figure 4.6. Time-integrated emission spectra of PDV.Li solution (5×10^{-2} mgml^{-1}) depending on TR. Insert: average emission energy extracted from the spectra [48].

Figure 4.7. Absorption and photoluminescence spectra of thin film of the polyrotaxane (solid lines) and of the non-threaded chain (dashed lines), spun-coated on spectrosil substrate. Adapted from ref. 49

Figure 5.1. Schematic representation of an fcc lattice (left), the two planes (111) within the fcc cell (centre), and the Brillion zone (right) associated to the fcc structure.

Figure 5.2. Band structure calculated along the ΓL direction in reciprocal space for an artificial opal consisting of polystyrene spheres (top). ΓL bands are highlighted with thick lines. Transmission (middle) and reflection (bottom) spectra at normal incidence for an artificial opal (ref. 62).

Figure 5.3. (a) Schematic representation of the vertical method. The PS-NPs self-assemble in a face-cantered-cubic array at the interface between the water meniscus and the glass substrate. (b) Experimental set-up for opal fabrication (photo by Dr. Valentina Robbiano). (c) AFM image of opals based on PS-NPs with a diameter of 260 nm.

Figure 5.4. Molecular structure of the polyrotaxane PDV$_n$Li $\beta - CD$, average of repeat unit n = 10, and threading ratio = 2 (top). Absorption (black line), and emission (red line) spectra of a spin-coated film of PDV$_{10}$Li $\beta - CD$ (bottom).

Figure 5.5. Schematic representation of the polystyrene sphere/polyrotaxane co-growth. The PS-NPs self-assemble at the interface between the meniscus of the aqueous solution and the glass substrate, while the $PDV_{10}Li$ β – CD macromolecules fill the fcc voids (a). AFM image of luminescent opals based on PS-NPs with a diameter of 200 nm (b).

Figure 5.6. Microscope images (magnification 10 x) of bare and loaded opal by dip coating (a), drop casting (b) and femtojet methods (c)

Figure 5.7. (a) Schematic representation of the bifurcated fibre used for normal reflection, and (b) the set-up used for angle-dependent transmission. The grey circle represent a large-area rotating breadboards (goniometers).

Figure 5.8. Schematic representation (left) and photo (right) of the set-up used for angle dependent PL. The grey circle represent the goniometers, the sample (S) and the laser (L) are placed on the optical table, while the detector (F_d) is placed on the goniometers, so it can rotate..

Figure 5.9. Normal reflectance spectra of polystyrene opals made with different sphere diameters (d = 220, 260, 300 and 340 nm) (a); plot of the PSB and high-energy bands peaks as a function of the sphere diameters (b).

Figure 5.10. Legend of the opal region analysed by reflectance measurement (a), normal-reflectance spectra of opals base on polystyrene nanoparticles with diameters of 220 nm (b), 260 (c), 300 nm (d) and 340 nm (e).

Figure 5.11. Angle-dependent transmission spectra of 260 nm (left), 300 nm (centre), and 340 nm (right) opals. The black arrows show the PSB trend by changing the angles of the incidence light, while the red arrows are representative of the high-energy band tendency.

Figure 5.12. Emission spectra of a $PDV_{10}Li$ β – CD spin-coated film (black curve) with, superimposed, the normal reflectance spectra (red curve) of a bare opal with nanoparticles of 200 nm of diameters.

Figure 5.13. (a) Normal reflectance of bare (red curve) and rotaxinated opal (black curve). (b) Normal reflectance collected in different spot of the rotaxinated opal surface.

Figure 5.14. Emission spectra of the spin-coated pure polyrotaxane (black curve) and of the rotaxinated melted opal, i.e. reference (blue curve) collected at 0° (normal incidence) (a); spectral overlap between the emission and the normal reflectance curves for co-growth opal made with spheres having diameter 200 nm, black and red curves, respectively (b).

Figure 5.15. Left: PL spectra of the rotaxinated opal before (solid line) and after (dashed line) the thermal treatment, at different angles of light collection; Right: Ratio between the angle-dependent emission of the co-growth opal (PhC) and the reference opal (Ref).

Figure 5.16. Legend of the analysed rotaxinated opal regions (a-i) by reflectance measurement (a), normal-reflectance spectra of opals base on polystyrene nanoparticles with diameters of 260 nm (b), 300 nm (c), and 340 nm (d).

Figure 5.17. Reflectance spectra collected at normal incidence to respect the (111) plane (top graph) of rotaxinated opals made with spheres having a diameter of 260 nm (red line), 300 nm (black line), and 340 nm (blue line). Normal reflectance peaks as a function of the sphere diameters (bottom graph). The spectra are reduced to the dimensionless unit a/λ(where a is the lattice parameter proportional to the spheres diameters, and λ is the wavelength of light).

Figure 5.18. Transmittance contour maps of three rotaxinated opals prepared with spheres having diameters of 260 nm (left), 300 nm (centre), and 340 nm (right)

respectively, as a function of both wavelength and incidence angle. The emission spectrum of the polyrotaxane in a melted opal is also shown as a white line. The blue and the black stars indicate respectively the peak of the PSB and the high energy bands as a function of the angle of the incidence of light.

Figure 5.19. Angle-dependent PL spectra (black curves) of rotaxinated opals based on different sphere diameters, 260 nm (left), 300 nm (centre), and 340 nm (right), overlapped with their angle-dependent transmission curves (red lines). At 0° of incident light the reflectance spectra (blue lines) have been added to better visualise the photonic high-energy bands.

Figure 6.1. Schematic representation of the evaporative co-assembly technique for inverse opals preparation. The PS-NPs self-assemble in a face-centred-cubic array at the interface between the colloidal/TEOS meniscus and the glass substrate. The silica precursor fill the voids between the spheres generating the inorganic matrix. The inverse opals structure are obtained after sample calcination at 500°C for 2 hours (a). SEM image of an inverse opal prepared by vertical deposition (b). The thickness of the resulted structure is 5.5 μm.

Figure 6.2. Reflectance curves of silica inverse opals prepared by varying the volume of the silica precursor, TEOS (a). Peak of the photonic band gap as a function of the TEOS contents (b).

Figure 6.3. Curves of normal reflectance collected in different spots of two inverse opals prepared using a colloidal solution containing 90 μL and 35 μL of silica precursor (TEOS), respectively. The inserts are a schematic representation of the samples investigated, the letters identify the area of the inverse opals undergo examination.

Figure 6.4. SEM images of inverse opals prepared by colloidal solution containing 15 μL (a), 25 μL (b), 35 μL (c), and 45 μL (d) of silica precursor (TEOS). For each structure the average diameter of the voids, <d>, has been measured.

Figure 6.5. Schematic representation of the infiltration method used to fill the voids of the silica inverse opal. The picture shows also the chemical structure of the conjugated active polymer, PDPV.

Figure 6.6. Normal reflection spectra of tuned and detuned inverse opal plotted together with the PL curve of a spin-coated film of PDPV (a); Comparison between the PL spectra of the PDPV into the inverse opals and of a PDPV spin-coated film of PDPV (b). The spectra are normalised.

Figure 6.7. PL spectra of tuned (black curve) and detuned (blue curve) opals together with the transmittance (red curve) of the luminescent tuned opal. The PL spectra were collected by increasing the collection angle from 0° to 30°, while the transmittance spectra by increasing the angle of the incidence beam.

Figure 6.8. Ratio between the angle-dependent emission of the infiltrated tuned inverse opal (PhC) and the infiltrated detuned opal (reference).

Figure 6.9. Schematic representation of the set-up used to infiltrate and characterised invers opals. The sample is located in a flow-cell connected with the reflectance probe and with a syringe pump for the flowing of the buffer and the analytes (a). Reflectance spectra of the inverse opals in air (blue line) and of the same sample into the flow-cell and infiltrated with the acetate buffer (green line) and with 1000 ppm of BSA (yellow line).

Figure 6.10. Time resolved IAW- IAW0 signal upon injection of BSA 1000 ppm. The signal-to-noise ratio is 83 (a). Time resolved IAW- IAW0 value for different concentration of BSA, 100 ppm (green sector), 200 ppm (yellow sector), 500 ppm (blue

sector), and 1000 (ppm pink sector) (b). Fitting of the IAW- IAW0 values as a function

of the BSA concentrations (c).

List of tables

Chapter 1. Introduction

The rainbow is a quite common and yet very spectacular phenomenon in nature: a beautiful arc in the sky, displaying all colours of the visible spectrum of electromagnetic waves. Our chance to appreciate red fading into orange, orange fading into yellow, and so on, all the way down to violet, is possible from the combination of reflection, refraction and dispersion of light occurring in water droplets in

Figure 1.1. Rainbow (Turin, July 2020).

the atmosphere. Prior to beauty and pleasure themselves, colouration is a precious resource of the universe, which conveys, by means of electromagnetic waves, crucial information for creatures in our planet. Animals, for example, utilize colours to accomplish vital functions, such as identification, mating, environmental camouflage, defence and much more [3].

The sensation of colours arises from the combination of two main phenomena: (1) the interaction between light and matter and (2) the vision mechanisms of the eye. The material, the structure and the orientation of illuminated objects basically determine the frequencies of electromagnetic waves. These are then collected by the eyes, which, acting as a natural detector, decode the information about the frequencies and encode it for the brain in the perception of coloration. Depending on how light interacts with matter, colours in nature can be produced by pigments, photoluminescence and structural colours. *Pigments* are materials, which, because of selective quantum absorption, reflect only specific wavelengths of light, i.e. specific

colours. *Photoluminescence* (PL) results from the quantum-optical transition of a system (atoms, molecules, polymers or nanocrystals) which relaxes from an excited state to its ground state; the relaxation consist in emitting a photon whose wavelength corresponds to the energy difference between the initial and the final state. *Structural colours* differ profoundly from pigments or luminescent dyes. They are brighter, higher saturated, not affected by photobleaching and they result from complex interactions between visible light and micro/nano-structures. The optical processes originating in this unique colouration span from thin-layer and multi-layer interference to diffraction grating and scattering. Moreover, depending on the regularity of the structure, structural colours can be categorized as either iridescent or non-iridescent. Ordered structures generate iridescence, meaning that the perception of their colour changes depending on the angle of observation. On the other hand, disordered structures are non-iridescent, i.e. the appearance remains the same regardless of the angle of observation [4,5].

Figure 1.2. Assortment of pigment powders on sale (Medina of Chefchaouen, Morocco, February 2015).

In nature, an important source of iridescence is represented by *Photonic crystals* (PhCs), periodic structures of materials with different refractive index (see for example figure 1.3). Among all, *opals* are widespread PhCs in which refractive indexes are periodically ordered in the three spatial dimensions (3D). Depending on their structure, they can be defined as *direct* or *inverse*. Direct opals are ordered arrays of dielectric spheres, where air fills the voids in between them. Vice versa, inverse opals

are structures in which spherical voids are periodically arranged in a dielectric medium. An illustrative example is given at page 68 and 95.
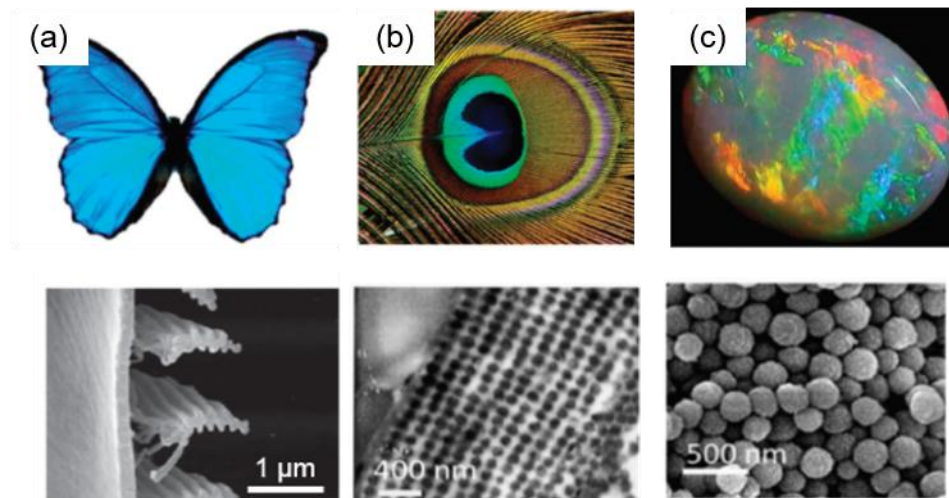
Figure 1.3. Examples of structural colours in nature. (a) Bright irridescence of *Morpho rhetenor* butterfly due to alternated lamellar structure of its wings. (b) The blue area of peacock feathers displays a periodic structure of melanin rods. (c) Natural opal gemstones is characterised by an array of silica spheres. Pictures (a), (b), and (c) are adapted with permission of ref 72.

Discovered in 1987 by Eli Yablonovitch and Sajeev John, respectively in ref. [6] and ref. [7], PhCs are characterised by very unique properties of light manipulation. When the dielectric periodicity is comparable to the wavelength of incident photons, light interacting with such structures is transmitted into the medium only for certain *bands* of frequency. The others frequencies are instead scattered outside the medium. If the scattered waves are in phase with each other, constructive interference is responsible for the "emergence" of a specific colour. On the contrary, if the waves are not in phase with each other, destructive interferences do not give colours. The wavelength of the scattered light can be estimated by using the Bragg-Snell law thoroughly explained at page 35 of this thesis.

The control of the propagation of light by photonic crystals is analogous to the control of the propagation of electrons by atomic crystals. Photonic band-gaps – frequency windows in which the propagation of photons through the crystal is forbidden

– are generated by the refractive index periodicity, similarly to how, in semiconductors, the electronic bands are generated by the electrical potential of the crystalline ions. The propagation of photons can be tuned by the "design" of the photonic band gap, hence by accurate engineering of the structural materials, by means of both their crystalline structure and their dielectric contrast. The efficiency of PhCs therefore depends on the materials themselves and on the fabrication methods for their crystalline arrangement.

Several studies demonstrate that PhCs are ideal candidates for providing control of photoluminescence of embedded materials [8,9]. For example, the photoluminescence can be completely suppressed by 3D photonic crystals if the frequencies of the incoming light beam is in resonance with the photonic band gaps [4]. In addition to suppression of light, PhCs are used to enhance the emission of dyes [10,11]. Among all, *luminescent conjugated polymers* are emitters that thanks to their optical and electronic properties can be used for different devices such as lasers, OLEDS, photovoltaic cells, and many more technological applications. Hence the control over their emission, for either suppression or enhancement, can importantly improve the performance of the photonic device. A class of conjugated polymers possessing high-performance optical and electrical properties is polyrotaxanes, supramolecular systems in which the conjugated chain is thread through cyclodextrin rings. These rings act as spacer between the chains, reducing or even completely inhibiting the quenching of the luminescence.

In this thesis, direct and inverse opals are studied as light manipulators of luminescent conjugated systems. The content of the remaining six chapters is summarised in the following. In **chapter 2**, I introduce the structure and the optical properties of photonic crystals, with particular emphasis on the generation of the photonic bands. By means of Maxwell's equations and Bragg-Snell law I expose the theories for the propagation of light in photonic crystals. In **chapter 3**, I discuss the

optical and electrical properties of conjugated polymers, as well as their applications. Additionally, I present previous works on the photophysics of the luminescent Poly(4-4'-diphenylene diphenylvinylene). In **chapter 4**, I study the chemical structures and the technological applications of supramolecular systems. I focus the attention on polyrotaxanes and on poly(4,4'-diphenylene vinylene) threaded through cyclodextrin rings, $PDV_{10}Li \ \beta - CD$. In **chapter 5**, I give a description of the *vertical deposition* technique for the fabrication of direct opals. I also study the optical properties of bare and luminescent opals, focusing on the effect of photonic bands on the emission of $PDV_{10}Li \ \beta - CD$. In **chapter 6**, I present a new strategy for the tuning of the photonic bands of inverse opals. The results demonstrate the strong efficiency of such strategy for employing inverse opals as light manipulators for conjugated polymers (i.e. PDPV), and as bio-sensors for the monitoring of bovine serum albumin (BSA). In the conclusions, **chapter 7**, I comprehensively discuss all the results obtained.

Chapter 2. Photonic crystals: ordered structures for manipulating light

This chapter gives an overview of the structure and of the optical properties of photonic crystals (PhCs). Their ability to control the radiative properties of luminescent materials is discussed, and the manipulation of Maxwell's equations is presented to understand how light propagate into the crystal array. Moreover, the Bragg-Snell law is studied for the case of 3D PhCs.

2.1 **Introduction to photonic crystals**

Photonic crystals (PhCs) are structures in which materials with different dielectric permittivity (ε) or refractive index, are periodically ordered in 1, 2, or 3 dimensions (see for example Figure 2.1). Due to the periodic modulation of ε, PhCs can completely control the radiative properties of luminescent materials and consequently manipulate the propagation of light [1,12]. In particular, PhCs with periodicity on the scale of visible light or near-infrared are of particular interest due to their technological applications such as optoelectronics, telecommunications, and biomedicine.
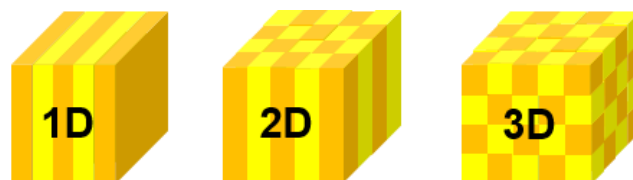
Figure 2.1. Schematic representation of one-dimensional (left), two-dimensional (centre), and three-dimensional (right) photonic crystals.

In order to understand how PhCs can afford control over the optical properties of materials, it is useful to exploit the analogy between photons inside a photonic crystal and the charge carriers inside a periodic (electronic) potential. The crystalline structure of electronic materials presents a lattice potential due to the periodical arrangement of atoms or molecules within the structure. The geometry of the lattice and the nature of the atoms set the conduction properties of the crystal. More in detail, the electrons, being quantum mechanical bodies, propagate as waves through the structure and occupy allowed energy levels, $E_n(\mathbf{k})$, which are characterised by two quantum numbers, n and k, where n is an integer number defined as band index (n = 1, 2, 3, …), while k can assume any value inside the range $-\left(\frac{\pi}{a}\right) < k < +\left(\frac{\pi}{a}\right)$ (where a is the lattice constant) depending on the crystal lattice. For each value of n, electrons can move in a continuum of energies between a maximum and a minimum value that are a function of k. The energies allowed for electron propagation are called the allowed band and the difference between the maximum and the minimum value of k is the bandwidth. Two consecutive bands can be totally or partially overlapped, and, more importantly, if the lattice potential is strong enough, they can be separated by a range of energy levels not allowed for electron propagation, the band gap.

Photonic crystals are the optical analogue of electronic materials, in which atoms or molecules are replaced by macroscopic media with different dielectric constants, and the periodic potential is replaced by a periodic index of refraction. If the dielectric constants are sufficiently different, and the light absorbed by the materials is minimal, then periodic modulation of ε can generate allowed and forbidden bands for the propagation of photons. Furthermore, as we will see in the next sections the range of allowed frequencies, $\omega_n(\mathbf{k})$, is labelled by a band index n and it is characterised by specific values of k, as in the case of electronic materials. Figure 2.2 shows how gaps open in both an electronic crystal (upper graphs) and a photonic material (lower graphs). The energy dispersion relation for an electron in vacuum is parabolic with no

gaps. When a periodic potential is present, gaps (see grey stripes in Figure 2.2) open creating forbidden energy levels for electrons propagation. Similarly, a periodic dielectric medium will present frequency regions where photons propagation is not allowed. The analogy between PhCs and electronic materials is possible by manipulating and casting the Maxwell's equations, which govern the photon propagation, in a single master equation that has a mathematical structure similar to the Schrodinger equation for electrons.
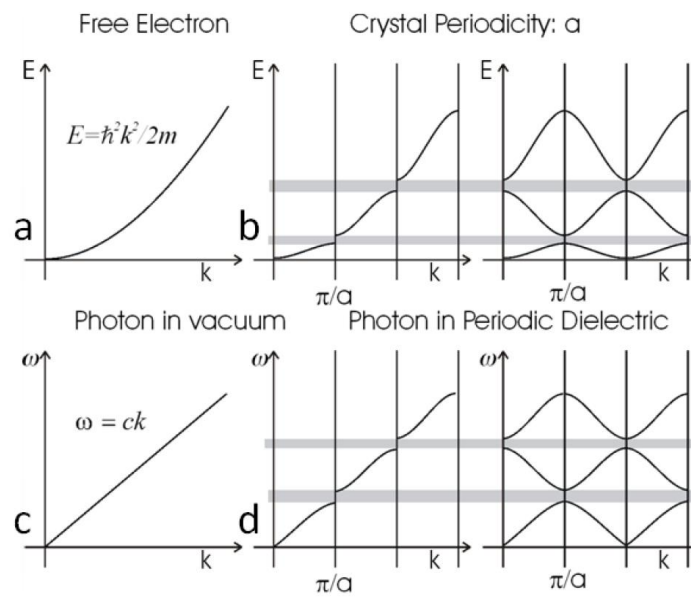
Figure 2.2. Dispersion relations for free electrons and inside a periodic potential (top) and for photons in vacuum and inside a periodic dielectric (bottom)[1].

Since the formation of forbidden and allowed bands is essentially caused by the refractions and reflections of light from all of the various interfaces of the PhCs, the Bragg-Snell law can be an advantageous method to understand the effect of the ε periodicity to the light propagation within PhCs (an accurate description can be found in section 2.3). However, in order to understand how the light propagates into a photonic crystal, the resolution of the master equation becomes essential. The next section explains how to use the Maxwell equations to obtain and solve the master equation useful to the work of the present thesis.

2.2 **The master equation**

The optical properties of photonic crystals can be described through the resolution of the macroscopic Maxwell Equations for a mixed dielectric medium. Assuming (i) a dielectric medium as composed of homogeneous dielectric regions as a function of the (Cartesian) position vector r, (ii) a small field strength in order to be in a linear regime, (iii) a macroscopic, isotropic and transparent material, so that the permittivity ε (**r**, ω) is the product between the vacuum permittivity ($\varepsilon_0 \approx 8.854 \times 10^{-12}$ Farad / m) and a scalar, real and positive dielectric function ε_r (**r**, ω), and that (iv) the dielectric constant is independent of frequency, ε (**r**) = $\varepsilon_0\varepsilon_r$ (**r**), the Maxwell Equations could be written as

$$\nabla \cdot \mathbf{E}(\mathbf{r},t) = \frac{\rho}{\varepsilon_r(\mathbf{r})\varepsilon_0}, \qquad\qquad \nabla \cdot \mathbf{H}(\mathbf{r},t) = 0, \qquad\qquad (2.1)$$

$$\nabla \times \mathbf{E}(\mathbf{r},t) = -\mu_0\mu(\mathbf{r})\frac{\partial\mathbf{H}(\mathbf{r},t)}{\partial t}, \quad \nabla \times \mathbf{H}(\mathbf{r},t) = \mathbf{J} + \varepsilon_r(\mathbf{r})\varepsilon_0\frac{\partial\mathbf{E}(\mathbf{r},t)}{\partial t}, \quad (2.2)$$

where **E** and **H** are the macroscopic electric and magnetic fields, ρ and **J** are the charge and current density, and μ_0 = 4π x 10^{-7} Henry / m and μ are the vacuum and the magnetic permeability, respectively. The $\nabla\cdot$ symbol denotes the divergence operator and it can be defined as the ratio between the net field flux (ϕ), which pass through a closed surface, and an infinitesimal and arbitrary volume, while the $\nabla\times$ symbol denotes the curl operator which express the ratio between the circulation (field magnitude per circular distance) and the area enclosed by the distance travelled by the field. In the assumptions listed above, linear and lossless materials are considered in order to use the simplest form of Maxwell's equations, however, no materials are perfectly linear and transparent. In ref. 1, perturbation theory is used to analyse the effect of small changes in the dielectric function on the modes and their frequencies, and it was found that for many realistic problems, the error in this approximation is negligible.

Maxwell's equations can be rewritten in a simple form if other restrictions for the mixed dielectric medium are considered, such as (i) it does not vary with time, (ii) it can be crossed by light but there are no sources of light inside it, (iii) it does not contain free charges or current, $\rho = 0$ and $J = 0$, and that (iv) for most dielectric materials of interest $\mu(\mathbf{r}) \approx 1$,

$$\nabla \cdot \mathbf{E}(\mathbf{r}, t) = 0 \qquad \qquad \nabla \cdot \mathbf{H}(\mathbf{r}, t) = 0 \qquad (2.3)$$

$$\nabla \times \mathbf{E}(\mathbf{r}, t) = -\mu_0 \frac{\partial \mathbf{H}(\mathbf{r}, t)}{\partial t} \qquad \nabla \times \mathbf{H}(\mathbf{r}, t) = \varepsilon_r(\mathbf{r})\varepsilon_0 \frac{\partial \mathbf{E}(\mathbf{r}, t)}{\partial t} \qquad (2.4)$$

E(r, t) and **H**(r, t) are functions of both time and space but due to the linearity of Maxwell's equations, the time dependence can be separated from the spatial dependence by using Fourier analysis, and **E**(r) and **H**(r) can consequently be written as harmonic modes

$$\mathbf{H}(\mathbf{r}, t) = \mathbf{H}(\mathbf{r})e^{-i\omega t}, \qquad (2.5)$$

$$\mathbf{E}(\mathbf{r}, t) = \mathbf{E}(\mathbf{r})e^{-i\omega t}, \qquad (2.6)$$

where ω is the angular frequency.

Therefore, by substituting the expressions of **E**(r, ω) and **H**(r, ω) of equations 2.5 and 2.6 into 2.3 and 2.4, the equation governing the mode profile for a given frequency can be found. In particular, by inserting the equations 2.5 and 2.6 into the divergence equations 2.3 we obtain that the electromagnetic waves are transverse. On the other hand, from the two curl equations 2.4 we can write

$$\nabla \times \mathbf{E}(\mathbf{r}) - i\omega\mu_0 \mathbf{H}(\mathbf{r}) = 0, \qquad (2.7)$$

$$\nabla \times \mathbf{H}(\mathbf{r}) + i\omega\varepsilon_r(\mathbf{r})\varepsilon_0 \mathbf{E}(\mathbf{r}) = 0. \qquad (2.8)$$

By dividing equation 2.8 by $\varepsilon(\mathbf{r})$, and then taking the curl and then using equation 2.7 to eliminate $\mathbf{E}(\mathbf{r})$, we can obtain a differential equation for $\mathbf{H}(\mathbf{r})$ called the Master equation or Helmholtz's equation:

$$\nabla \times \left(\frac{1}{\varepsilon(\mathbf{r})} \nabla \times \mathbf{H}(\mathbf{r}) \right) = \left(\frac{\omega}{c} \right)^2 \mathbf{H}(\mathbf{r}), \qquad (2.9)$$

where $c = \frac{1}{\sqrt{\varepsilon_0 \mu_0}}$

The master equation, together with the transversality requirement, gives us all the information about $\mathbf{H}(\mathbf{r})$ and $\mathbf{E}(\mathbf{r})$ as modes and frequencies, and consequently, it describes how the light propagates in a medium with a dielectric constant $\varepsilon\,(\mathbf{r})$.

For reasons of mathematical convenience, working with the magnetic field instead of the electric field is preferred for numerical calculations, and the most convenient methods to solve the master equation 2.9 is to consider this problem as an eigenvalue one. Consequently, we can define the left side of the master equation as an operator $\hat{\Theta}$ acting on $\mathbf{H}(\mathbf{r})$, so that the master equation will be:

$$\hat{\Theta}\, \mathbf{H}(\mathbf{r}) = \left(\frac{\omega}{c} \right)^2 \mathbf{H}(\mathbf{r}). \qquad (2.10)$$

The eigenvectors $\mathbf{H}(\mathbf{r})$ are the spatial patterns of the harmonic modes, and the eigenvalues $\left(\frac{\omega}{c} \right)^2$ are proportional to the squared frequencies of those modes. The operator $\hat{\Theta}$ is linear and it can be written as:

$$\hat{\Theta}\, \mathbf{H}(\mathbf{r}) \triangleq \nabla \times \left(\frac{1}{\varepsilon(\mathbf{r})} \nabla \times \mathbf{H}(\mathbf{r}) \right). \qquad (2.11)$$

Since the operator is linear, any linear combination of solutions must also be a solution. In addition, since $\hat{\Theta}$ is a Hermitian operator the eigenfunctions (i) have real and nonnegative eigenvalues for $\varepsilon > 0$, (ii) they are orthogonal, that means two

harmonic modes with different frequencies have an inner product of zero, (iii) they can be obtained by a variational principle, which state that a mode concentrates its electric-field energy in regions of high dielectric constant, and (iv) they may be catalogued by its symmetry properties. An accurate description and analysis of the Hermitian properties can be found in ref. 1.

An important feature of the master equation is the scale invariance. In other words, the electromagnetic field in dielectric media does not have a fundamental length, as it is for the Bohr radius in the electronic states. Consequently, unlike systems that show very different physical properties only for variation in their overall spatial scale, for photonic crystals, there is no fundamental constant with the dimensions of length. By considering two systems with a dielectric configuration that differs only for some scale parameter s(ε'($\mathbf{r}$) = ε($\mathbf{r}$/s)), the harmonic modes and frequency also differ for the scale parameter s($\mathbf{H}$'($\mathbf{r}$) = $\mathbf{H}$($\mathbf{r}$'/s), $\omega' = \frac{\omega}{s}$). This mean that the scale invariance permits to study structures in any convenient scale and then extend the results in every other region of interest.

Another interesting property linked to the invariance of scale is the lack of fundamental value for the dielectric constant. By considering two systems with a dielectric configuration that differs by a constant factor everywhere ($\varepsilon'(\mathbf{r}) = \frac{\varepsilon(\mathbf{r})}{s^2}$), the harmonic modes $\mathbf{H}$($\mathbf{r}$) are the same for the two systems, but the frequencies are all scaled by a factor s (ω' = sω). Furthermore, by scaling ε by s^2 and also rescale coordinates by s, the ω is unchanged. In other words, using the same form of the Maxwell's equations it is possible to study warped and distorted structure.

2.3 **Symmetries and photonic band structure**

In a dielectric structure, the existence of symmetry provides a convenient method to classify the electromagnetic modes of that system. Photonic Crystals are

characterized by both continuous and discrete translational symmetry in the direction in which the medium is homogeneous and periodic, respectively.

Along the direction in which the medium is homogeneous, the system remains unchanged when everything is translated by the same distance **d**. For each **d**, we can associate a translation operator $\widehat{T_d}$ which acts on a generic function f(**r**) shifting its argument by **d**.

$$\widehat{T_d}\varepsilon(\boldsymbol{r}) = \varepsilon(\boldsymbol{r} - \boldsymbol{d}) = \varepsilon(\boldsymbol{r}). \qquad (2.12)$$

Systems with a continuous translation symmetry in the z-direction (the dielectric function is constant in the z-direction) are invariant under all of the $\widehat{T_d}$'s for that direction. The eigenfunctions of the translation operator are plane waves and the corresponding eigenvalue is e^{-ikd} , where $\mathbf{k} = k_x\hat{\mathbf{x}} + k_y\hat{\mathbf{y}} + k_z\hat{\mathbf{z}}$ is the wave vector from which is possible to classify the modes

$$\widehat{T_d}e^{ikz} = e^{ik(z-d)} = e^{-ikd}e^{ikz}. \qquad (2.13)$$

Extending the argument to 3D-homogeneous systems (ε (**r**) = constant in all directions), the modes will have the form

$$\mathbf{H_k}(\mathbf{r}) = H_0\,e^{i\mathbf{k}\cdot\mathbf{r}}, \qquad (2.14)$$

where H_0 is any constant vector. These plane waves polarized in the direction of H_0 are solutions of the master equation with eigenvalues $\left(\frac{\omega}{c}\right)^2 = \frac{|k|^2}{\varepsilon}$ and for the transversality requirement we have that $\mathbf{k} \cdot H_0 = 0$.

On the other hand, where the PhCs have a discrete translational symmetry, the system remains unchanged only for a distance that is multiple of some fixed step length. The dielectric unit that is repeated is known as the unit cell and its width is the

lattice constant, *a*. The linked step vector is the primitive lattice vector $\mathbf{a} = a_x\hat{\mathbf{x}} + a_y\hat{\mathbf{y}} + a_z\hat{\mathbf{z}}$. Because of this discrete symmetry in three dimensions, we have

$$\varepsilon\,(\boldsymbol{r}) = \varepsilon\,(\boldsymbol{r} + \boldsymbol{R}), \qquad\qquad (2.15)$$

where **R** is an integer multiple of **a** (**R** = ℓ**a** where ℓ is an integer), and the electromagnetic modes of a PhCs can be written as a Bloch state [1,13,14]

$$\mathbf{H}_{\mathbf{k}}(\mathbf{r}) = e^{i\mathbf{k}\cdot\mathbf{r}}\boldsymbol{u}_k(\boldsymbol{r}), \qquad\qquad (2.16)$$

where **u$_k$(r)** is a periodic function on the lattice $\boldsymbol{u}_k(\boldsymbol{r}) = \boldsymbol{u}_k(\boldsymbol{r} + \boldsymbol{R})$, and again **k** identifies the modes. However, all of the modes characterised by wave vectors of the form $k + m\left(\frac{2\pi}{a}\right)$ (where *m* is an integer), have the same eigenvalues and consequently they form a degenerate set of periodic frequencies where *k* can be selected within the range $-\left(\frac{\pi}{a}\right) < k < +\left(\frac{\pi}{a}\right)$, called the Brillouin zone.

Inserting the Block state 2.16 into the master equation 2.10, all the information about the modes can be obtained.

$$\widehat{\Theta}\,\mathbf{H}_k = \left(\frac{\omega(\boldsymbol{k})}{c}\right)^2\mathbf{H}_k, \qquad\qquad (2.17)$$

$$\widehat{\Theta}\,e^{i\mathbf{k}\cdot\mathbf{r}}\boldsymbol{u}_k(\boldsymbol{r}) = \left(\frac{\omega(\boldsymbol{k})}{c}\right)^2 e^{i\mathbf{k}\cdot\mathbf{r}}\boldsymbol{u}_k(\boldsymbol{r}). \qquad\qquad (2.18)$$

However, due to the transversality and the periodic boundary condition, it is enough to solve the eigenvalue problem just for a single unit cell of the PhCs. The result is a family of continuous functions, ω_n(**k**), labelled by a band index *n* which indicates the discretely spaced frequencies. By studying these functions, known as band structure of the photonic crystals, it is possible to predict the optical (transmission and reflection) properties of such structures.
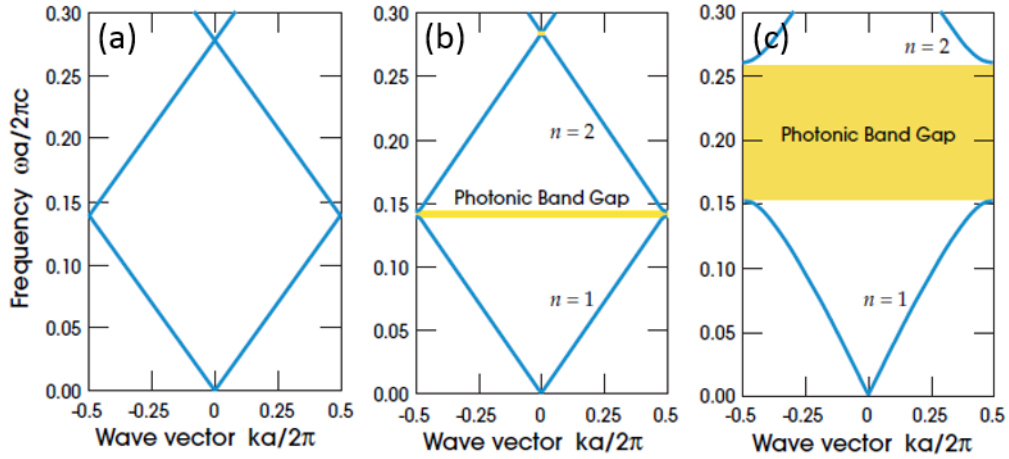
Figure 2.3. Photonic band structure for three different multilayer film characterized by different dielectric contrast. The plot on the left is for homogeneous mediums, the central plot is for low dielectric contrast structures, and the bands on the right is for high dielectric contrast multilayers [1].

In figure 2.3, $\omega_n(\mathbf{k})$ for three simplest photonic crystals (multilayer film) are plotted. All media are characterised by a periodicity of *a*, but present a different dielectric contrast. The plot "a" is for a homogeneous dielectric medium that is all the layers have the same ε, the plot "b" is for a structure with very low ε contrast $(\left(\frac{\varepsilon_{higher}}{\varepsilon_{lower}}\right) \sim 1)$, and the plot "c" is for a structure with a much higher dielectric contrast $(\left(\frac{\varepsilon_{higher}}{\varepsilon_{lower}}\right) > 10)$.

It is clear that the presence of a dielectric contrast $(\left(\frac{\varepsilon_{higher}}{\varepsilon_{lower}}\right) \neq 1)$ generates a gap in frequencies at either the Brillouin zone's edge or its centre. In that gap, there is no allowed modes for the photonic crystals. This frequencies gap is called "photonic band gap" and it enlarges considerably as the dielectric contrast increases. The bands above (n = 2) and below (n = 1) the gap can be distinguished by where the energy of their mode is concentrated, indeed the study of the electromagnetic variational theorem suggests that low-frequency modes concentrate their energy in the high-ε regions, while the high-frequency modes in the low- ε regions. Often, in photonic crystals the low- ε regions are made by ambient air, consequently, the band above the

photonic band is called air band, and the band below the gap is known as dielectric band.
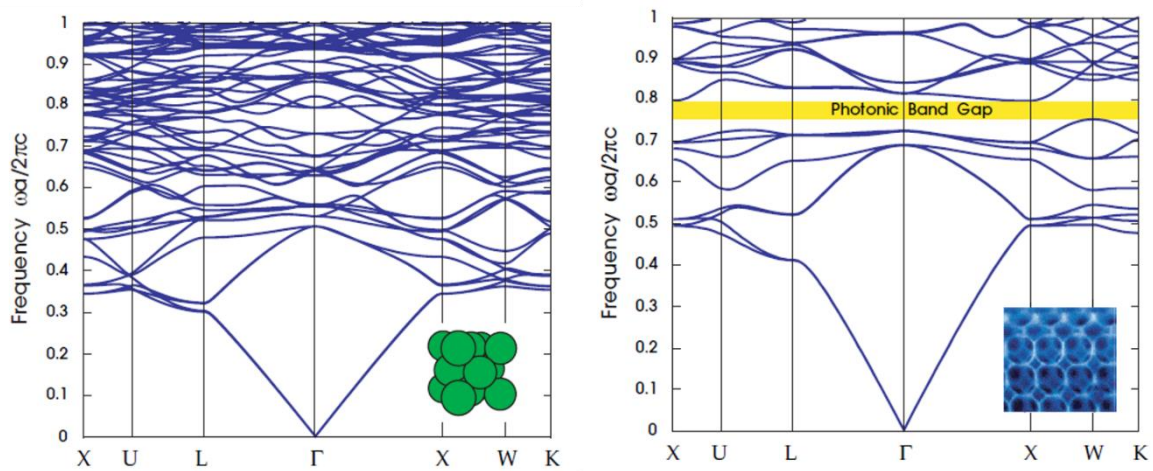
Figure 2.4. Left - The photonic band structure for the lowest-frequency electromagnetic modes of an opal: face-centred cubic (fcc) lattice of close-packed dielectric spheres in air (inset). Note the absence of a complete photonic band gap. Right – The photonic band structure for the lowest bands of an inverse opal: fcc lattice of close-packed air sphere in dielectric (insert). Note the presence of a complete photonic band gap (yellow)[1].

The appearance of the photonic band gap is also related to the light polarization. If the photonic band gap exists for all the light polarization and in all the k directions then it is called a "complete-photonic band gap" or just PBG. On the other hand, we call "pseudo-photonic stop band" or just PSB the band gap opened in only one crystallographic direction. For a higher dielectric contrast (i.e. > 10) in at least one polarization, 1D and 2D PhCs always display a PBG, whereas for 3D structures obtaining a complete gap is more challenging, unless they present structures like face-centred cubic (fcc), diamond, Yablonovite or woodpile. For example, the left graph of figure 2.4 shows the band structure for an fcc lattice of close-packed high-dielectric spheres (ε =13) in air. Although the dielectric contrast is very large, there is no PBG, but only a PSB between the first and the second bands, along the ΓL direction of the Brillouin zone. On the other hand, in the right graph of figure 2.4 the PBG gap of an fcc inverse opal structure can be observed.

The next section explains why and how Bragg-Snell law is an easy and direct method to estimate the photonic band gap position in the transmission and reflectance spectra. First, the ray reflection and the ray diffraction are considered as isolated events and Bragg's and Snell's equations are illustrated separately. Then, Bragg-Snell equation is obtained by combining the diffraction and reflection phenomena and by adapting them to the case of the photonic crystals.

2.4 **Bragg-Snell Law**

By considering PhCs as one-dimensional planar structures, it is possible to use Bragg-Snell law for incident light as a simple model to describe the optical phenomena due to the ε modulation.

In 1912, Max von Laue suggested that a crystal lattice composed of atoms might have a spacing small enough to create a diffraction pattern using x-ray. Since the interspace distance between atomic planes (D) is on the order of the x-ray (10^{-10} m), two incident x-rays parallel to each other will be reflected by the atoms of the crystal lattice and they will interfere constructively when they travel the total distance that differs by an integer number multiple of their wavelength, that is when the two waves are fully in-phase.
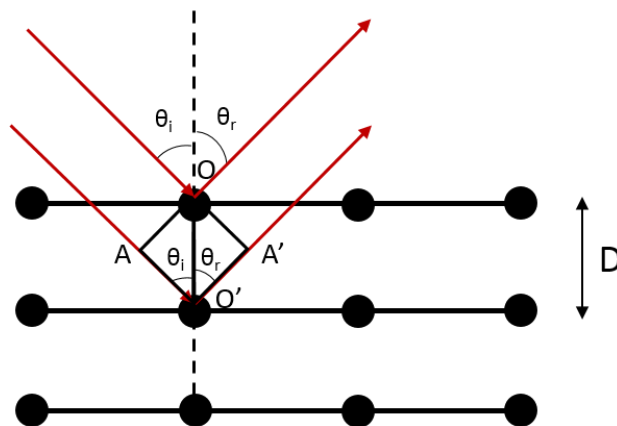
Figure 2.5. Scheme of the diffraction process of two incident beams in a one-dimensional crystal.

In figure 2.5, two parallel and in-phase X-rays (red arrows) hit a crystal lattice forming an incident angle, θ_i, and then they are reflected out of the surface at an angle $\theta_r = \theta_i$. The wave on the bottom travels a greater distance compared to the wave on top. The extra distance that it travels is equal to

$$AO' + O'A' = m\lambda, \qquad (2.19)$$

where λ is the wavelength of the X-ray and m is a multiple of the wavelength λ ($m = 1$ for first-order diffraction, $m = 2$ for second-order diffraction and so forth). This means that there are constructive interferences between two beams when their optical path difference is equal to an integer number of wavelengths. Looking at the right triangles that the rays form with the normal line (dashed line), OAO' and OO'A', the hypotenuse of both triangles corresponds to the inter-planar distance D. Consequently, for the triangle OAO'

$$\cos\theta_i = \frac{AO'}{D},$$
$$\qquad (2.20)$$
$$AO' = D\cos\theta_i,$$

and for the triangle OO'A

$$\cos\theta_r = \frac{O'A'}{D},$$
$$\qquad (2.21)$$
$$O'A' = D\cos\theta_r.$$

Remembering that $\theta_r = \theta_i$, Bragg's law is then obtained by rewriting equation 2.19 by substituting AO' and O'A' with the solution of the equations 2.20 and 2.21

$$D\cos\theta_i + D\cos\theta_r = m\lambda, \qquad (2.22)$$

$$2D\cos\theta_i = m\lambda. \qquad (2.23)$$

Bragg's law is used to calculate the distance between atoms (D) based on the wavelength of X-ray (λ) and the angle of incidence of the X-ray (θ_i). This equation is valid for λ < D and if the incident light undergoes specular reflection. Since PhCs possess a periodicity similar or smaller than the wavelength of the incident light (λ ~ D), the refractive indices of the media should be considered and Snell's law has to be applied.
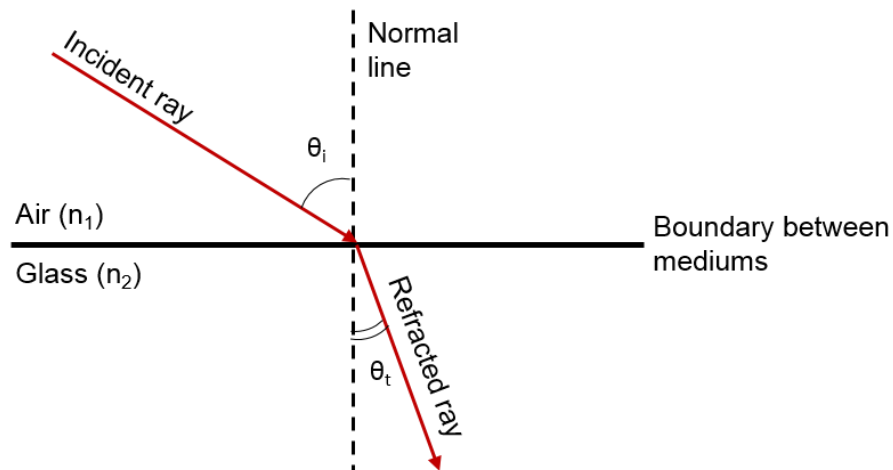
Figure 2.6. Schematic representation of ray diffraction.

When light passes from one transparent medium to a different transparent medium, light refraction occurs. This phenomenon is a result of the fact that light travels with different speeds in different media. Figure 2.6 shows a schematic representation of wave refraction when an incidence ray travel from air to glass. The ray enters a medium (glass) in which the speed of light is lower compared to the light speed on air, then the ray bends towards the normal line. This means that the angle of the incidence light (θ_i) is bigger than the angle of refraction (θ_t).

Snell's Law gives a relationship between the angle of incidence, the angle of refraction and the index refraction of both media (n_1 and n_2):

$$n_1 \sin \theta_i = n_2 \sin \theta_t. \qquad (2.24)$$

If $n_1 < n_2$ then $\theta_i > \theta_t$, and if $n_1 > n_2$ then $\theta_i < \theta_t$.

For structure made by i non-interacting materials as PhCs, n_2 can be approximated by an effective refractive index n_{eff} calculated as the weighted average of refractive indices with weights given by the volume fraction of the different components (e.g. air and polystyrene for a PhC made of polymer spheres and air) [14]. Therefore, if $n_1 = n_{air} = 1$ (air), the Snell's Law can be written as

$$n_{air}\sin\theta_i = n_{eff}\sin\theta_t. \qquad (2.25)$$

By taking into account this refraction occurring when light crosses the interface from air to the photonic crystal, the correct optical path can be calculated from figure 2.7. i.e., considering that AO' = O'A' and BO = OB' (figure 2.7-a), the optical path can be written as

$$2\left(n_{eff}AO' - n_{air}BO\right) = m\lambda. \qquad (2.26)$$
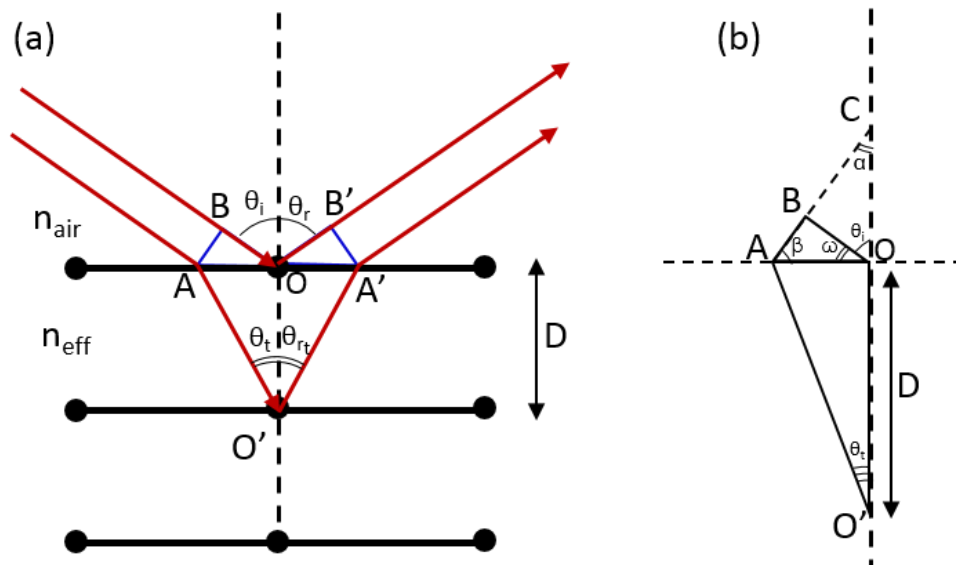
Figure 2.7. Scheme of the diffraction model of one-dimensional photonic crystal (a), and geometric representation of the ray diffraction (b).

Figure 2.7-b shows a zoom of the triangles, AOB and AOO' (figure 2.7-a), that the light forms with the normal line (dashed line) and the crystal planes. The geometrical representation of the incident and refracted rays allows one to express AO' and BO as a function of $\sin\theta_i$ and $\sin\theta_t$, respectively. From the triangles AOC,

AOB and BOC (figure 2.7-b), we can easily assume that $\alpha + \beta = 90°$ and $\alpha + \theta_i = 90°$, so that $\beta = \theta_i$. Moreover, trigonometric relationships suggest that

$$\cos\theta_t = \sqrt{1 - sin^2\theta_t} = \frac{OO'}{AO'} = \frac{D}{AO''},$$ (2.27)

$$\sin\theta_i = \frac{BO}{AO'},$$ (2.28)

$$\sin\theta_t = \frac{AO}{AO'}.$$ (2.29)

Therefore,

$$AO' = \frac{D}{\cos\theta_t} = \frac{D}{\sqrt{1 - sin^2\theta_t}},$$ (2.30)

$$BO = AO \, \sin\theta_i = (AO' \sin\theta_t) \sin\theta_i.$$ (2.31)

From equation 2.25, Snell's law, and considering that $n_{air} = 1$

$$\sin\theta_t = \frac{\sin\theta_i}{n_{eff}}.$$ (2.32)

Then we can combine Snell's law with Bragg's law by rewriting equations 2.30 and 2.31 with the help of 2.32. AO' and BO can be expressed in terms of $\sin\theta_i$ and n_{eff} as follows:

$$AO' = \frac{D}{\sqrt{1 - sin^2\theta_t}} = \frac{D}{\sqrt{1 - \frac{sin^2\theta_i}{n_{eff}^2}}} = \frac{D}{\sqrt{\frac{n_{eff}^2 - sin^2\theta_i}{n_{eff}^2}}}$$

$$= \frac{D}{\frac{\sqrt{n_{eff}^2 - sin^2\theta_i}}{n_{eff}}} == \frac{Dn_{eff}}{\sqrt{n_{eff}^2 - sin^2\theta_i}},$$ (2.33)

$$BO = (AO' \sin \theta_t) \sin \theta_i = \frac{Dn_{eff}}{\sqrt{n_{eff}^2 - sin^2\theta_i}} \frac{sin^2\theta_i}{n_{eff}} = \frac{Dsin^2\theta_i}{\sqrt{n_{eff}^2 - sin^2\theta_i}}.$$

<div style="text-align:right">(2.34)</div>

Bragg-Snell law is then obtained by rewriting equation 2.26 with the help of the expression for AO' and BO given in 2.33 and 2.34:

$$m\lambda = 2(n_{eff}AO' - n_{air}BO) = 2\left(\frac{Dn_{eff}^2}{\sqrt{n_{eff}^2 - sin^2\theta_i}} - \frac{Dsin^2\theta_i}{\sqrt{n_{eff}^2 - sin^2\theta_i}}\right) =$$

<div style="text-align:right">(2.35)</div>

$$= 2D\left(\frac{n_{eff}^2 - Dsin^2\theta_i}{\sqrt{n_{eff}^2 - sin^2\theta_i}}\right) = 2D\sqrt{n_{eff}^2 - sin^2\theta_i}.$$

Bragg-Snell law allows one to estimate the spectral position of the photonic band gap (λ) depending on the angle of the incident light (θ_i), the interplanar spacing between the media (D), the refractive indices and volume fraction of the media (n_{eff}).

Chapter 3. Luminescent conjugated-polymers

Organic semiconductors are a class of organic materials which includes conjugated small molecules and conjugated polymers characterised by interesting electrical and optical properties for photonic and optoelectronic applications, such as organic light-emitting diodes (OLEDs) [15-18], organic photovoltaic cells [18,19], organic field-effect transistors (OFETs) [20,21] and lasers. This chapter gives a brief overview of the electronic and optical properties of organic semiconductors, and in particular on conjugated polymer. Furthermore, the structure and the main photophysical properties of poly(4-4'-diphenylene diphenylvinylene), or briefly PDPV, are also presented.

3.1 **Introduction to organic semiconductors**

Compared with inorganic materials, carbon-based materials offer a variety of advantages in terms of synthesis and processability. By tailoring certain structural parameters (e.g. side chain length, interlocked architectures, degree of polarization, etc.), as well as substituent groups, it is in fact possible to finely tune the chemical structure of conjugated macromolecules in order to obtain desirable physical and optical properties of the semiconductor [22]. Furthermore, since conjugated small molecules and polymers can be designed so as to be soluble in either water or organic solvents, solution-processing techniques (i.e. drop-casting, spin-casting, layer-by-layer deposition, roll-to-roll processing, etc.) can be used for a low-cost fabrication of large area devices on a variety of different substrates, including flexible ones. Consequently, the goals of organic-based devices is not that of overcoming the inorganic technologies performance, but of cutting fabrication costs, and introducing

new mechanical properties for the final device as flexibility and mechanical resistance. For the discovery and development of conductive polymers the Nobel Prize in Chemistry 2000 was awarded jointly to Alan J. Heeger, Alan G. MacDiarmid and Hideki Shirakawa [23].

3.2 **Electronic properties**

Semiconducting polymers are sp^2-hybridised carbon-based chains characterised by the alternation of single (σ) and double (σ and π) bonds along the main chain (see for example the structure of polyacetylene in Fig. 3.1).
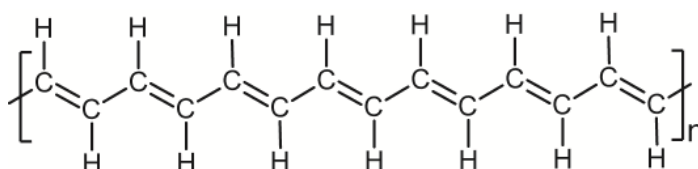
Figure 3.1. Chemical structure of trans-polyacetylene, the simplest conjugated polymer.

The molecular orbital structure resulting from the linear combination of the orbitals of the carbon atoms determines the electrical properties of organic semiconductors. By considering that the electronic configuration of the carbon atoms is $1s^2 \, 2s^2 \, 2p^2$, in the ground state, and by applying the hybridisation theory of atomic orbitals, we can better describe carbon bonds and understand their properties.

The hybridisation theory considers three different hybrid states, i.e. *sp^3*, *sp^2*, and *sp*, coming from the linear combination of *s* and *p* atomic orbitals. Figure 3.2 schematically explains all these possible configurations. In the *sp^3* hybridisation (see for example Figure 3.2-a) the *2s* orbital is mixed with three *2p* orbitals generating four new atomic orbitals having the same energy and pointing toward the vertices of a tetrahedron, with an angle of 109,5°. Each orbital has one electron and interacts with closed atoms by generating σ (bonding) and σ* (anti-bonding) orbitals. Since the promotion of an electron from the σ to the σ* orbital requires an energy E ~ 10 eV, the polymers obtained by *sp^3* interaction are considered insulators (i.e. polyethylene).

On the other hand, the mixing of the *2s* orbital with two *2p* orbitals, out of the three available, leads to the sp^2 hybridisation (see for example Figure 3.2-b). In this configuration, the new three sp^2-atomic orbitals are arranged in a trigonal planar geometry, with an angle of 120° between one another, and they are able to form strong, highly directional σ-bonds with neighbouring atoms. The third *2p* orbital does not take part in the hybridization and can interact with an adjacent carbon to form so-called π (bonding) or π* (anti-bonding) orbitals. The choice of the Greek letter is suggestive of the fact that these molecular orbitals derive only from *p* atomic orbitals, without the contribution from *s* orbitals, and the "*" is usually take to indicate the excited orbital of this type. Since the π-orbital is lower in energy that the π*-orbital, in a simple two-sp^2-carbon system (i.e. C_2H_4) at the ground state the two electrons coming from the p_z orbitals will occupy the bonding orbital leaving unoccupied the π* orbitals. The highest occupied molecular orbital is called HOMO, while the lowest unoccupied molecular orbital is called LUMO. The energy separation between HOMO and LUMO is a forbidden energy gap, *Eg*, which correspond to the bandgap of crystalline (extended) materials (see for example Figure 3.3-a). Finally, the *sp* hybridisation (see for example Figure 3.2-c) is originated by the combination of the *2s* orbital and one *2p* orbital, out of three *2p* orbital available, forming a total of two *sp* orbitals oriented at 180° from one other. This type of hybridisation allows formation of one σ-bond and two π-bonds. The delocalisation of π/π*-states in between neighbouring sp^2-carbon atoms allows electrons to move along the carbon backbone giving rise to electrical conductivity. The conjugation length, or in other words the extension of the π-electron delocalization, also affects the electrical and optical properties of conjugated polymers. As the number of π (π*) molecular orbitals increase, the π (π*) levels take the form of quasi-continuous bands and the HOMO/LUMO gap decrease, i.e. by varying from 6.7 eV for ethylene to 1.5 eV for stretch-oriented polyacetylene[24], as illustrated in figure 3.3-b.
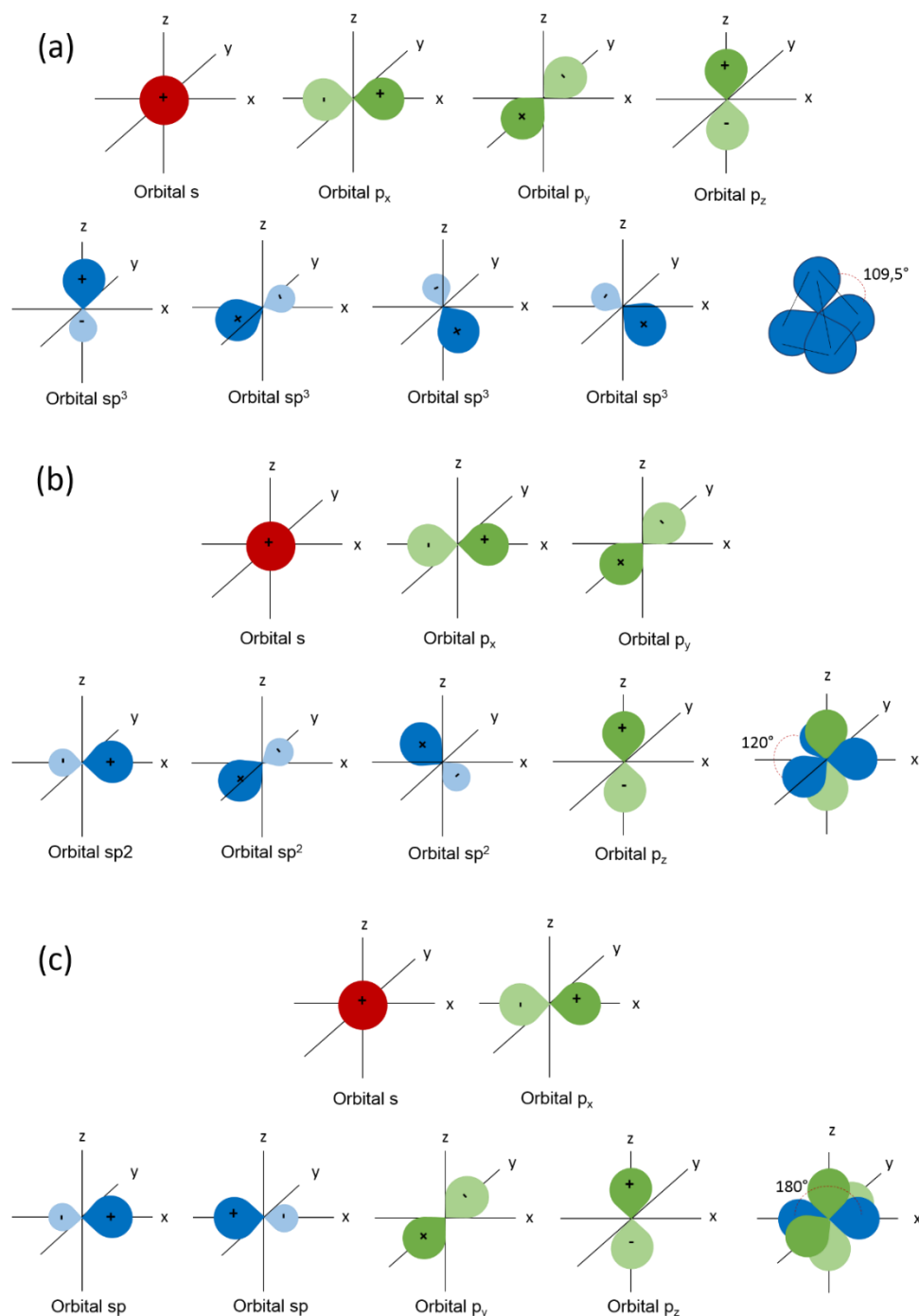
Figure 3.2. (a) In the *sp³* hybridisation, 4 atomic orbital are combined, one s (red) and three p (green), to give 4 hybridised molecular orbitals *sp³* (blue) which are arranged in a tetrahedral geometry. (b) In the *sp²* hybridisation, 3 atomic orbital are combined, one s (red) and two p (green), to give 3 hybridised molecular orbitals *sp²* (blue) arranged in a triangular planar geometry. The p_z orbital does not take part in the hybridisation and it stays perpendicular to the sp² plane. (c) In the *sp* hybridisation, 2 atomic orbital are combined, one s (red) and one p (green), to give 2 hybridised molecular orbitals *sp* (blue) arranged in a linear geometry. Both p_z and p_y orbitals do not take part in the hybridisation and they stay perpendicular to the *sp²* plane and to each other.
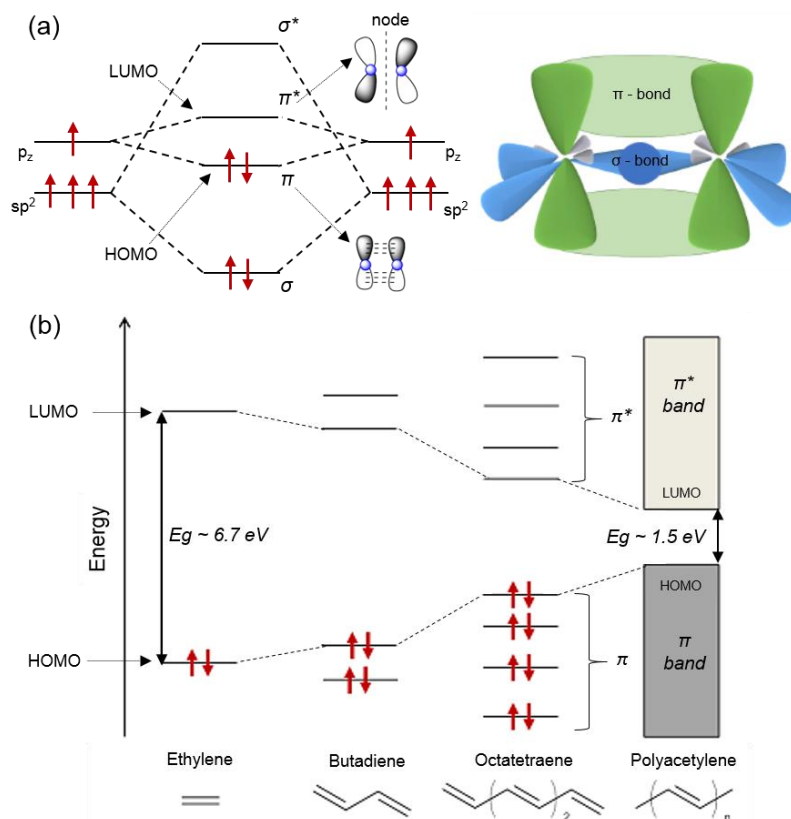
Figure 3.3. Schematic representation of energy levels and molecular orbitals of ethylene. The p_z orbitals of neighbouring carbons overlap to form new and extended orbitals with an energy splitting, namely π-bonds and π*-anti-bonds. (b) Increasing the conjugation length has the effect of broadening the ensemble of hybrid states into a quasi-continuous 'band' and narrowing the energy gap, Eg. Adapted from ref. [2].

3.2.1 Polarons

The presence of an extra charge resulting by either charge injection or a chemical reaction tend to polarises the surrounding atoms of a conjugated polymers. This polarization leads to structural relaxations of the molecule toward a new equilibrium causing the appearance of inter-band state between the π and π* bands (see for example figure 3.4). The extra charge together with the polarization effect form a quasi-particle state that is referred to as a "polaron". Polarons can be either negative or positive. "Bipolarons", instead, are formed when two polarons of the same sign interact via lattice deformation[25-27].

π* conduction band

positive
bipolaron

positive
polaron

exciton

negative
polaron

negative
bipolaron

π valence band
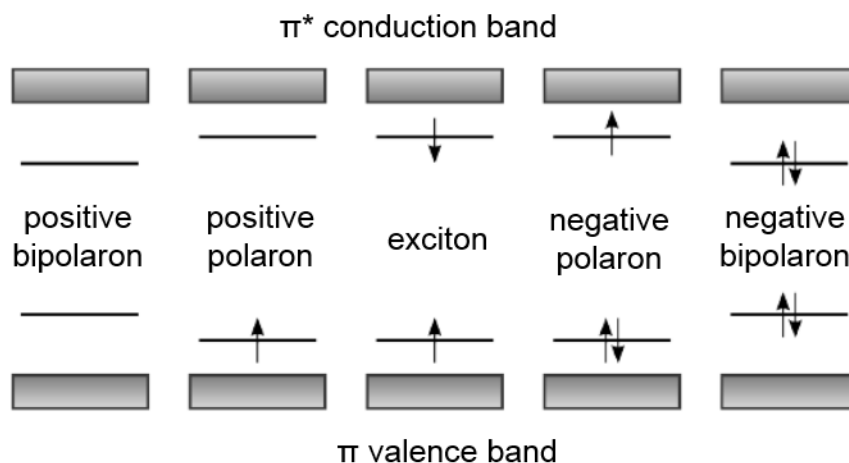
Figure 3.4. Schematic representation of inter-band states called polarons levels which are formed by the distortion of the structure of organic molecules after the molecular polarization due to a net charge (adapted from ref. 18).

In the solid state (relevant to optoelectronic applications) polymer chains are close to each other allowing the interaction between molecular orbitals of neighbouring molecules. Consequently, charge transport is not limited along the chain, but it can occurs also between adjacent molecules via hopping mechanism upon thermal activation or phonon-assisted tunnelling [24]. However, intermolecular interactions are typically much smaller than inorganic semiconductors. The distances between conjugated molecules negatively affect the intermolecular delocalization and consequently reduces the electrons tendency to be delocalized over the complete active layer. This clearly indicates that the optimisation of the film morphology becomes essential to obtain efficient charge transport [28-30].

3.2.2 Excitons and energy transfer

The formation of excited species resulting from photoexcitation also leads to structural modifications of the conjugated chain, and to polarization of the surrounding atoms. Considering that organic molecules have a relatively low dielectric constant (ε_r ~ 1.8 - 6) compared to inorganic compounds, the transition of an electron from the HOMO to the LUMO orbital generates "excitons". Excitons are bound hole-electron

pair, and can be classified in three different types depending on their binding energy, i.e. Wannier-Mott, Frenkel, and charge-transfer excitons.
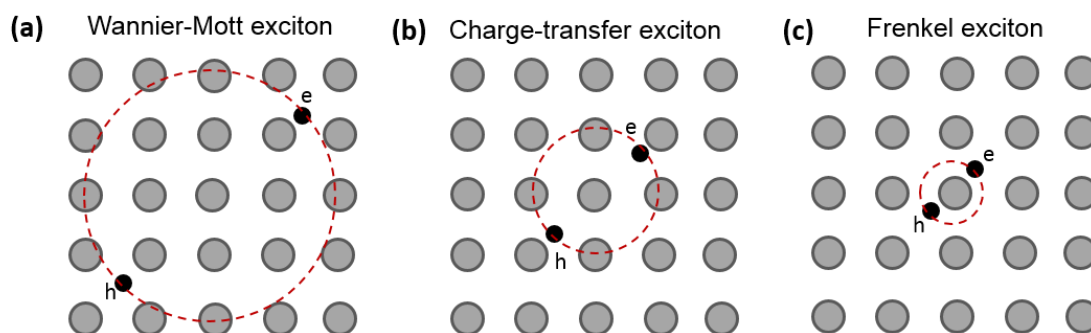
Figure 3.5. Schematic representation of a Wannier-Mott exciton (a), charge-transfer exciton (b) and Frenkel exciton (c).

The Wannier-Mott excitons or long-radius excitons are characterised by a radius (i.e. distance between electrons and holes) bigger than the lattice parameter and by a binding energy less than 0.1 eV. They are usually found in inorganic semiconductors where the dielectric constant is large (see for example figure 3.5-a). Frenkel excitons or small-radius excitons are characterised by a binding energy between 0.2 eV and 1 eV, i.e. their energy lies inside the energy gap. The spatial extension of the excitation is restricted to a single unit cell, and excitons are, to a large extent, localised at a specific atom or molecule. They are usually found in insulating materials or in organic semiconductors where the dielectric constant is small (see for example figure 3.5-c). Charge-transfer excitons represent an intermediate condition between the Wannier-Mott and the Frenkel excitons. They can be found in organic semiconductors as well (see for example figure 3.5-b).

Transfer of excited states between adjacent molecules occurs via energy transfer. The molecule which donates the exciton is called donor, D*, and it is in the electronic excited state, while the molecule which accepts the exciton is referred as an acceptor, A, and it is in its ground state. The energy transfer mechanism can be explained using two models which consider transport as a non-radiative process: Förster and Dexter. The general energy transfer process can be written as

$$D^* + A \rightarrow D + A^*$$
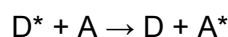
where * indicate the electronic excited state.
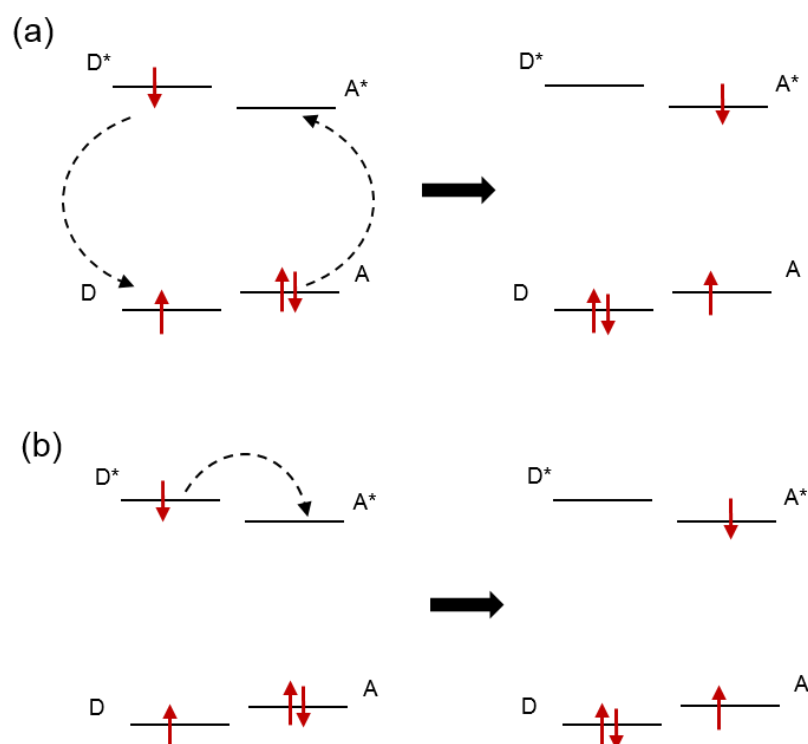
Figure 3.6. Schematic representation of the diffusion of an exited state between adjacent molecules via (a) Förster and (b) Dexter mechanism.

In the Förster model, known as Förster fluorescence resonance energy transfer (FRET), the energy transfer occurs as a consequence of a resonant dipole-dipole interaction between the dipole transition moments of the donor and the acceptor. From the figure 3.6-a is easy to understand that the relaxation process of the donor toward its ground state involves a release of energy that excites the acceptor via a non-radiative resonance energy transfer. The FRET efficiency increases together with the overlap of the emission spectra of the donor with the absorption spectra of the acceptor and it is inversely proportional to r^6, where r is the distance between D* and A. On the other hand, the Dexter mechanism is based on electron exchange interaction. In particular, the electron in the LUMO of the donor is transferred to the LUMO of the acceptor while an electron of the HOMO of the acceptor is transferred to the HOMO of the donor (see for example Figure 3.6-b). The efficiency of the Dexter process

increases together with the overlap between the wave functions of the involved orbitals, and decrease exponentially when the distance between D* and A increase.

3.3 **Optical properties**

As explained in the previous section, an exciton is a bound hole-electron pair generated also from photo-stimulation of polymers. Consequently, it is defined as an unstable state that can decay to the ground state releasing energy. In particular, the exciton can relax either via radiative, i.e. a photon is emitted, or non-radiative transition.

To better understand all the possible transition in a molecule, the Jablonski diagram is used. The latter describes the different energy levels of a molecule (i.e. electronic, vibrational, rotational and translational levels), the optical transitions between them, and consequently the optical properties of organic semiconductors. In the Jablonski diagram of figure 3.7 the molecular electronic states are presented as a set of lines grouped depending on their multiplicity. The singlet and triplet states are named S_1 and T_1, respectively, while the ground state is named S_0. Each electronic levels are associated with vibrational levels (thin lines labelled by 0, 1, 2, 3) having a smaller spacing in energy (~0.1-0.2 eV) than electronics levels. The vibrational ground states of each electronic state are marked with thicker lines. Usually, the radiative process (i.e. light absorption, fluorescence, and phosphorescence) are indicated with solid lines, whereas non-radiative (i.e. vibronic relaxation, internal conversion, and inter-system crossing) processes with dashed lines.
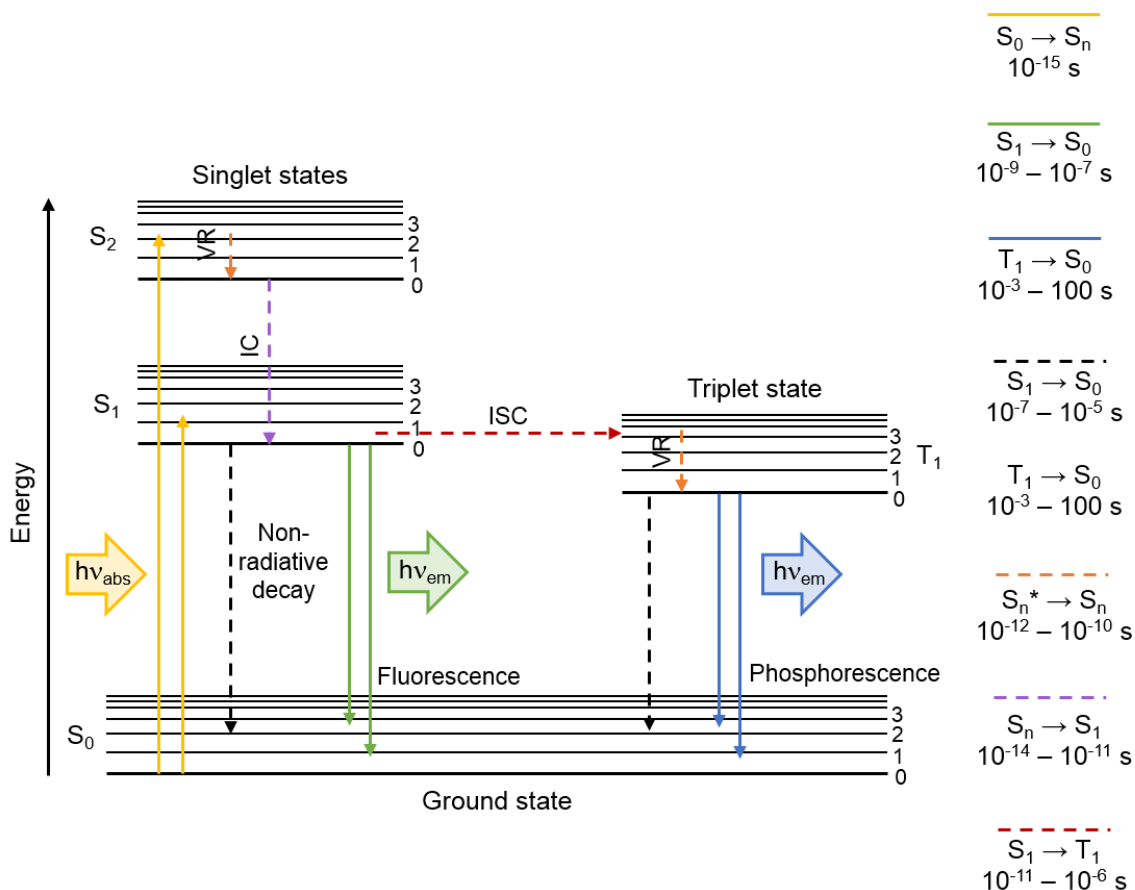
Figure 3.7. Jablonski diagram. Schematic representation of the molecular energy levels and of the possible transitions between them. On the right, the speed of the radiative e non-radiative relaxation process is illustrated.

At room temperature the thermal energy is ~ 26 meV and only the fundamental vibrational state is populated. The process that generates the exciton is the vertical absorption of a photon from the ground state S_0 to an excited state S_1 or S_2 ($h\nu_{abs}$ in Fig. 3.7). These excited state tends to release the energy in excess by a radiative or non-radiative mechanism. The non-radiative mechanism does not involve photons emission, but the energy is released as thermal energy. In the vibronic relaxation (VR) process, an excited state relaxes to its vibrational ground state by realising thermal energy to the environment. Other types of non-radiative decay can involve electronic states having the same spin multiplicity, this is the case of internal conversion, IC, or with different spin multiplicity as the intersystem crossing, ISC. On the other hand, the

radiative relaxation involves the emission of photons from an excited state to the ground state. Depending on the spin multiplicity of the emission level, the radiative relaxation can be classified in fluorescence and phosphorescence emission. If the photons are emitted from an excited state having the same spin multiplicity that the ground state (i.e. $S_1 \rightarrow S_0$), the process is known as fluorescence. Fluorescence is a rapid radiative process, the photon is emitted in a range of time of $10^{-9} - 10^{-7}$ s. Phosphorescence, instead, release photons from T_1 excited state to the ground state S_0. Since the transition $T_1 \rightarrow S_0$ is spin-forbidden, the phosphorescent mechanism is very long, up to ms or even s.

According to the Born-Oppenheimer approximation, the optical transitions occur on a shorter time scale compared to molecular vibration. Consequently, the probability of a transition is proportional to the overlap between the vibrational wave functions of the initial and final states. Figure 3.8 illustrates the molecular potential energy curve as a function of the nuclear coordinates. Since in the Frank-Condon approximation, the nuclei are considered fixed during electronic transitions, the latter can be considered as vertical transitions, orange arrows for absorption and green arrows for emission. Since the equilibrium geometry of the molecule in the ground state is different from that on the excited state, the S_{00}-S_{10} transition is characterised by a small overlap between the initial and final wave function, while the transition with the higher probability is the S_{00}-S_{11} as shown from the solid orange arrow. Similarly, the emission transition with a higher probability is the S_{10}-S_{01} as indicated by the vertical solid green arrow. The different transition probability between absorption and fluorescence explains why the absorption and emission peaks do not spectrally overlap (Stokes' shift).
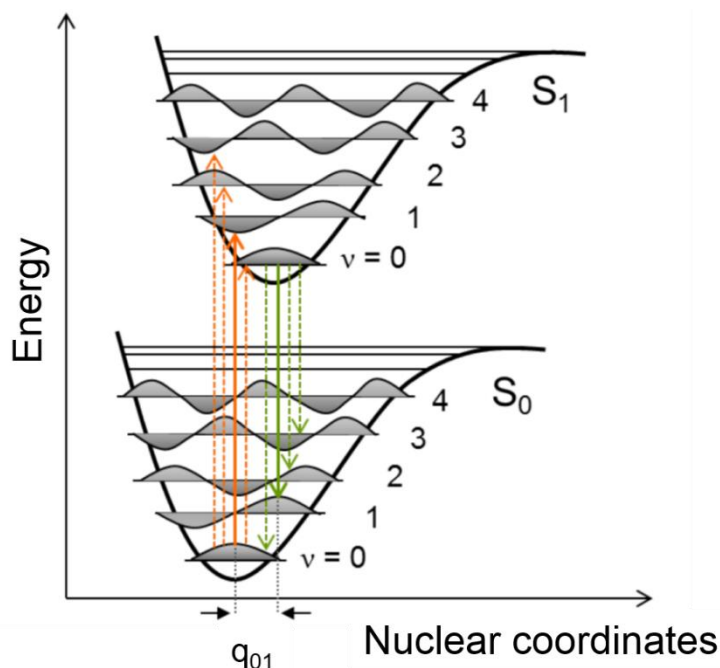
Figure 3.8. The diagram shows the Franck-Condon principle. The absorption transitions are represented by vertical orange arrows from the ground state, S_0, to the exited state, S_1, potential energy curve, while the emission transition by vertical green arrows from the S_1 to the S_0 energy level. The vibrational wave functions for each state are depicted in grey. Adapted from ref. [2].

The ratio between the number of photons emitted relative to the number of photons absorbed represent one of the most important parameters used to determine the photophysics of a fluorophore, and it is defined as "photoluminescence quantum efficiency", ϕ_{PL}

$$\phi_{PL} = \frac{k_r}{k_r + k_{nr}} \qquad (3.1)$$

where k_r is the radiative rate for the decay to S_0, and k_{nr} is the non-radiative decay rate. Furthermore, to investigate the dynamics of the exited state, another parameter needs to be considered, i.e. the "photoluminescent lifetime", τ, which gives information about the average time a molecule stays in the exited state before decaying to the ground state.

$$\tau = \frac{1}{k_r + k_{nr}} \qquad (3.2)$$

The photoluminescent lifetime is very sensitive to the environment surrounding and it can be used to evaluate the mechanism and the efficiency of the fluorescence quenching.

3.3.1 Photoluminescence quenching

The photoluminescence quenching is the reduction of the photoluminescence (PL) intensity due to alternative paths of decay. The fluorescence intensity can be reduced by two types of quenching mechanisms, static and collisional (or dynamic) quenching. Both of them require that the fluorophore come into contact with a quencher [31].

In the static quenching the drop in fluorescence results from the formation of a non-radiative complex between the fluorophore in its ground state and a quencher. The type of process is defined static since it does not depend on the molecular diffusion or on the exited state life time of the fluorophore. Furthermore, the static quenching can be easily detected from the absorption spectrum of the fluorophore-quencher complex, which presents a shift with respect to the fluorophore absorption curve. On the other hand, collisional quenching take place when the fluorophore in its excited state comes into contact with a quencher. Consequently, the decrease of the fluorescence intensity depends on the molecule diffusion and on the fluorophore lifetime. Additionally, the dynamic quenching mechanism varies with the nature of the quencher [32].

A form of static quenching is the quenching by aggregation. Indeed, depending on the chain structure of the polymers, they can interact with each other by intermolecular Van Der Waals-like forces and generate H- or J-aggregates, which exhibit discrepancies in the absorption and emission spectra with respect to the

isolated polymer [33]. J-aggregates come from the head-to-tail arrangement of the polymer chains. They are characterised by a red-shift of the absorption curve and by high PL quantum yield. On the contrary, H-aggregates consist of co-facial aggregation of the conjugated polymer chain typically observed on polymer thin-films. They present a blue-shift of the optical absorption and low or absent photoluminescence.

A possible way to avoid the formation of aggregates and consequently the decrease of the PL quantum yield is the control of the intermolecular interactions like in supramolecular structures. The general characteristics of supramolecular materials, and a discussion on a particular classes of supramolecular structure, i.e. polyrotaxane, it will be presented in the next chapter.

3.4   **Poly(4,4'-diphenylene diphenylvinylene)**

Poly(4-4'-diphenylene diphenylvinylene), or briefly PDPV, is a conjugated polymer which has been studied as active materials for organic optoelectronics due to the promising optical and electrical properties. It has been demonstrated that the interesting radiative properties of PDPV, such as photostability and high photoluminescent efficiency, derive from its own chemical structure. Indeed, PDPV consist of a poly(para-biphenylene vinylene) chain where the hydrogen atoms on the vinylene singularity are substituted with phenyl rings (see for example Figure 3.9) [34].
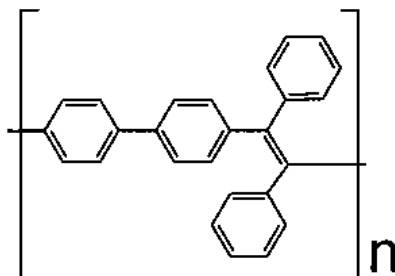
Figure 3.9. Chemical structure of PDPV, poly(4-4'-diphenylene diphenylvinylene).

The replacement of the vinylene hydrogens by phenyls leads to reduced photo-oxidative degradation and consequently promotes the photostability of the material.

The good solubility of the PDPV in common organic solvent (i.e. chloroform or toluene), and the high PL quantum efficiency are other interesting properties resulting from this chemical modification along with the disorder induced by cis/trans isomerism and the reduced π-π aggregation in solid-state. In support of this Winroth *et al.* have demonstrated the stability of the optical and electroluminescence properties over a period of time of at least one decade [35,36]. Furthermore, the conformational relaxation in the excited state of the rings, lead to a large Stokes' shift between absorption and emission spectra which can be exploit for the production of white-emitting LEDs [37].

Chapter 4. Supramolecular structures

This chapter gives a brief introduction on supramolecular systems, on their structure, and properties. Furthermore, the structure of polyrotaxane and in particular the main photophysical properties of the polyrotaxane named PDV.Li ⊂ β − CD (Poly(4,4'-diphenylene vinylene) threaded through β-cyclodextrins) are discussed.

4.1 **Introduction to supramolecular systems**

Supramolecular systems are defined as large molecules in which smaller molecules interact by noncovalent interactions, in some cases even leading to molecular recognition by so-called lock and key model (see for example Figure 4.1). In particular, the building blocks of such supramolecular system can be linked by hydrogen bonding, metal coordination, hydrophobic forces, van der Waals forces, π-π interactions and electrostatic effects [38]. Those types of weak bonds generates new entities possessing unique properties, different from the starting molecules [39,40].
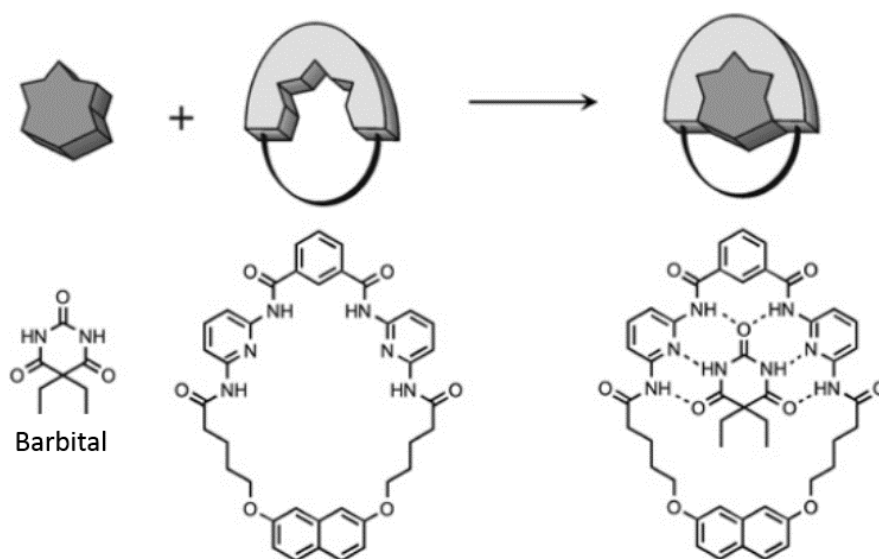
Figure 4.1. Schematic representation of molecular recognition due to hydrogen bonding N-H⋯O and N-H⋯N [30].

The design of highly interactive molecules, and the possibility to control the intermolecular interactions lead to a novel organic engineered materials suitable for optoelectronics and photonics, such as light-emitting diodes [41,42], and optically pumped lasers[43], but also for nanomachines able to reproduce a wide range of movements distinctive of natural machines, i.e. linear, rotating, and tweezer like movements (see for example Fig. 4.2).

Figure 4.2. Representation of two supramolecular systems: (a) a molecular tweezer made of two rings (i.e. crown ether) connected by a central unit -N=N-. If irradiated by light, the molecule changes structure, passing from trans to cis. This allows the two rings to get closer and therefore act as a trap for potassium ion; (b) a catenane made of two interlocked macrocycles, A and B having two sites of bonding for the cupper ion Cu^+, A1 and B1. If the Cu^+ is electrochemical oxidised, the ring A will rotate by 180° so that the Cu^{++} will interact with A2 and B1. The reduction of the Cu^{++} into Cu^+ leads to the initial structure of the catenane. [30].

4.2 **Polyrotaxanes**

In contrast to the common supramolecular bonds, rotaxanes are characterised by components linked by stronger but still non-covalent interactions. This means that rotaxane components cannot dissociate despite their high degree of mobility and freedom.

As showed in figure 4.3-a, rotaxanes consist of a linear moiety mechanically strung into molecular rings (i.e. cyclodextrin macrocycles). If the ring can be easily disassociated from the linear molecule by external forces, then the structure is called "pseudorotaxane". On the other hand, it is defined "true rotaxane" a supramolecular system in which two stoppers (represented by two balls) are connected to the terminal sides of the linear moiety to prevent unthreading. Figure 4.3-a also shows the first and the highest level of rotaxane structure, [2] and [5]Rotaxane, respectively [44].
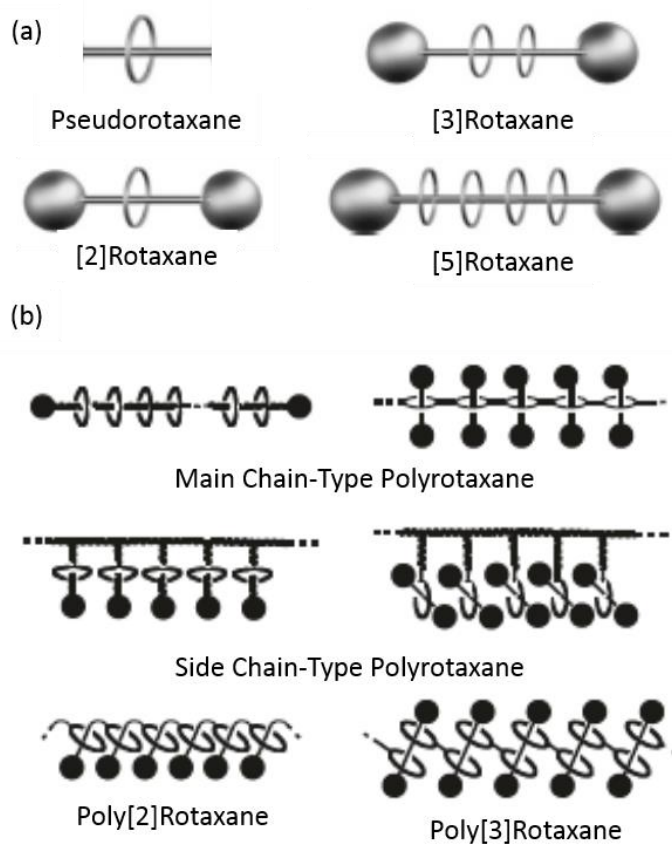
Figure 4.3. Schematic representation of rotaxane (a) and polyrotaxane (b) structures [34, 35].

60

The polymeric analogue of the low molar-mass rotaxane is the "polyrotaxane", which is characterised by a polymeric linear moiety. Depending on how the ring and the polymer chain are connected, polyrotaxanes can be grouped into different categories, (see for example Figure 4.3-b). In addition to the type of structure and chemical composition, the properties of polyrotaxanes are determined by the size of the macrocycle, the freedom of the components and by the "threading ratio" (TR) which is defined as the average number of rings per repeated unit. Additionally, such systems, can reproduce linear or rotating movements if carefully designed and adequately stimulated (see for example Figure 4.4) [45].
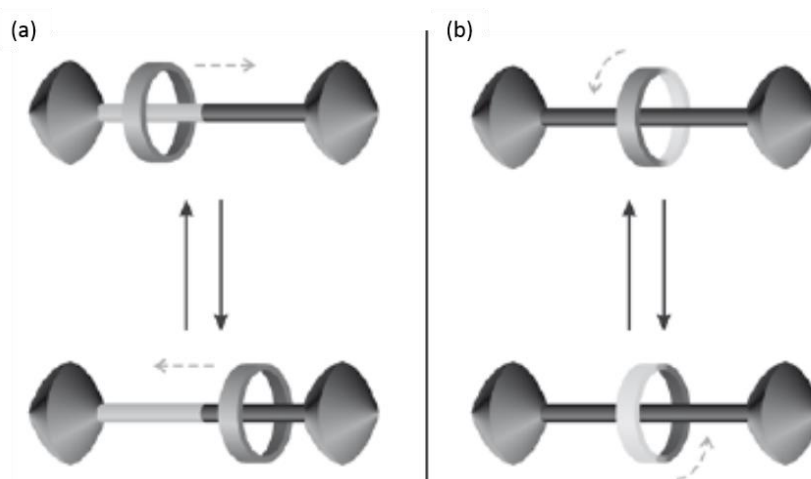
Figure 4.4. Schematic representation of linear (a) and rotating (b) movement of polyrotaxane [30].

4.3 **Poly(4,4'-diphenylene vinylene) $\subset$ β - CD)**

Polyrotaxanes have a chemical structure suitable for studying fundamental physical properties of conjugated semiconductors. Indeed, the macrocycle units can act as no-conjugated "spacer" between the conjugated chains consequently suppressing the intermolecular interaction. Therefore, they prevent intermolecular

quenching of the spontaneous emission and, by increasing the threading ratio, they do not suppress the charge transport in solid films [46].
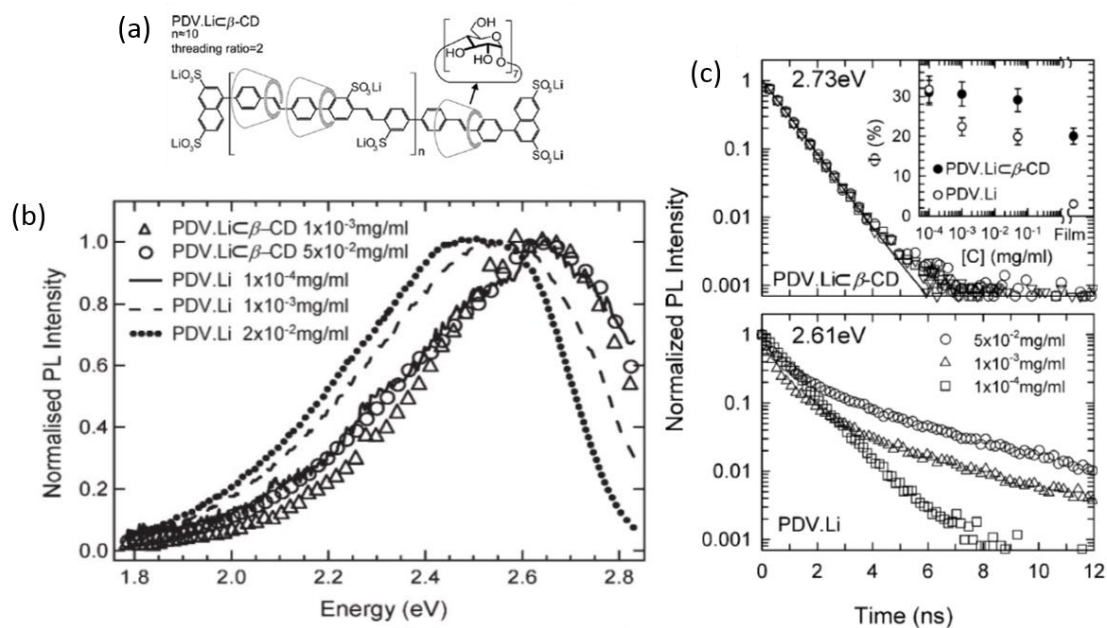
Figure 4.5. chemical structure of the PDV.Li ⊂ β – CD (a); Time-integrated emission spectra of PDV.Li solution at 5×10^{-2} mgml^{-1} (open circle) 1×10^{-4} mgml^{-1} (open triangles) and of all the solutions of the unthreaded polymer (b); time-dependent decays of solutions of PDV.Li ⊂ β – CD (top panel), and of unthreaded polymers (bottom panel). Insert: evolution of the photoluminescence quantum efficiency ϕ (%) as a function of concentration [47].

Poly(4,4'-diphenylene vinylene) threated through β-cyclodextrins, or briefly PDV.Li ⊂ β – CD (see Figure 4.5-a for the chemical structure), faithfully represents the polyrotaxane characteristics. M. Petrozza *et al.* have compared the optical properties of unthreaded and threated poly(4,4' – diphenylene vinylene), PDV.Li, in solution. Figure 4.5-b-c shows that the unthreaded PDV.Li is characterized by a long-lived non exponential decay strongly dependent on concentration and by a red-shifted emission typical of interchain species. On the contrary, the emission spectra of threaded PDV.Li ⊂ β – CD (TR = 2) is independent of the solution concentration. That means, the cyclodextrin rings controls the formation of interchain radiative states in solution [47].
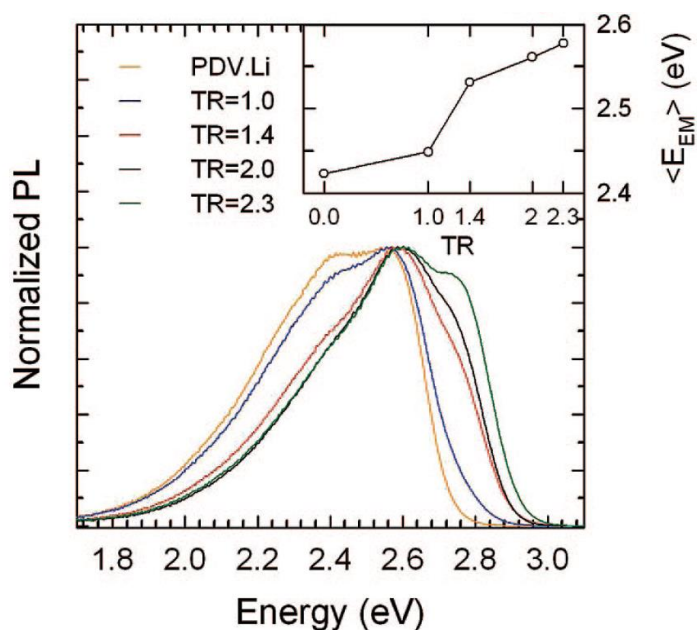
Figure 4.6. Time-integrated emission spectra of PDV.Li solution (5×10^{-2} mgml^{-1}) depending on TR. Insert: average emission energy extracted from the spectra [48].

S. Brovelli *et al.* have demonstrated that the control of the threading degree of polyrotaxanes influences the formation of interchain aggregates and consequently the related physical properties. Figure 4.6 shows the time-integrated photoluminescence of PDV.Li solutions depending on the TR. By increasing TR from 0 to 2.3 the red tail of the emission curve, which is characteristic of intrachain aggregates, is reduced; in the meantime, the blue region of the spectra, resulting from the intrachain exciton, becomes predominant. In support of those results, the time-resolved PL measurements show that the long-lived component, which is dominant for the unthreaded polymer, drops by increasing the TR [48].

Additionally, the results showed by F. Cacialli *et al*. (see ref. 49), highlight the polyrotaxane ability to reduce intermolecular interactions and photoluminescence quenching, while still allowing charge-transport, in the solid state. According to such previous works, the photoluminescence spectra of thin solid film of PDV.Li ⊂ β – CD blue-shifted with respect to those of the analogous non-rotaxinated PDV.Li (see for example Figure 4.7), and the value of the photoluminescence efficiency increasing for the rotaxinated polymer [49]. To verify the presence of charge transport in this class of supramolecular materials, Cacialli *et al*. have fabricated standard polymer LEDs also using PDV.Li ⊂ α – CD. The results obtained by testing the devices show that the LED functions are achieved [49].
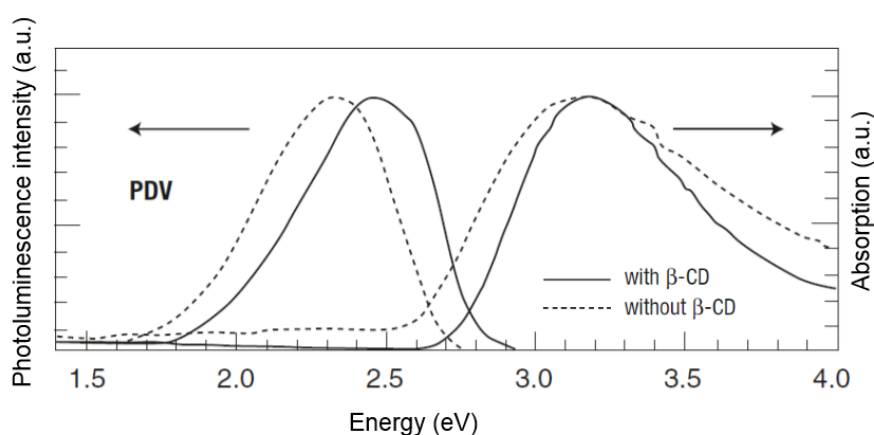
Figure 4.7. Absorption and photoluminescence spectra of thin film of the polyrotaxane (solid lines) and of the non-threaded chain (dashed lines), spun-coated on spectrosil substrate. Adapted from ref. 49

Last but not least, the presence of sulfonated sidegroups ($-SO_3^{3-}$) balanced by Li^+ ions in the PDV.Li ⊂ β – CD, allows the polyrotaxane to be solubilised in polar solvents, such as H_2O. Since in this work I use water-based colloidal solution, the rotaxane solubility in water is essential for the success of my experiments.

Chapter 5. Manipulation of polyrotaxane emission by opal high-energy bands

Opals are close-packed arrays of spherical particles capable to control the spontaneous emission of chromophores embedded between the spheres. This chapter gives an overview of the photonic effect of direct opals on the emission of a supramolecular conjugated polymer, i.e. $PDV_{10}Li \subset \beta - CD$. Firstly, the fabrication method for preparing bare and luminescent opals is explained. Secondly, the tuning of their photonic bands obtained in experiments of normal reflection, angle-dependent transmission and photoluminescence, is discussed across an enlarged energy range. The last section of this chapter focuses on the optical influence of the high-energy bands of the direct opals on the luminescence of $PDV_{10}Li \subset \beta - CD$.

5.1 **Introduction to opals**

Opals are probably the most popular 3D photonic crystals. This is mainly due to the effectiveness of the vertical deposition method, based on the natural tendency of the dielectric microsphere to self-assemble into face-centred-cubic arrays [6,7,50,51]. Besides, opals also represent a versatile system for the investigation of the photonic effects, an example being the fine-tuning of optical properties [52] including the modification of the emission spectra [53] and radiative rates [54]. In addition, the study of the photonic effect on the photoluminescence is simplified by the easy incorporation of active materials such as metal nanoparticles [55], semiconductor nanocrystals [56] or conjugated polymers [57] by infiltration, co-growth or evaporation.

All synthetic opals were prepared by using polystyrene microparticles, PS –

NPs, (ε = 2.4-2.7) [57], which constitute the filled volume fraction in the fcc structure,

whereas air (ε = 1) is the component of the fcc voids. More precisely, opals are

characterized by a rotated fcc lattice where the exposed direction is the (111), i.e. the

ΓL direction in the corresponding Brillion zone. Thus, the ΓL direction is the direction

usually investigated in reflection and transmission experiments, as discussed in figure

5.1.
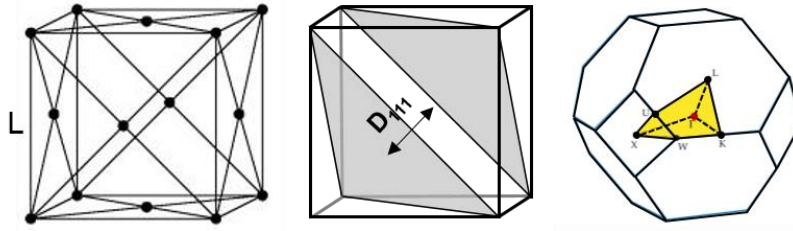
Figure 5.1. Schematic representation of an fcc lattice (left), the two planes (111) within the fcc cell (centre), and the Brillion zone (right) associated to the fcc structure.

Considering that the distance between the (111) plane reads

$$D_{111} = \frac{L}{\sqrt{3}} = d\sqrt{\frac{2}{3}}, \qquad (5.1)$$

where d is the sphere diameter used to prepare opals, we can express the Bragg-Snell

law (see equation 2.35, page 42) as a function of the sphere diameters:

$$m\lambda = 2d\sqrt{\frac{2}{3}}\sqrt{n_{eff}^2 - sin^2\theta}. \qquad (5.2)$$

We conclude that the PSB position depends on both the incidence angle and d. Due

to the small difference between ε of the two photonic components, i.e. polystyrene and

air, the polystyrene direct opals are classified as low-dielectric contrast media. They

cannot display a complete-photonic band gap and rather feature only a pseudo-

photonic stop band along the crystallographic direction (111).

5.1.1 High-energy bands

Although synthetic opals have been extensively investigated, the majority of experimental studies concerns the behaviour of the main PSB resulting from the Bragg diffraction by the (111) planes. Consequently, the investigated energy region is between $a/\lambda \sim 0.4$ and $a/\lambda \sim 0.8$ [53,57-59] (see for example the graph at the bottom of Figure 5.2). However, the optical situation at higher energy ($a/\lambda > 1$) could be of considerable interest. Besides the expected second and third order Bragg diffraction associated with the (111) planes, opals present additional bands with small splitting, which result from light diffraction by planes different from the (111), and which are associated to so-called Van Hove singularities [60-63]. In three dimensions, Van Hove singularities correspond to a divergence of the slope of the density of states in correspondence to a critical point of the Brillouin zone. The appearance of those bands at high frequencies does not allow a straightforward understanding of the photonic band structure, and the Bragg-Snell law is no longer sufficient to describe the optical properties of opals [64].

Figure 5.2 shows the experimental reflection and transmission spectra (bottom and middle graph, respectively) at normal incidence for a polystyrene-based opal, and its band structures (top graph) calculated by C. López and co-workers [62]. The solid bold curves of the top graph correspond to the ΓL bands arising from the dispersion of the wave-vectors (**k**) parallel to the ΓL direction, whereas the thin lines represent the bands due to diffractions coming from planes different from the (111). In the energy range where the band structure displays a linear trend with a constant slope (see the top graph at $a/\lambda < 1$) the opals result transparent in both transmission and reflection spectra, while in correspondence to the stop band ($a/\lambda \sim 0.6$) the reflection spectrum shows a peak accompanied by a dip in transmission. On the other hand, in the high-energy region ($a/\lambda > 1$) the number of energy bands increases and the complexity of the latter reflects the features in the transmission and reflectance spectra.

Furthermore, as D. Comoretto and co-workers explained [61], the PSB and the high energy bands display an opposite trend as a function of the incidence angle of light (θ). Indeed, by increasing θ, the PSB shifts to higher energies whereas the Van Hove singularities move to lower energies.
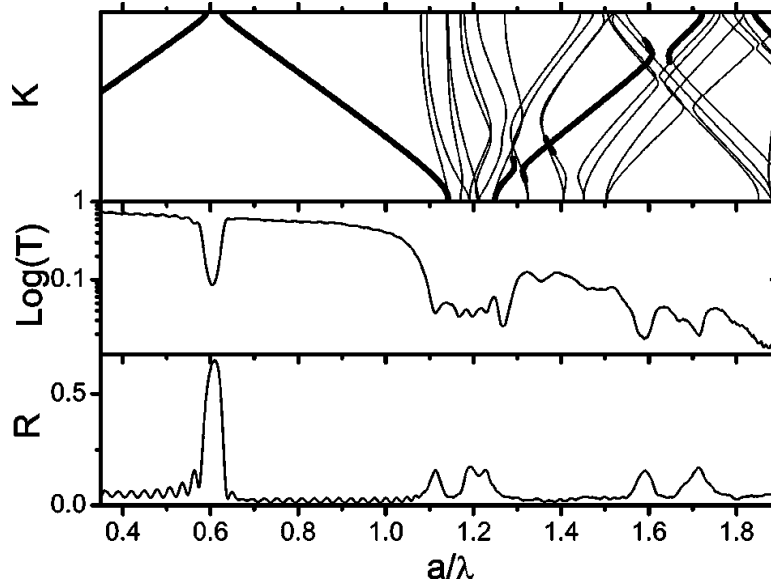
Figure 5.2. Band structure calculated along the ΓL direction in reciprocal space for an artificial opal consisting of polystyrene spheres (top). ΓL bands are highlighted with thick lines. Transmission (middle) and reflection (bottom) spectra at normal incidence for an artificial opal (ref. 62).

5.1.2   Density of states

The optical properties of atoms and molecules strongly depend on the density of states (DOS) [54,65], which is defined as the number of possible modes per unit frequency, ω, and it is expressed as [13]

$$D\left(\omega\right) = \frac{\omega^2 V}{\pi^2 c^3} \qquad\qquad 5.5$$

where V is the volume of the region considered when there is no material in it (e.g. an empty or "free space" cavity) and c is the vacuum speed of light. When the free-space is replaced by a uniform material, c is replaced by $v = {}^c/_n$, with n being the refractive

index of the medium. Femi's golden rule states that the transition probability (R) from an initial state *i* to a final state *f* depends on the density of the final state ρ.

$$R_{i \to f}(\omega) = \frac{2\pi}{\hbar} \, |\langle f|H'|i\rangle|^2 \rho(\omega) \qquad 5.6$$

The matrix element $\langle f|H'|i\rangle$ represents the perturbation between the final and the initial state.

Previous studies report that the spontaneous emission of a PhCs-embedded material is redistributed over the whole spectrum. More specifically, in correspondence of the PSB, depending on whether the DOS decreases or entirely vanishes the PL is partially or completely suppressed. In contrast, at the edge of the PSB, the DOS increases allowing an enhancement of the spontaneous emission[54].

As discussed in the previous section, opals show a variation of DOS also at high frequencies (1 < a/λ < 1.8). Therefore, a modification of the infiltrated opals emission is expected not only where the PSB appears, but even where the overlap between PL spectra and high-energy bands occurs. Consequently, photonic crystals can be used as a convenient tool to design and modify D(ω) and change the optical properties of luminescent materials.

Experiments have focused so far on studying the modification of emission intensity, directionality, and polarization which is induced by the existence of high-order photonic bands. These, however, concern mostly inverse opal structures where the higher dielectric contrast facilitates the observation of such effects. This thesis complements such studies by promoting direct opals at the forefront of research on light manipulation, and it sheds light on the relationship between the modification of the spontaneous emission and high-energy bands, as well as the diameter of the polystyrene microparticles.

5.2   Experimental methods

5.2.1   Bare opals preparation

Synthetic bare opals were prepared by using the vertical deposition technique [59]. The dielectric microparticles self-assemble in a stable and well-defined structure by exploiting the capillary action induced on the water surface. More in detail, a glass substrate was slowly extracted from an aqueous suspension of polystyrene monodispersed microspheres so that an fcc photonic array is gradually built at the interface between the water meniscus and the substrate (see for example figure 5.3-a).
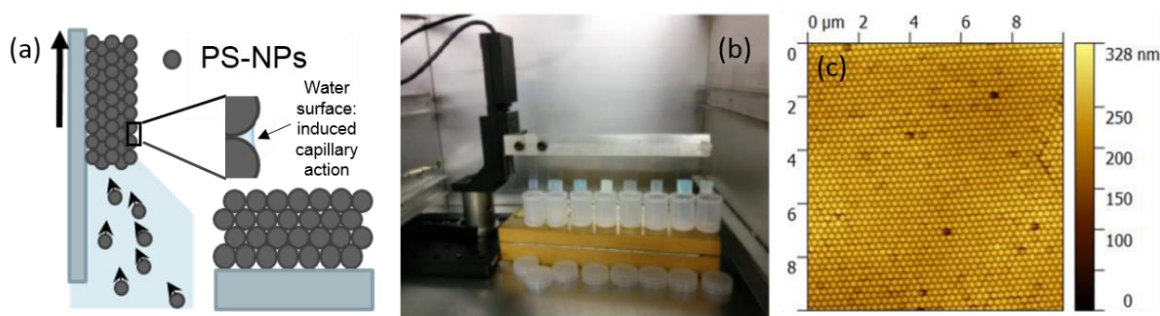
Figure 5.3. (a) Schematic representation of the vertical method. The PS-NPs self-assemble in a face-cantered-cubic array at the interface between the water meniscus and the glass substrate. (b) Experimental set-up for opal fabrication (photo by Dr. Valentina Robbiano). (c) AFM image of opals based on PS-NPs with a diameter of 260 nm.

In order to guarantee a high order degree of the photonic array and a good compromise between transmission and reflection measurements, an opal thickness between 3 μm and 4 μm is required. Hence, a commercial colloidal suspension (Duke Scientific polystyrene microparticles, 10% in volume having diameter of 220, 260, 300 and 340 nm, standard deviation 5%, refractive index 1.59) diluted to 0.2% in volume (100 μL of microparticles 10% in volume were added on 4900 μL of distilled water) was used.

The substrates adopted for growing opals are nothing more that commercial soda-lime glass microscope slides (original dimension 25x75x1 mm; final dimension obtained by cutting the slides using a diamante tip ~ 10x30x1 mm). Once cleaned in a bath of basic piranha (3:1:1 mixture of ammonia, water and hydrogen peroxide) [66], the slides were immersed perpendicularly into the colloidal suspension and were extracted at constant speed of 6.5 x 10^{-5} mm/s at 45°C ± 1°C by using a home-made dip coater with a motorized translation stage (by Thorlabs) (see for example figure 5.3-b). The obtained synthetic opals have an area of 1.5 x 1,0 cm. The opals growth took place into a BF53 Binder incubator located on an optical table to minimise vibrations deleterious for the opal periodicity.

5.2.2 Fluorescent opals preparation

The fabrication of the fluorescent opals consists in the co-growth of the polystyrene microparticles with the emitted material onto glass substrates, exploiting the advantages of the vertical method. More precisely, a glass substrate was slowly extracted (extraction speed of 6.5 x 10^{-5} mm/s at 45°C ± 1°C) from an aqueous suspension of polystyrene monodispersed microspheres (Duke Scientific 10% in volume diluted at 0.2% in volume; sphere diameters 200, 260, 300 and 340 nm, standard deviation 5%, refractive index 1.59), also containing 16 x 10^{-3} mg/ml of a water-soluble polyrotaxane as dye, i.e. poly(4,4'-diphenylene vinylene) threaded through cyclodextrin rings ($PDV_{10}Li$ β – CD). Figure 5.4 shows the chemical structure and the optical properties of a spin-coated film of $PDV_{10}Li$ β – CD. This polyrotaxane were synthesised by Dr. Shane O. McDonnel and Prof. Harry L. Anderson (Chemistry Research Laboratory, Department of Chemistry, University of Oxford).
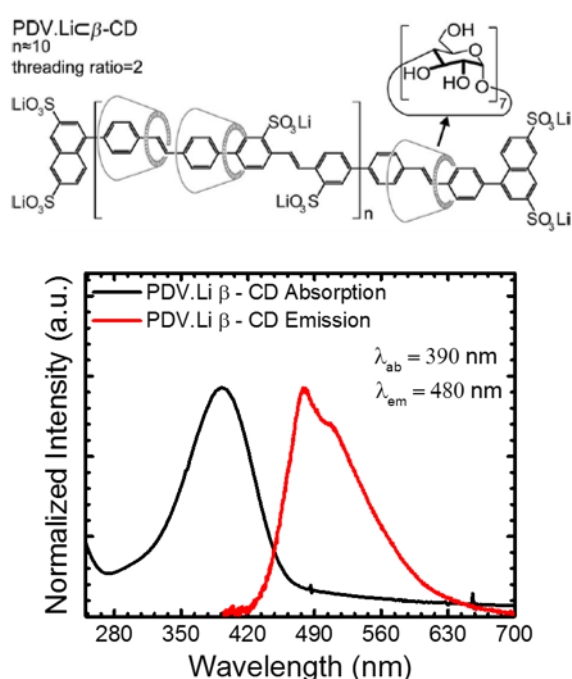
Figure 5.4. Molecular structure of the polyrotaxane PDV_nLi β – CD, average of repeat unit n = 10, and threading ratio = 2 (top). Absorption (black line), and emission (red line) spectra of a spin-coated film of $PDV_{10}Li$ β – CD (bottom).

The obtained synthetic opals are characterised by an fcc array of polystyrene spheres in which the voids are partially filled by $PDV_{10}Li\ \beta - CD$ (see for example figure 5.5). Since the reflectance spectra of rotaxinated opals match the reflectance spectra of bare opals (see for example figure 5.13), I suppose that the $PDV_{10}Li\ \beta - CD$ does not expand the photonic structure during the co-growth, it fits the fcc voids, instead. As for the bare opals, the substrates used to fabricate fluorescent PhCs are commercial soda-lime glass microscope slides previously cleaned by a basic piranha solution.
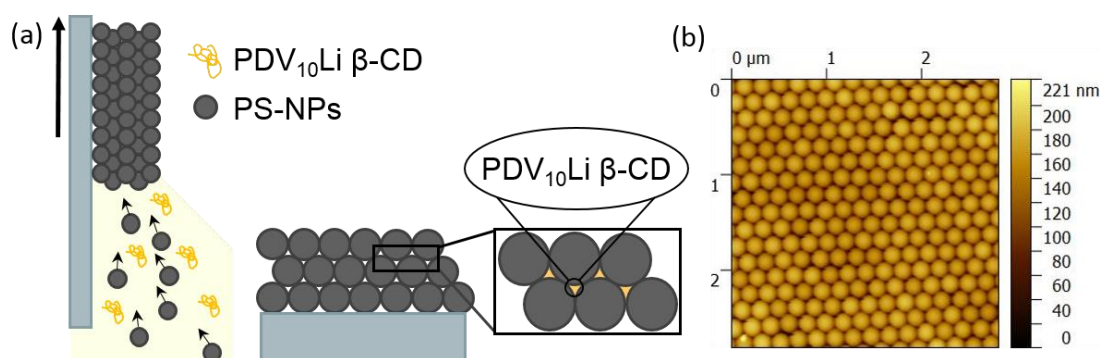
Figure 5.5. Schematic representation of the polystyrene sphere/polyrotaxane co-growth. The PS-NPs self-assemble at the interface between the meniscus of the aqueous solution and the glass substrate, while the $PDV_{10}Li\ \beta - CD$ macromolecules fill the fcc voids (a). AFM image of luminescent opals based on PS-NPs with a diameter of 200 nm (b).

In order to study the photonic effect on the spontaneous emission of the polyrotaxane embedded into opal, a reference sample was used. The latter is the very same opal under investigation but thermally annealed at 75°C for 5 minutes. Such thermal annealing is enough to melt the polystyrene spheres destroying the photonic properties of the structure but preserving the PL properties of the emitter, due to the higher thermal stability of this class of supramolecular system. To demonstrate the melting effect on the photonic optical properties, I collect the emission spectra of the melted rotaxinated opal changing the angle of incident light. The emission curves are the same for all the detected angle (dashed line in figure 5.15).

5.2.3   Behind the scene of opal fabrication

Although direct opals are deeply studied and the vertical deposition method is well known, I would like to point out some issues I came across during my experiments.

1. The vertical deposition technique is a slow fabrication method (opal fabrication take up to 5 days), and it is highly sensitive to environmental conditions, such as humidity, temperature, and external vibrations. I did not have a humidity sensor, but I used to perform experiments under controlled external (room 19°C) and internal (incubator 45°C) temperature. Furthermore, the opals growth took place on an optical table to minimise vibrations deleterious for the opal periodicity.

2. The nanoparticle concentration of the colloidal suspension needs to be carefully calculated in relation to the substrate dimensions. For high concentrations, the long-range order of the final structure is not guaranteed, the thickness of the sample increase making transmittance experiments impossible to perform. Furthermore, opals result incredibly fragile. On the other hand, if the nanoparticle concentration is low the nanoparticles do not arrange as an fcc array, and the thickness of the structure will be not enough for reflectance measurements.

3. The polyrotaxane was successfully incorporated after a careful investigation of the infiltration methods, and calculation of the concentration of the polyrotaxane solution. Before choosing the co-growth technique, I attempt different methods for incorporating the $PDV_{10}Li$ β – CD into the direct opals, examples are drop-casting, dip coating, and femtojet. As it is clear from figure 5.6, all these methods destroyed the sample. On the contrary, as discussed in this chapter,

the co-growth method allows the incorporation of the polyrotaxane into the direct opal, without deforming the fcc structure.
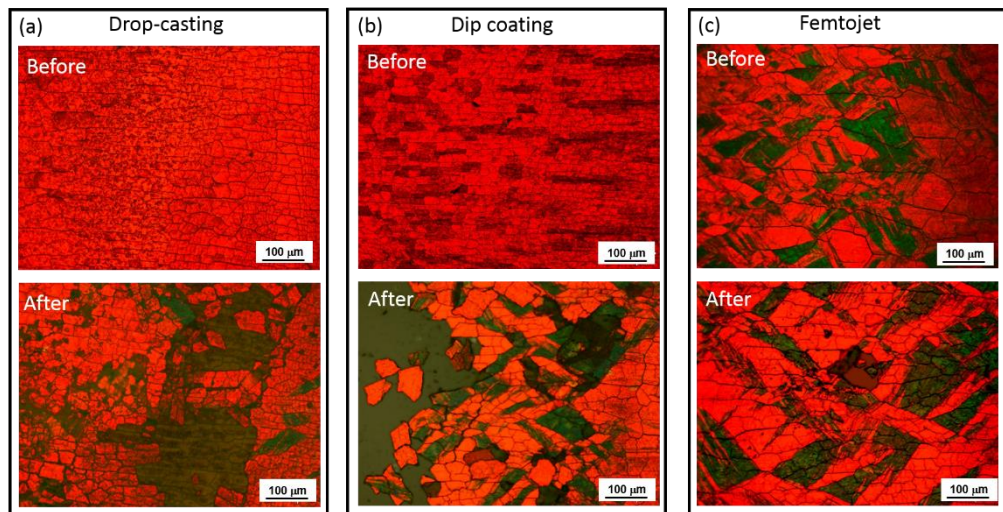
Figure 5.6. Microscope images (magnification 10 x) of bare and loaded opal by dip coating (a), drop casting (b) and femtojet methods (c)

For high concentrations of polyrotaxane, the excess will deposit on top of the sample avoiding the detection of the photonic effect on the spontaneous emission. The polyrotaxane emission coming from the top layer will cover the emission of the polyrotaxane infiltrated in the opal voids. However, If the concentration is low the emission intensity will be not strong enough to be detected.

In conclusion, it is important to consider different aspects of the experimental parameters to obtain high quality opals for light manipulation.

5.2.4 Optical measurements

Bare and fluorescent opals were investigated by normal reflection and angle-resolved transmittance measurements. In addition, the photoluminescence spectra were collected for the optical study of fluorescent opals.
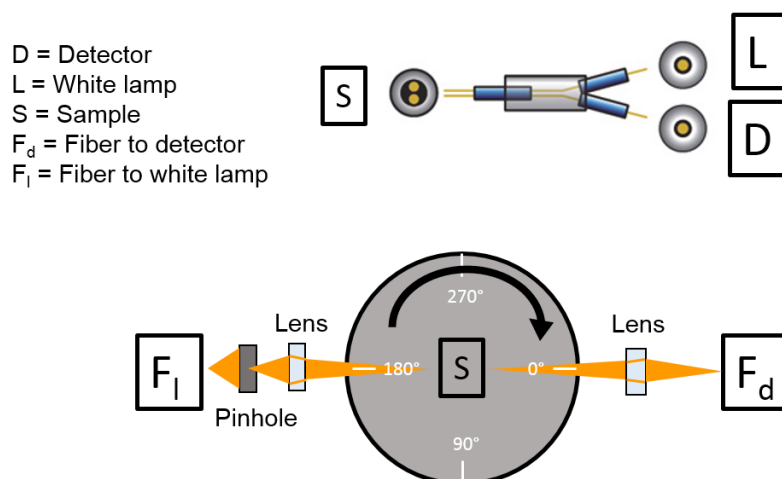
Figure 5.7. (a) Schematic representation of the bifurcated fibre used for normal reflection, and (b) the set-up used for angle-dependent transmission. The grey circle represent a large-area rotating breadboards (goniometers).

Figure 5.7 shows a schematic representation of the home-made optical set-up used to perform reflection and transmission measurements. For the reflection measurements (see for example figure 5.7-a), I used an Ocean Optics bifurcated fibre together with the HL-2000 tungsten halogen lamp, as light source (L). The sample (S) were fixed horizontally on a black sample holder. On the contrary, for the transmission measurements (see for example figure 5.7-b), the sample (S) were free to rotate. The opals were mounted on a rotating stage (big grey circle) allowing the transmission collection at different incidence angles (θ), in the range 0°-70°. The large-area rotating breadboards is a goniometer (by Thorlabs) having a diameter of 18 inch and a scale from 0° to 360° with steps of 1°. The detector and the lamp (Ocean Optics HL-2000 tungsten halogen source) were fixed on an optical table and connected towards the sample by two optical fibres, F_d and F_l, respectively. Normal reflection and angle-

dependent transmission setups are based on an Avantes 2048 compact fibre optic spectrometer working in the range 250-1100 nm with a resolution of ~1.5 nm (D).
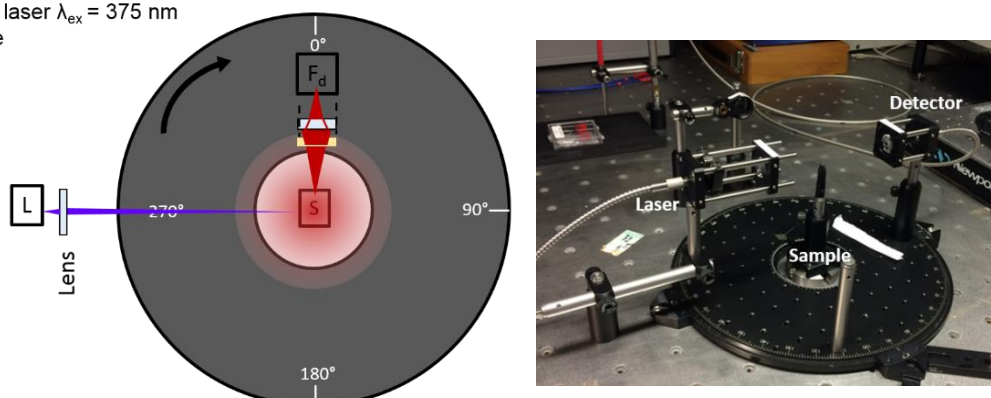
Figure 5.8. Schematic representation (left) and photo (right) of the set-up used for angle dependent PL. The grey circle represent the goniometers, the sample (S) and the laser (L) are placed on the optical table, while the detector (F_d) is placed on the goniometers, so it can rotate..

PL measurements were realized in the dark and in backscattering geometry recording emitted light coming out from the opal side (not from the slide side). The excitation light used for the PL experiment was the pulsed laser diode (λ_{ex} = 375 nm, pulse width ~ 60 ps). For angle resolved PL measurements (see for example figure 5.8 for the schematic representation and the picture of the home-made set-up), the laser (L) and the sample (S) were kept fixed on the optic table, whereas the collection fiber (F_d) connected to the Andor Shamrock 163i spectrometer (coupled with an Andor Newton CCD camera cooled at -50 °C) was rotated between 0° and 80°.

5.3 Results and discussion

5.3.1 Optical properties of bare opals

In order to verify the efficacy of the vertical method, I studied the direct opals by normal reflectance and angle resolved transmittance measurements. Figure 5.9-a shows the normal reflectance spectra related to polystyrene opals made with different spheres diameters (i.e. d = 220, 260, 300 and 340 nm). In agreement with the

theoretical works discussed in the section 5.1 [61,62], the spectra display an intense peak corresponding to the PSB, and a group of bands at shorter-wavelengths due to diffractions from planes different from the (111) and which strongly depend on the internal fcc order [61]. For example, opals made by sphere of 340 nm (blue curve) have the PSB centred at 765 nm and the high-energy bands between 390 nm and 440 nm. The 300 nm-opals (green curve), are characterised by a PSB at 680 nm and by the high-energy bands centred between 350 nm and 385 nm. The 260 nm- (red curve) and the 220 nm-opals (black curve) present the PSB at 575 nm and 507 nm, respectively, while the high-energy bands are between 278 and 340 nm. Furthermore, as expected from the Bragg-Snell law (see equation 5.2, page 65), the PSB position depends also on the sphere diameter, *d*, used to prepare opals. Precisely, the maximum of the wavelength of the PSB red-shifts by increasing the diameter *d.* This trend is clearly visible in table 5.1 and in figure 5.9-b. Figure 5.9-b displays a linear and ascending trend of the experimental PSB peak (from λ = 507 nm to λ = 765 nm) (black dots) by increasing the sphere diameters (from d = 220 nm to d = 340 nm) and according to the calculated PSB peaks in table 5.1. In addition, the peaks of the high-energy bands present the same behaviour compared to the PSB peaks. By increasing the sphere diameters from 220 nm to 340 nm, the appearance of the high-energy bands is red-shifted by 150 nm (red dots in figure 5.9-b). In table 5.1, the PSB position calculated by using the Bragg-Snell law for each sphere "nominal" diameter was compared with the experimental reflectance peaks showed in figure 5.9-b.

Since the PSB corresponds to the first Bragg peak (m = 1) observed along the ΓL direction (θ = 0, $sin^2\theta$ = 0), the Bragg-Snell law can be written as

$$\lambda = 2dn_{eff}\sqrt{\frac{2}{3}} \qquad\qquad 5.3$$

where n_{eff} for polystyrene opals is ~1.46. This is estimated by means of the following expression

$$n_{eff}^2 = 0.74\, n_{PS}^2 + 0.26\, n_{air}^2 \qquad\qquad 5.4$$

where n_{PS} and n_{air} are, respectively, the refractive indexes of polystyrene particles (n_{PS} = 1.59) and air voids (n_{air} = 1), whereas 0.74 and 0.26 are their associated theoretical volume filling fractions. The refractive index value of the polystyrene nanoparticles was given by the nanoparticle supplier, Duke Scientific.
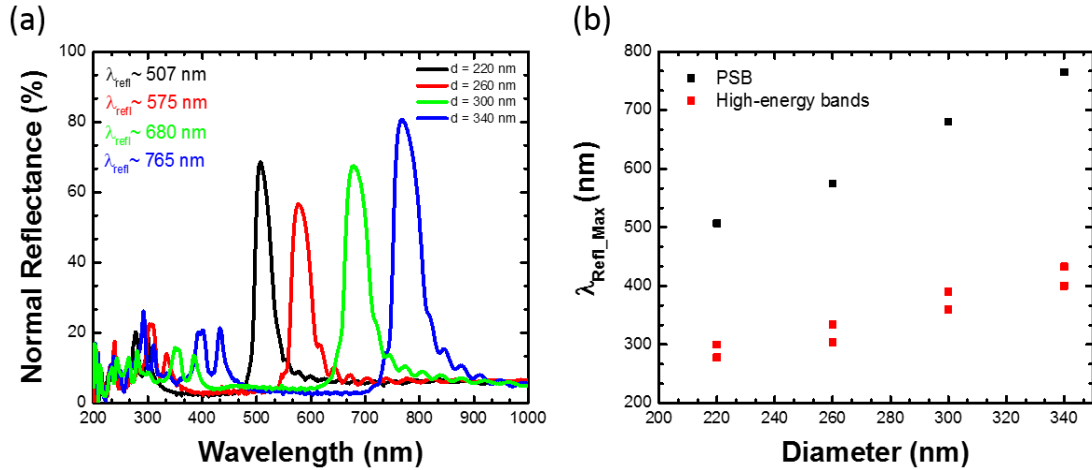
Figure 5.9. Normal reflectance spectra of polystyrene opals made with different sphere diameters (d = 220, 260, 300 and 340 nm) (a); plot of the PSB and high-energy bands peaks as a function of the sphere diameters (b).

Sphere diameter (nm)	Calculated PSB peak (nm)	Experimental Reflectance peak (nm)
220 ± 11	524 ± 25	507 ± 1.5
260 ± 13	620 ± 30	575 ± 1.5
300 ± 15	715 ± 35	680 ± 1.5
340 ± 17	810 ± 40	765 ± 1.5

Table 5.1. Comparison between the calculated PSB peak using the Bragg-Snell law, and the experimental PSB position in the normal reflectance spectra. The values of the sphere diameter and their value are given by the nanoparticle supplier, Duke Scientific.

Considering the 5% standard deviation of the nominal sphere diameters (data given by the nanoparticle supplier, Duke Scientific), can be concluded that there is a good agreement between the theoretical and the experimental PSB peaks. Such agreement shows how vertical method techniques deliver top-quality polystyrene arrays for optical performances of direct opals.
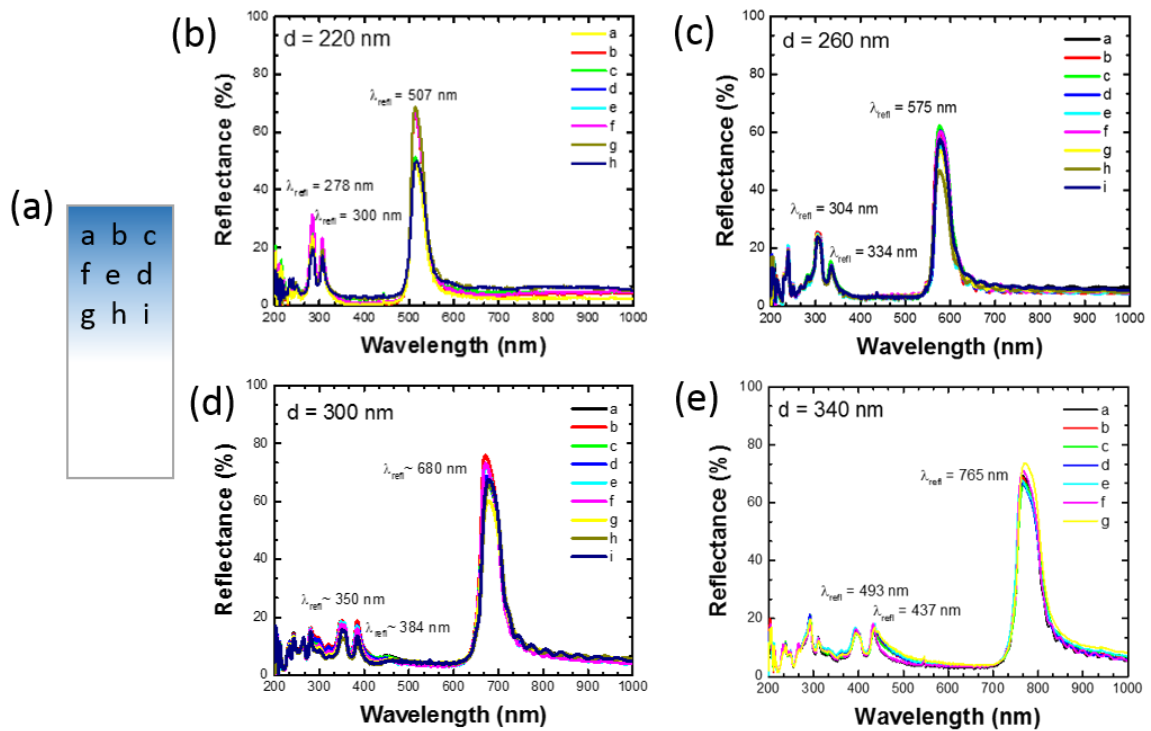
Figure 5.10. Legend of the opal region analysed by reflectance measurement (a), normal-reflectance spectra of opals base on polystyrene nanoparticles with diameters of 220 nm (b), 260 (c), 300 nm (d) and 340 nm (e).

Further indication of the excellent quality of the microstructure array is given by the agreement between the normal reflectance spectra collected in different spots of the same sample. To this aim it is worth discussing figure 5.10. Its panel "a" is a schematic representation of the sample of interest: marked in blue, and by letters "a" to "i" to indicate the zone where the reflectance spectra are collected, is the glass slide covered by the photonic array; in white colour is the glass substrate. The remaining "b" – "e" panels show the reflectance spectra collected along the ΓL direction for the 220 nm-, 260 nm-, 300 nm- and 430 nm-opals, respectively. The spectral position of the PSB is unchanged for all samples, and it has its maximum for each respective sample at the following values: 507 nm for the 220 nm-opal, 575 nm for the 260 nm-opal, 680 nm for the 300 nm-opal and 765 nm for the 340 nm-opal. Moreover, the ordered

arrangement of spheres in photonic crystals is underlined by the consistency of the spectral position and shape of the high-energy bands, all over the sample.
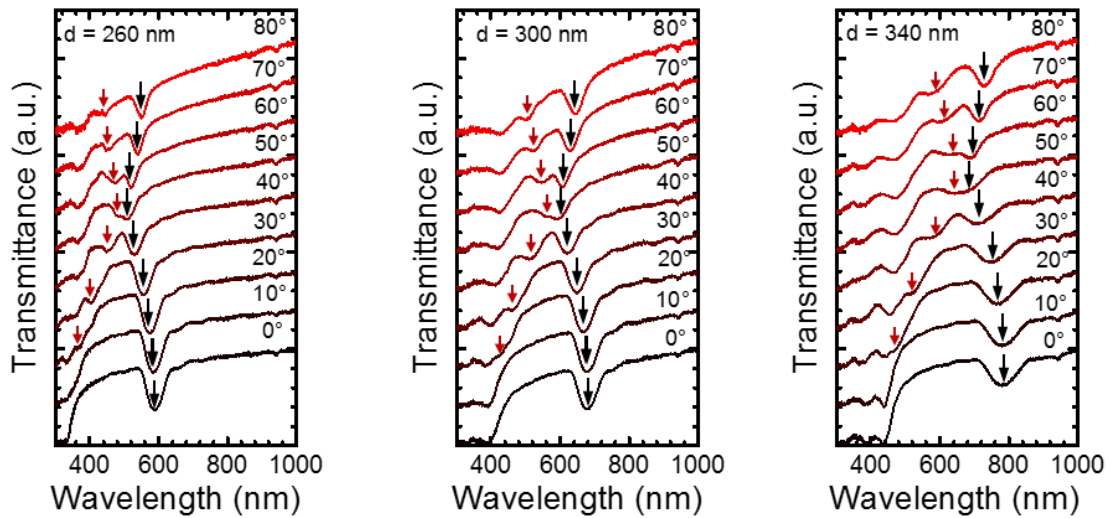
Figure 5.11. Angle-dependent transmission spectra of 260 nm (left), 300 nm (centre), and 340 nm (right) opals. The black arrows show the PSB trend by changing the angles of the incidence light, while the red arrows are representative of the high-energy band tendency.

In order to investigate the dispersion of the photonic bands, I collected the transmittance spectra at different angles of the incidence light, from 0° to 80° with a step of 10°. The angle-dependent transmittance is reported in figure 5.11 for the 260 nm- (left panel), the 300 nm- (central panel) and for the 340 nm-opals (right panel). Coloured arrows are used to facilitate the identification of both the PSB and the high-energy bands, otherwise ambiguous. The PSB produced by the (111) planes (black arrows) presents a blue-shift of 50 nm, 80 nm, and 100 nm, for the 260nm-, 300nm-, and 340nm-opal, respectively, at low angles 0°< θ < 50°. Conversely, the high-energy bands (red arrows) shift to higher wavelength until the PSB is reached at 50°. At this angle, the PSB and the high-energy bands display an anticrossing so that at higher angles (60°< θ < 80°), the transmittance bands display the opposite behaviour. The PSBs evolve towards higher wavelength whereas the high-energy bands shift to lower values of λ [63]. The angle-dependent transmission spectra in fig 5.11 are in agreement

with the photonic band study of D. Comoretto in ref 61. The observation of several photonic bands having a well-defined trend is a proof of the high quality of my crystals.

The results discussed prove that the vertical method used for opals preparation brings to high ordered photonic structures without implementing expensive fabrication techniques. Therefore, I made full use and I derived all benefit of the vertical method in order to incorporate a polyrotaxane dye within opals and to study its emission in correspondence of the PSB and of the high-energy bands.

5.3.2 The effect of the PSB on polyrotaxane emission
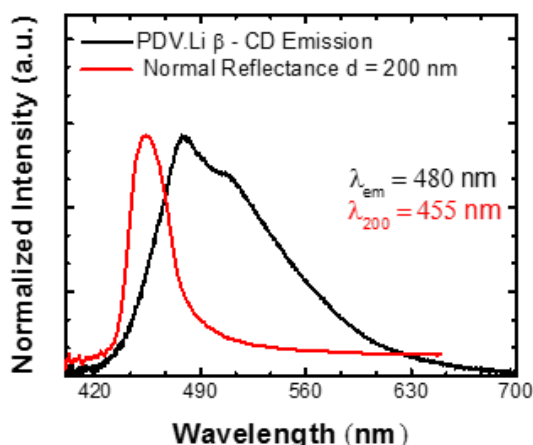
Figure 5.12. Emission spectra of a PDV$_{10}$Li β – CD spin-coated film (black curve) with, superimposed, the normal reflectance spectra (red curve) of a bare opal with nanoparticles of 200 nm of diameters.

As discussed before, the existence of the spectral overlap between the PSB and the polyrotaxane emission is crucial to observe the PL modification caused by photonic effects. Figure 5.12 shows in red the curve for the normal reflectance of a bare 200 nm–opals and in black the emission curve of the polyrotaxane. The spectral overlap occurs between the high-energy side of the polyrotaxane emission and the 200 nm-opal PSB. This means that the suppression/enhancement of the

photoluminescence of PDV$_{10}$Li β – CD is expected in the range between 420 nm and 490 nm. In order to ensure this spectral overlap, I prepared fluorescence opals of polystyrene spheres with a diameter of 200 nm (see section 5.2.2 for the preparation method).
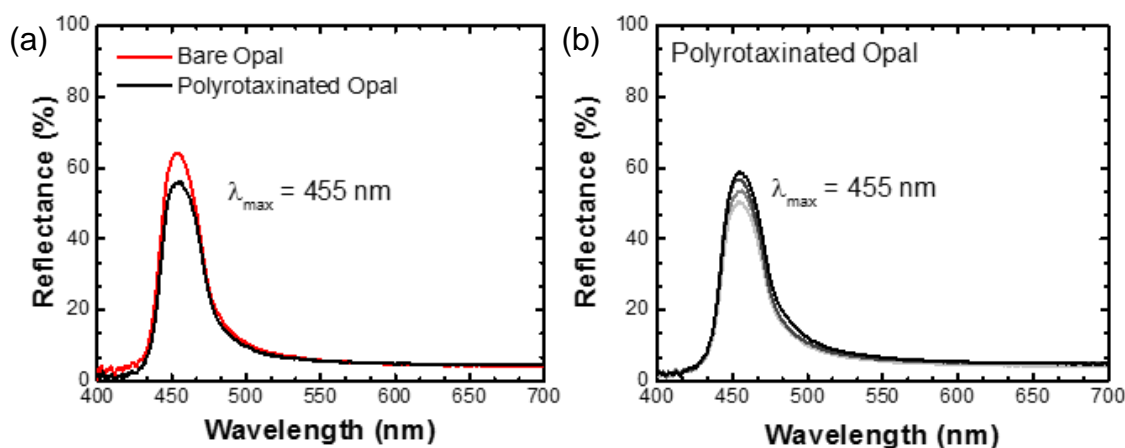
Figure 5.13. (a) Normal reflectance of bare (red curve) and rotaxinated opal (black curve). (b) Normal reflectance collected in different spot of the rotaxinated opal surface.

To verify the quality of the co-growth opals, the reflectance spectra of the fluorescent opal is compared to the one of the bare opals. Figure 5.13-a shows a good agreement between the two spectra in terms of peak energy (λ$_{max}$ = 455 nm) and intensity of reflectance (R ~ 60%). Furthermore, the reflectance percentages collected in different regions of the sample slightly change so that its variation can be negligible (see for example figure 5.13-b). These results prove the preservation of the fcc structure of the opals even after rotaxane incorporation.

Looking at the figure 5.14-a and –b, I would like to note that the PDV$_{10}$Li β – CD emission is strongly modified by the photonic band structure. First of all, by comparing the emission of the fluorescent opal to the emission of the rotaxane neat-film (figure 5.14-a), a 30 nm blue-shift is observed (from ~ 450 nm to ~ 440 nm). Moreover, an increase of the PL quantum yield is also measured, from ϕ_{PL} = 18 ± 2% for the neat-film rotaxane to ϕ_{PL} = 35 ± 3% for the rotaxinated opal. Such blue-shift and ϕ_{PL} are probably due to the electrostatic interactions of the Li$^+$ cations of the PDV$_{10}$Li β – CD with the negatively charged surface of the polystyrene microspheres. In addition,

due to the preparation method, that induces strong capillary forces [67], and to the internal geometry of the crystal, the polymers may undergo structural constraints. This leads to a modification of the PL dynamics of the polyrotaxane compared to that observed in a neat-polymer film [48]. More importantly, the PL of the rotaxinated opal presents a partial suppression exactly in correspondence of the maximum in reflectance at 0° incidence (from ~ 443 nm to ~ 465 nm) of the opal (figure 5.14-b). This evidence confirms what predicted in section 5.1.2: in correspondence of the photonic stop band, which is defined by a depression in the DOS, the PL can be partially or completely suppressed.
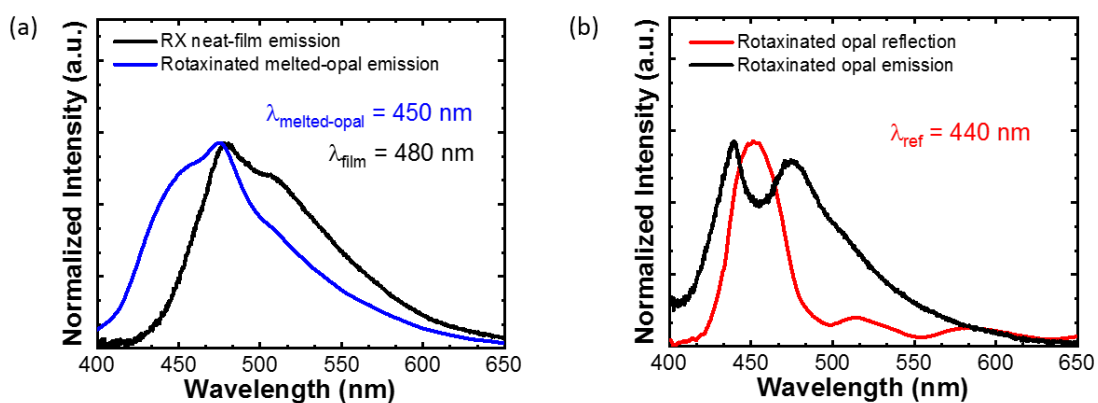
Figure 5.14. Emission spectra of the spin-coated pure polyrotaxane (black curve) and of the rotaxinated melted opal, i.e. reference (blue curve) collected at 0° (normal incidence) (a); spectral overlap between the emission and the normal reflectance curves for co-growth opal made with spheres having diameter 200 nm, black and red curves, respectively (b).

In order to appreciate the effect of the PhCs on the spontaneous emission of the rotaxane, the angle-resolved PL spectra for the infiltrated opal (red curves) are reported in figure 5.15-a together with the PL curves of the reference sample (black dashed). In order to compare the emission curves, both the PL measurements were executed in the same area of the sample and the PL spectra were normalized. The emission of the rotaxinated opal is partially suppressed in correspondence of the stop-band, for all the incidence angles (from 0° to 40° with a step of 5°). Moreover, there is an enhancement of the PL intensity at the high-energy edge of the stop-band. Both enhancement and suppression have the same dispersion as the stop-band, thus

suggesting that both effects are connected to a directional redistribution of the photonic density of states [68,69]. The enhancement/suppression effects are better appreciated in the ratio between the two PL spectra in figure 5.15-b. In correspondence of the PSB, between $\lambda \sim 443$ nm and $\lambda \sim 465$ nm, the ratio is < 1, whereas it is > 1 at the short-wavelength edge of the PSB (below 450 nm).
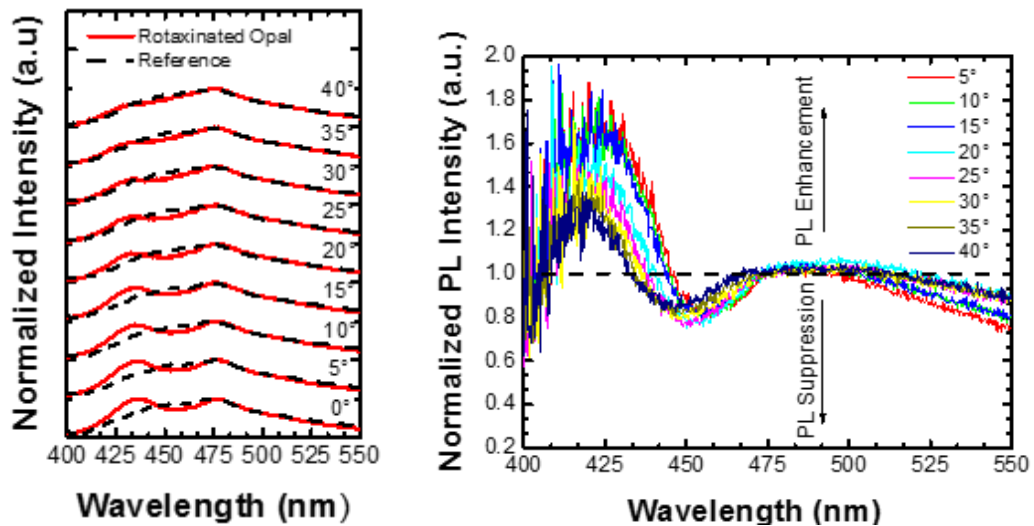
Figure 5.15. Left: PL spectra of the rotaxinated opal before (solid line) and after (dashed line) the thermal treatment, at different angles of light collection; Right: Ratio between the angle-dependent emission of the co-growth opal (PhC) and the reference opal (Ref).

The results in this section are in agreement with the ones obtained by former members of the group of Franco Cacialli [59]. The strong match of the experimental evidence between the work of F. Di Stasio and the present one validate the vertical methods as a reliable technique also for the preparation of fluorescent opals.

5.3.3 The effect of the high-energy bands on polyrotaxane emission

This section is focused on the effect of the direct opals high-energy bands on the emission of $PDV_{10}Li$ β – CD. The samples studied are co-grown rotaxinated opals made with spheres having a diameter of 260 nm, 300 nm, and 340 nm (the preparation method is explained in section 5.2.2).
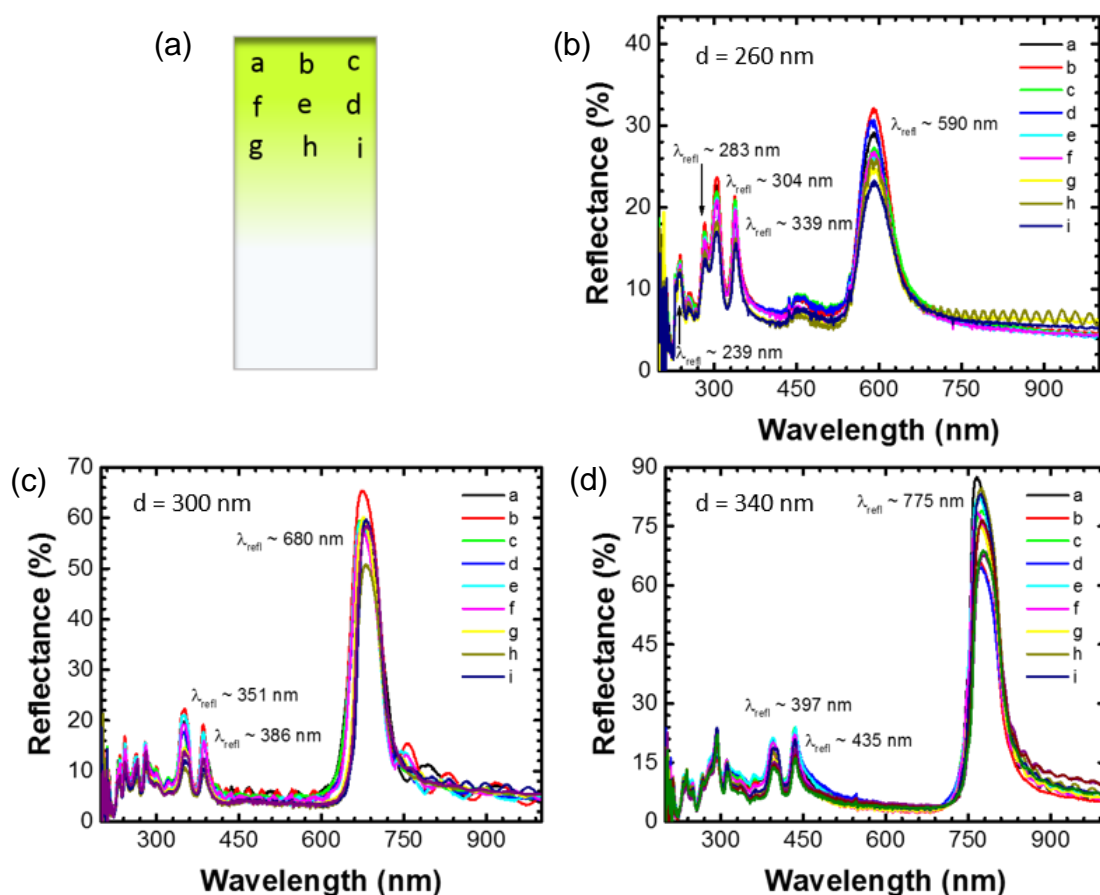
Figure 5.16. Legend of the analysed rotaxinated opal regions (a-i) by reflectance measurement (a), normal-reflectance spectra of opals base on polystyrene nanoparticles with diameters of 260 nm (b), 300 nm (c), and 340 nm (d).

In order to analyse the quality of the photonic structure, the obtained rotaxinated opals were characterized by normal reflectance measurements in different regions of the sample (see for example Fig. 5.16). Figure 5.16-a displays a schematic representation of the sample (the grey part is the glass slide covered by the co-growth

luminescent PhCs, while the white part is the glass slide alone) marked by letters from "a" to "i" to indicate the regions where the reflectance spectra were collected. Figure 5.16 from "a" to "d" shows the reflectance spectra collected along the ΓL direction for the 260 nm-, 300 nm-, and 430 nm-opals, respectively. In all the opals the PSB and the high-energy bands are consistent in terms of wavelength value, across the whole sample. In particular, the spectral position of the high-energy bands cover the range from 283 nm to 389 nm for the 260 nm-opal, from 351 nm to 386 nm for the 300 nm-opal and from 397 nm to 435 nm for the 340 nm-opal. Furthermore, the small variation of the reflectance intensity is negligible for the scope of this thesis.
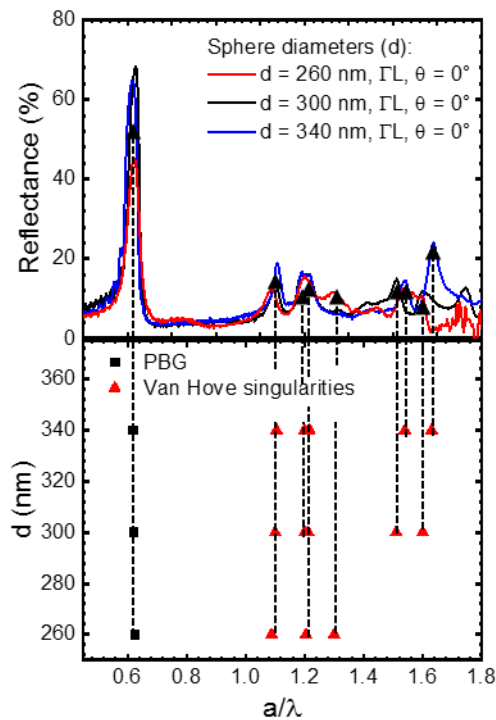
Figure 5.17. Reflectance spectra collected at normal incidence to respect the (111) plane (top graph) of rotaxinated opals made with spheres having a diameter of 260 nm (red line), 300 nm (black line), and 340 nm (blue line). Normal reflectance peaks as a function of the sphere diameters (bottom graph). The spectra are reduced to the dimensionless unit a/λ (where a is the lattice parameter proportional to the spheres diameters, and λ is the wavelength of light).

To demonstrate the photonic nature of the curves in figure 5.16, in addition to the reflectance spectra collected along the ΓL direction of the first Brillouin zone, I investigated the spectral position of the photonic bands as a function of the sphere

diameters. The results are displayed in figure 5.17. Normal reflectance spectra are typical of fcc uninfiltrated opals, demonstrating a good preservation of the photonic properties of the opal, even after polyrotaxane incorporation. Since the spectra are reduced to the dimensionless quantity a/λ, where a is the lattice parameter proportional to the spheres diameters and λ is the wavelength of light, can be conclude that the observed peaks are caused by intrinsic properties of the photonic crystals and the band at $a/\lambda \sim 0.6$ can be associate to the PSB caused by the (111) planes, whereas the multiple diffraction peaks between $a/\lambda \sim 1.1$ and $a/\lambda \sim 1.8$ to the Van Hove singularities which correspond to the diffraction along directions different from the direction of the incidence light.
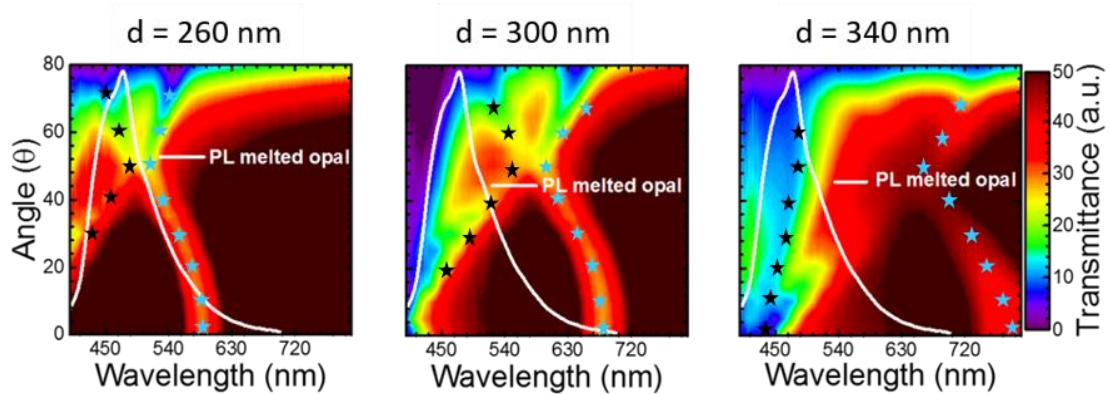
Figure 5.18. Transmittance contour maps of three rotaxinated opals prepared with spheres having diameters of 260 nm (left), 300 nm (centre), and 340 nm (right) respectively, as a function of both wavelength and incidence angle. The emission spectrum of the polyrotaxane in a melted opal is also shown as a white line. The blue and the black stars indicate respectively the peak of the PSB and the high energy bands as a function of the angle of the incidence of light.

Clearly, in order to observe a modification of the emission spectrum of a luminophore embedded in a photonic structure, a spectral overlap is needed between the emission of such luminophore and the relevant photonic band, in this case the opal high-energy bands. For this reason, I prepared rotaxinated opals with spheres of diameter of 260 nm, 300 nm, and 340 nm, respectively, and I am presenting in figure 5.18 the contour maps of their transmittance (presented also in figure 5.19 together with the rotaxinated opal emission) as a function of both wavelength and incidence

angle, as well as the emission of the PDV$_{10}$Li β – CD embedded into the melted opal (see section 5.2.2 for the reference preparation).

Looking first into the sphere size dependence, I would like to note, as expected, that both the PSB (blue stars) and the high-energy bands (black stars) shift to higher wavelength with increasing sphere diameters until the spectral overlap between the PL and PSB disappears. At the same time, the overlap between the PL and the high-energy bands reaches its maximum for opals made with spheres of diameter of 340 nm. At 0° of incidence light, respectively for the 260 nm-, 300 nm- and 340 nm-opal, the PSB has a peak at 590 nm, 680 nm, 775 nm, while the high energy bands have the first peak at 339 nm, 386 nm and 435 nm. Hence, for opals made with spheres of 300 and 340 nm, the PSB-dependence of the emission is expected to decrease in favour of high-energy bands influence.
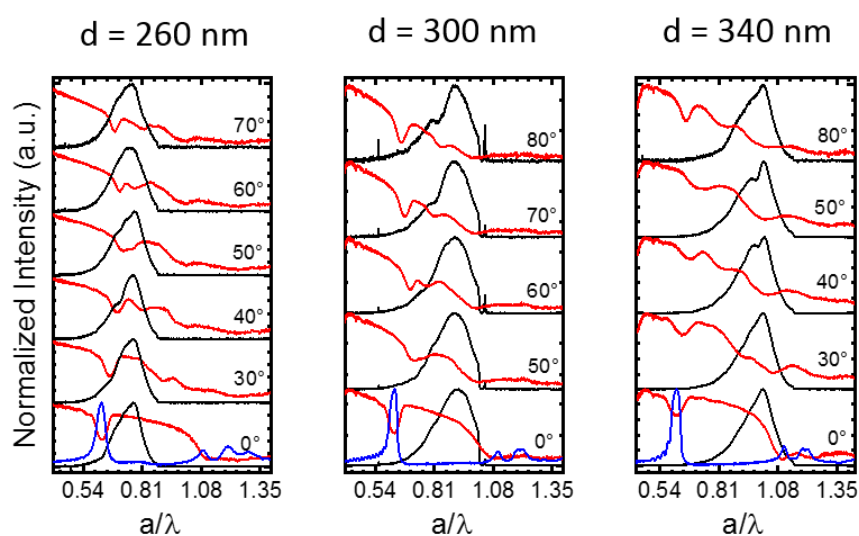
Figure 5.19. Angle-dependent PL spectra (black curves) of rotaxinated opals based on different sphere diameters, 260 nm (left), 300 nm (centre), and 340 nm (right), overlapped with their angle-dependent transmission curves (red lines). At 0° of incident light the reflectance spectra (blue lines) have been added to better visualise the photonic high-energy bands.

In order to demonstrate the dependence of the emission on the high-energy bands, the PL spectra of the rotaxinated opals were collect in overlap with the transmittance spectra as a function of the incidence light. The opal reflectance curves (blue lines) have been added in the graphs to better display the spectral position of the

high-energy bands at 0° of incidence light, otherwise covered by scattering effects. As illustrated in figure 5.19, the PL (black spectra) of the 260 nm-opal is slightly affected by the PSB (red curve) only between 0° and 30°, leading to modifications only of the lower-energy edge of the PL curve. By increasing the angle of the incident light up to 50° the contribution of the high-energy bands emerges, and, in good agreement with the transmission measurements, the emission alteration follows the anti-crossing path of the photonic bands, i.e. a second and a third peak appear at $a/\lambda = 0.7$ and $a/\lambda = 0.74$ for, respectively, 40° and 50°, together with a spectral broadening. For angles higher than 50°, the splitting of the transmission characteristics decreases the modification effect on the PL. The photoluminescence of 300 nm-opal displays a different dependency on transmission: the related emission spectra are not affected by photonic bands until the PSB meets the high-energy bands at 50°. At this angle, a shoulder emerges on the PL spectrum at $a/\lambda = 0.75$, which corresponds to the photonic bands crossing-energies. By increasing the incidence angle up to 80°, according to the Bragg-Snell law, the PSB moves towards lower energies decreasing the overlap with the PL, while the high-energy bands delineate the emission peak at $a/\lambda \sim 0.8$. Regarding the 340 nm-opal, the PSB effect vanishes due to the zero-spectral overlap between the PL and the transmittance measurements. This occurs over the whole range of incidence angles investigated. Indeed, the suppression of the PL follows the trend of high-energy bands. Their influence starts at 30° and it becomes stronger for higher angles (40° and 50°) where a greater spectral overlap appears, resulting in a well visible second PL peak at $a/\lambda = 0.95$. It is clear that for the rotaxane embedded into opals with a PSB totally overlapped with the PL spectra (260 nm spheres), the modulation of its emission is affected mostly from the PSB in all the angles spanned. On the other hand, when the PSB is out of the rotaxane PL wavelengths, the emission (for 300 and 340 nm sphere diameters) is controlled mainly by the higher energy bands. The PBG contributes to the spectra modification at higher angles ($50° < \theta < 60°$), only in the case of opals made with 300 nm sphere diameters. Moreover, the

evidence of the photonic effect on the rotaxane emission is given by the increase of the PL efficiency from $18 \pm 2\%$ for the neat spin-coated film, to $33 \pm 3 \%$ for the fluorescent opals.

This work demonstrates how the photonic properties of direct opals affect the emission of the rotaxane $PDV_{10}Li \beta - CD$ when the sphere diameters used to fabricate the photonic crystals are modified. The interplay between the opposite angular dispersion of photonic bands and the diameter-depending spectral overlap is crucial for the modification of the PL spectra of the embedded material. In particular, I fabricated high-quality photonic crystals and I observed for the first time the complex influence of the photonic high-energy bands on polyrotaxane spontaneous emission.

Chapter 6. Tuning of the photonic stop bands in silica inverse opals

Inverse opals are ordered 3D porous structures in which spherical cavities are close-packed in an fcc array of high refractive index material. The large refractive index contrast has the potential to produce a full photonic band gap useful to a variety of applications in different fields running from light manipulation to (bio)sensing. This chapter introduces a new method for preparing silica inverse opals able to tune the photonic band gap by simply controlling the contents of the silica precursor. Furthermore, two applications of such structure are presented in order to demonstrate the efficiency of the fabrication technique. Firstly, an overview of the photonic effect on the radiative properties of a conjugated polymer (i.e. PDPV) highlights the potential of inverse opals as light manipulators. Secondly, the same opals were exploited as bio-sensor for bovine serum albumin (BSA) monitoring in collaboration with Prof. Giuseppe Barillaro from University of Pisa.

6.1 **Introduction to inverse opals**

The preparation of inverse opals consists on the infiltration of the interparticle voids of synthetic opals with materials of high refractive index, followed by removal of the opal template. Three steps are generally considered for the preparation of the inverse opals: (1) the fabrication of the opal template, for example via sedimentation, spin-coating and evaporative deposition, (2) the infiltration of high refractive index materials, i.e. SiO_2, TiO_2 and Al_2O_3 precursors, respectively, and (3) the removal of the spheres, for example by calcination or chemical etching. However, it has been demonstrated that a single step fabrication is possible by co-assembling polymeric

spheres with a matrix materials (i.e. silica precursor), followed by removal of colloidal template [70,71]. This methods generates large-area and crack-free inverse opals. The co-assembly of the spheres with the silica precursor implies the ability of the spheres to self-assemble onto a substrate, and simultaneously the ability of the silica precursor to fill the voids. The fabrication methods based on colloidal self-assembly are various and each one is based on different forces as gravitational and capillary force or electric and magnetic fields [72-74]. Among the simplest methods, the vertical deposition *via* evaporation leads to high quality ordered structure by the exploitation of capillary interactions. More in details, an fcc array is created at the interface between the solution meniscus and a substrate vertically removed from a mixture of silica precursor and colloidal spheres. Opal templates can be made by silica, polystyrene (PS) or polymethylmethacrylate spheres. However, in this thesis only inverse opals prepared by PS templates are presented. In contrast to silica spheres, polymeric one are easily removed by solvents, plasma treatment, or calcination at temperatures above their glass transition.

The fabrication technique, the lattice constant, the refractive index contrast, and the degree of filling fraction can produce a full or incomplete photonic band gap in the near infrared and visible range [75]. Up to now, the tuning of the photonic band gap has been realized by implementing the best infiltration method for opal template (i.e. impregnation with liquid precursor or sol–gel, chemical vapour deposition, atomic layer deposition, electrochemical deposition) or by changing the spheres diameters of the opals template for the one-step fabrication technique [9]. The work discussed in this chapter completes these studies by promoting a new method for controlling the photonic band gap position in a single step fabrication without changing the spheres diameters of the opal template. By adjusting the content of the silica precursor, the refractive peak of inverse opals shifts toward lower wavelengths without decreasing the PhCs ability to efficiently manipulate light. Hence, after the infiltration of a polymeric

dye into the photonic structure, I observed a significant photonic control of the radiative properties (PL quantum efficiency, lifetime and radiative rate) of the polymer. Moreover, in order to highlight the effectiveness of this fabrication method, inverse opals were used as porous scaffold bio-sensor for the detection of bovine serum albumin (BSA) by using a technique namely interferogram average over wavelength reflectance spectroscopy (IAWRS).

6.2   **Experimental methods**

6.2.1 Inverse opal preparation

Silica inverse opals were prepared by the evaporative co-assembly of polystyrene microparticles with a sol-gel solution contain the silica precursor. The inverse opal is obtained in a single step, avoiding cracks caused by the liquid infiltration on prefabricate porous structures. More specifically, a glass substrate is slowly extracted from 5 mL of an aqueous suspension of polystyrene monodispersed microsphere (Duke Scientific polystyrene microparticles, 10% in volume having diameter of 370 nm, standard deviation 5%, refractive index 1.59), diluted to 2% in volume, also containing x mL of hydrolyzed tetraethoxy silane (TEOS) solution, where x was varied from 15 µL to 90 µL. The standard TEOS solution consists of 1:1:1.5 ratio by weight of TEOS (98% Aldrich), 0.10 M HCl, and EtOH (100%), respectively, stirred at room temperature for 1 h prior to use. The substrates adopted for growing opals are commercial soda-lime glass microscope slides (original dimension 25x75x1 mm; final dimension obtained by cutting the slides using a diamante tip ~ 10x30x1 mm). Once cleaned in a bath of basic piranha (3:1:1 mixture of ammonia, water and hydrogen peroxide) [66], the slides were immersed perpendicularly into the colloidal/TEOS suspension and were extracted at constant speed of 6.5×10^{-5} mm/s at 45°C ± 1°C by using a home-made dip coater with a motorized translation stage (by Thorlabs) (see

figure 6.1 for the scheme of evaporative co-assembly technique). The opals growth took place into a BF53 Binder incubator located in an optical table to minimise vibrations deleterious for the opal periodicity. The samples was then fired at 500°C for 2 hours, with a 4 hours ramp in order to remove the polymer template and partially sinter the silica structure. The obtained synthetic opals have an area of 1.5 x 1.0 cm and a thickness off ~ 5 µm (see SEM image in figure 6.1).
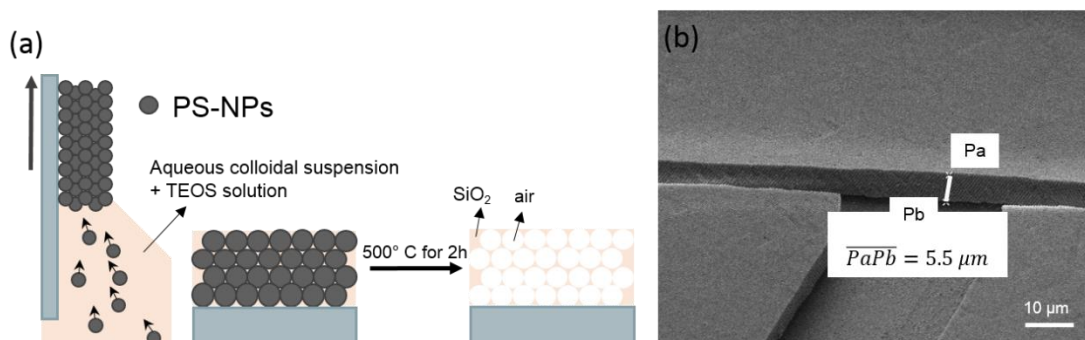
Figure 6.1. Schematic representation of the evaporative co-assembly technique for inverse opals preparation. The PS-NPs self-assemble in a face-centred-cubic array at the interface between the colloidal/TEOS meniscus and the glass substrate. The silica precursor fill the voids between the spheres generating the inorganic matrix. The inverse opals structure are obtained after sample calcination at 500°C for 2 hours (a). SEM image of an inverse opal prepared by vertical deposition (b). The thickness of the resulted structure is 5.5 µm.

The preparation of the samples for PDPV optical study and for bovine serum albumin detection are described in details in section 6.3.

6.2.2 Characterisation techniques

Bare inverse opals were characterised by normal reflectance and scanning electron microscopy. The study of the PDPV emission when infiltrated into the inverse opals were carried out by measuring the normal reflectance, the angle-dependent transmission and photoluminescence, the PL efficiency, and the PL-decay. The bovine serum albumin (BSA) were monitored by using a technique namely interferogram average over wavelength reflectance spectroscopy (IAWRS) that is discussed on section 6.3.

The set-ups for normal reflectance, angle-dependent transmittance and photoluminescence measurements are extensively described in chapter 5, section 5.2.3. PL efficiency were measured by using a 405 nm Oxxius diode laser (model LBX-405-100-CSB-PP) with a maximum power of 50 mW and an integrate sphere as explained by J. C. de Mello [76]. The Radiative decay of the photoluminescence of the PDPV were measured by time-correlated single-photon counting, TCSPC. The system used in this thesis was an Edinburg Instruments F900-red TCSPC, with the Oxxius diode laser (405 nm excitation) and a cooled photomultiplier tube coupled with a monochromator as detector. Images of inverse opals were collected by using the SEM mode of a dual beam Carl Zeiss XB1540 Cross-Beam focussed-ion-beam microscope.

6.3   **Result and discussion**

Silica inverse opals were prepared by varying the contents of TEOS solution that was added to the colloidal suspension of polystyrene microparticles. The photonic structure obtained after calcination of the polystyrene spheres were then characterised by normal reflectance measurements, and the experimental reflectance peak were compared with the calculated one. For the inverse opals, the peak of the photonic band gap can be estimated by the Bragg-Snell law written as

$$m\lambda = 2d \sqrt{\frac{2}{3}[f_v n_1^2 + (1 - f_v)n_2^2]} \qquad (6.1)$$

where d is the spherical void diameters, n_1 is the refractive index of the void and, n_2 is the refractive index of the filled space, f_v is the void fraction, and $(1 - f_v)$ is the volume-filling fraction. Considering that $n_1 = 1$ and $n_2 = 1.47$ are the refractive index for air and silica, respectively, and that for an ideal fcc-lattice $f_v = 0.74$ and $(1 - f_v) = 0.26$, the peak of the photonic band gap is estimated to be 688 nm, for inverse opals made using spheres with a diameter of 370 nm. However, the reflectance spectrum in figure 6.2-a

shows a peak at 584 nm (black curve) for the inverse opal prepared using 15 µL of silica precursor (the smallest amount of TEOS useful to obtain a good-quality array). The blue-shift of 114 nm compared to the calculated one is probably related with a reduction of the opal lattice period during dray. This conclusion can be deduced by looking at the SEM images in figure 6.4-a. For the inverse opal prepared using 15 µL of silica precursor, the average diameter of the voids is 312 ± 11 nm, 58 nm smaller with respect to the sphere diameter used for preparing the opal template. Hence, by substituting d with 312 nm, into equation 6.1, a photonic band gap peak of 581 nm is obtained, very close to the experimental one, which is 584 nm.
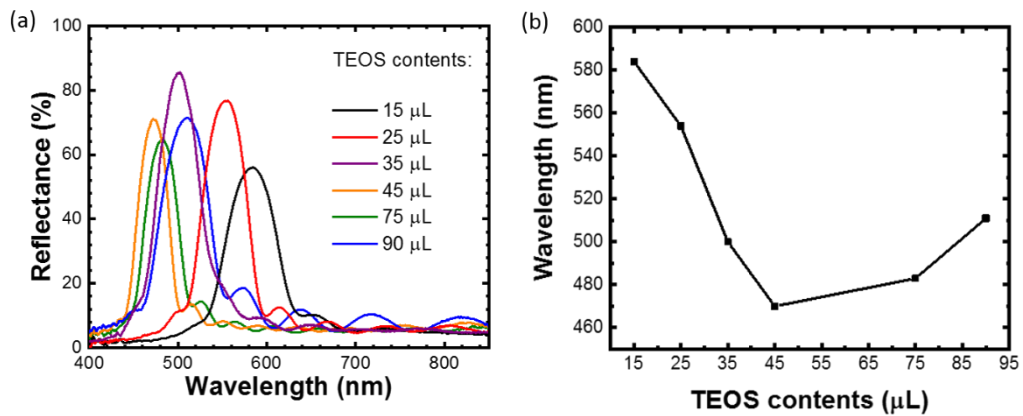
Figure 6.2. Reflectance curves of silica inverse opals prepared by varying the volume of the silica precursor, TEOS (a). Peak of the photonic band gap as a function of the TEOS contents (b).

More important, the amount of TEOS has a significant influence on the photonic band gab position. Increasing the TEOS contents from 15 µL to 45 µL, the photonic band gap shifts towards lower wavelengths by 114 nm. However, by increasing the TEOS volume over 45 µL, the refractive peak moves back to higher wavelengths compared to that of samples made with low content of TEOS. The overturning trend of the refractive peak as a function of the volume of TEOS is better appreciated in figure 6.2-b. Indeed, for colloidal solutions containing 75 µL and 90 µL of silica precursor, the photonic band gap moves to higher wavelengths reaching its peak at 483 nm and at 511 nm, respectively. The red-shift is probably due to a non-

periodic arrangement of the polystyrene spheres during the vertical deposition. In this regard, I collected the normal reflectance spectra of the inverse opals in different spots of the sample. Figure 6.3 compares the reflectance curves of two inverse opals made with 90 μL and 45 μL of silica precursor, respectively. The reflectance curves resulting from the study of the inverse opal made with 90 μL of TEOS have a profile that depends on the detected area of the sample. First of all, the photonic band gap peaks present a mismatch in wavelengths (λ_r) covering a range of 50 nm, from 470 nm to 520 nm. Additionally, the values of the intensity of reflection are strongly different, running from 45% (red curve) to 75% (orange curve). On the contrary, the inverse opal prepared with 35 μL of silica precursor have congruent reflectance curves regardless of the spot of the sample investigated. Those results prove that an excess of TEOS is deleterious for the quality of the photonic array.
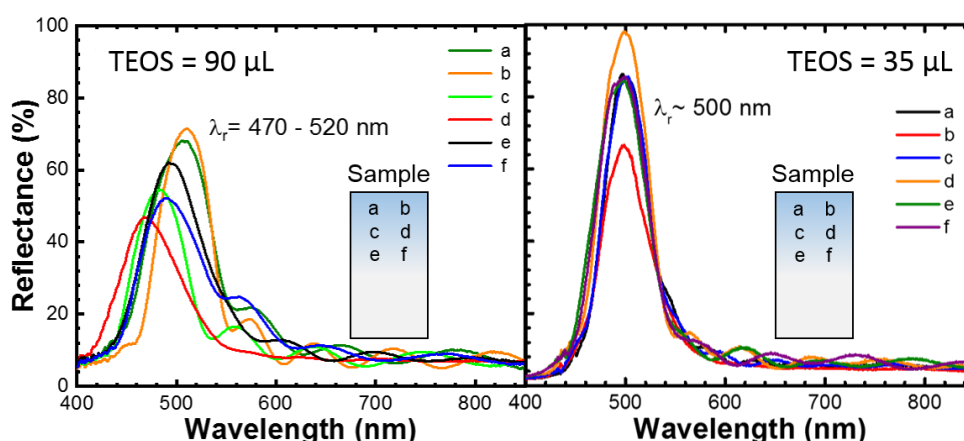
Figure 6.3. Curves of normal reflectance collected in different spots of two inverse opals prepared using a colloidal solution containing 90 μL and 35 μL of silica precursor (TEOS), respectively. The inserts are a schematic representation of the samples investigated, the letters identify the area of the inverse opals undergo examination.

Figure 6.4 compares the diameters size of the voids of inverse opals prepared with 15 μL (panel "a"), 25 μL (panel "b"), 35 μL (panel "c"), and 45 μL (panel "d"). The size of the voids (<d>) were calculated by averaging the voids diameters of the cross section of the samples visible on the SEM images in figure 6.4. It was found that the

void size of the inverse opals decrease with increasing the TEOS contents of the colloidal solution. Considering that the constant lattice *a* for an fcc array is:

$$a = 2\sqrt{2}\,\frac{d}{2} \qquad\qquad (6.2)$$

(where *d* is the void diameter), the lattice period for the inverse opals can be compared. As expected, replacing *d* with the values measured in figure 6.4, I found that the lattice constant *a* decrease as the TEOS volume is increased. More precisely, inverse opals prepared by colloidal solutions of polystyrene microparticle of 370 nm and 15 µL, 25 µL, 35 µL, and 45 µL of TEOS are characterised by an fcc array having a lattice constant of 441 nm, 407 nm, 388 nm and 371 nm, respectively (see table 6.1). Furthermore, inserting the diameter values found in figure 6.4 (considering their error) into the Bragg-Snell law (equation 6.1) the theoretical PSB peaks fit very well the experimental one (see table 6.2). This leads to the conclusion that changing the TEOS content, the PSB still follow the trend of the Bragg-Snell law.
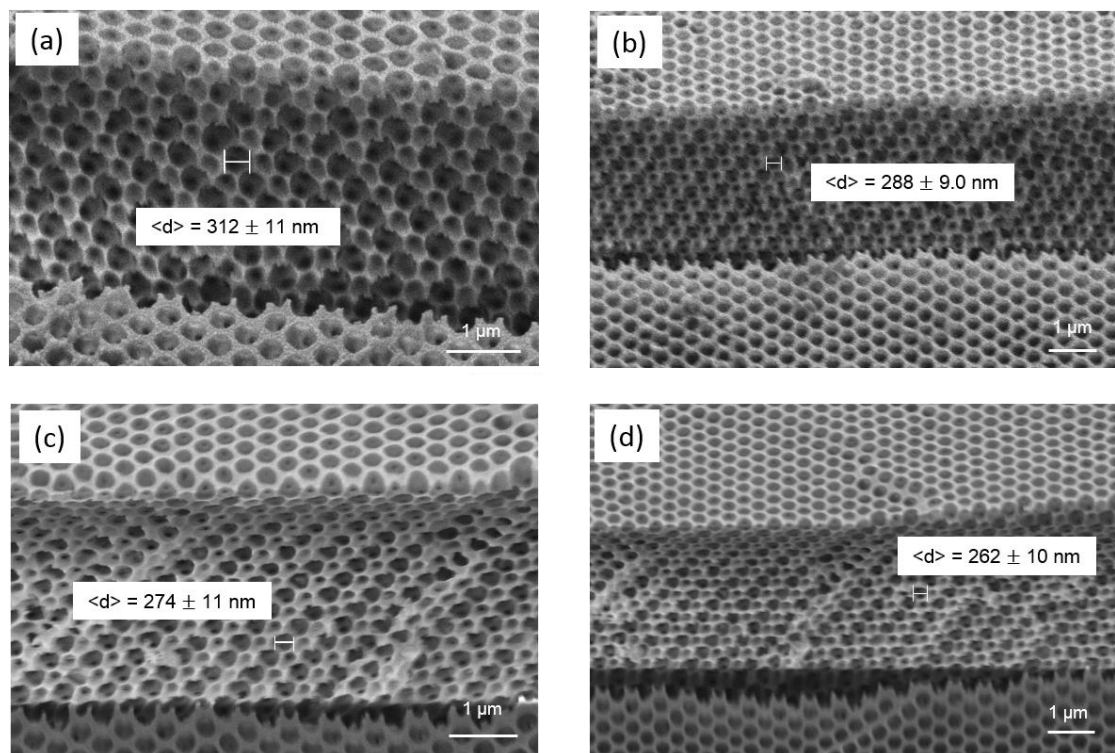

Figure 6.4. SEM images of inverse opals prepared by colloidal solution containing 15 µL (a), 25 µL (b), 35 µL (c), and 45 µL (d) of silica precursor (TEOS). For each structure the average diameter of the voids, <d>, has been measured.

TEOS contents (µm)	Voids diameter (nm)	fcc lattice constant (nm)
15 ± 1	312 ± 12	441 ± 12
25 ± 1	288 ± 9.0	407 ± 9.0
35 ± 1	274 ± 11	388 ± 11
45 ± 1	262 ± 10	371 ± 10

Table 6.1. Variation of the fcc lattice constant as a function of the contents of the silica precursor (TEOS) on the colloidal solution used for preparing inverse opals.

TEOS contents (µm)	Voids diameter (nm)	Calculated PSB peak (nm)	Experimental Reflectance peak (nm)
15 ± 1	312 ± 12	581 ± 13	584 ± 1.5
25 ± 1	288 ± 9.0	536 ± 10	554 ± 1.5
35 ± 1	274 ± 11	510 ± 12	500 ± 1.1
45 ± 1	262 ± 10	487 ± 11	470 ± 1.5

Table 6.2. Comparison between the calculated PSB peak using the Bragg-Snell, and the experimental PSB position in the normal reflectance spectra. The diameter values used were measured from the SEM images in fig. 6.4

To conclude, by simply controlling the amount of silica precursor in the vertical deposition technique it is possible to tune the photonic band gap wavelengths by over 100 nm, in SiO_2 – inverse opals. The fcc photonic structure is still highly ordered and presents different lattice constant depending on the TEOS contents.

6.4 Applications

6.4.1 Manipulation of radiative rate in silica inverse opals

The inverse opal prepared by using the vertical deposition technique were infiltrated with the green conjugated polymer Poly(4-4'-diphenylene diphenylvinylene), or briefly PDPV (see section 2.4 for further details) by drop-casting as shown in figure 6.5. More in detail, 500 µL of PDPV 5 mg/mL in toluene was dropped on top of the inverse opal and were let them infiltrate into the pours until the solvent was evaporated.
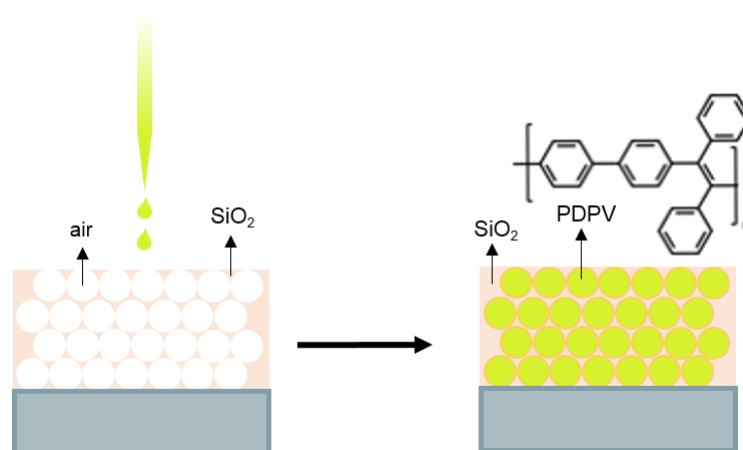
Figure 6.5. Schematic representation of the infiltration method used to fill the voids of the silica inverse opal. The picture shows also the chemical structure of the conjugated active polymer, PDPV.

In order to select the appropriate inverse opals to infiltrate, the reflectance spectra of two bare opals were plotted together with the PL spectra of a spin-coated film of PDPV, as showed in figure 6.6-a. The tuned opal has the reflectance peak at 500 nm and its curve is contained within the emission spectra of the thin-film of PDPV, orange and purple curve, respectively. On the contrary, the detuned opal (reference) is characterised by a photonic band gap peak (green curve) at 400 nm, generously distant in wavelength with respect to the PDPV emission so that it cannot affect the PDPV radiative properties. The tuned opal was prepared from a colloidal/TEOS

solution of polystyrene spheres with a diameters of 370 nm and 35 µL of silica precursor, while the detuned opal was fabricated using polystyrene spheres with a diameters of 300 nm and 45 µL of TEOS.
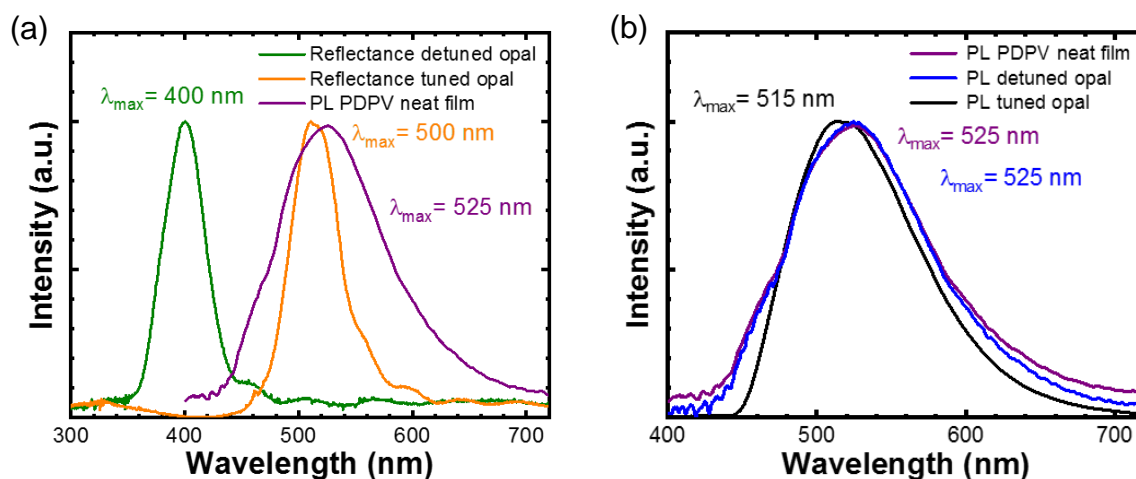
Figure 6.6. Normal reflection spectra of tuned and detuned inverse opal plotted together with the PL curve of a spin-coated film of PDPV (a); Comparison between the PL spectra of the PDPV into the inverse opals and of a PDPV spin-coated film of PDPV (b). The spectra are normalised.

Figure 6.6-b demonstrates that the PDPV infiltrated in the reference opal preserves its emission. Indeed, the photoluminescence spectrum of the infiltrated detuned opal (blue curve) overlaps with that of the PDPV spin-coated film (blue curve) all over the detected wavelengths. On the contrary, the infiltrated tuned opal has a PL spectrum (black curve) dissimilar with respect to the detuned one. Its peak is 10 nm lower in wavelengths compared to that of the reference opal, and it does not show the shoulder at 450 nm, feature of the PDPV emission. Those results prove that the variation of the PDPV spontaneous emission is not due to simple interactions between the polymer and the surface of the porous scaffold, but photonic effects take part on such modification.
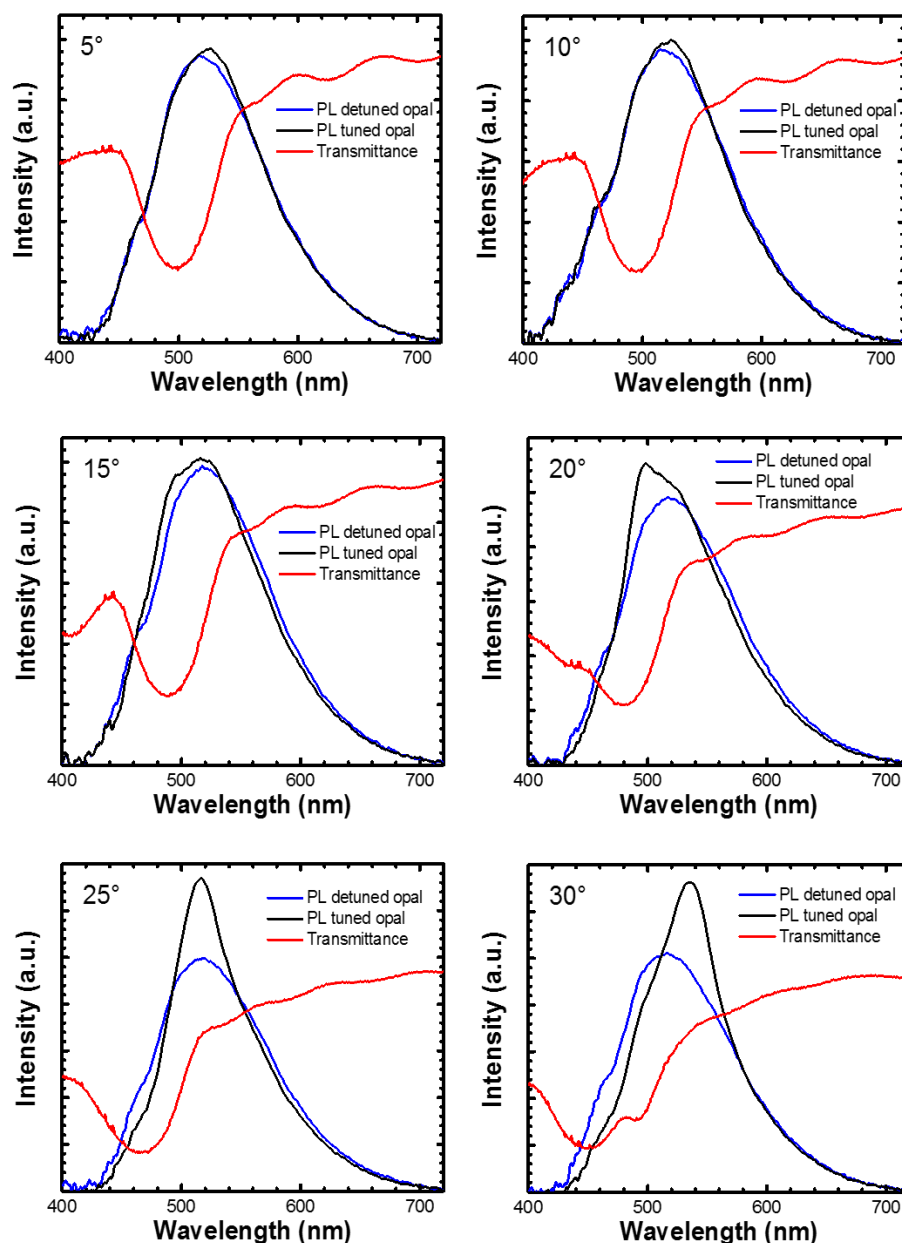
Figure 6.7. PL spectra of tuned (black curve) and detuned (blue curve) opals together with the transmittance (red curve) of the luminescent tuned opal. The PL spectra were collected by increasing the collection angle from 0° to 30°, while the transmittance spectra by increasing the angle of the incidence beam.

Figure 6.7 shows the angle-dependent PL spectra of the tuned (black curve) and detuned (blue curve) opals together with the angle-dependent transmittance (red curve) of the luminescent tuned opal. As expected, the PL of the detuned opal doesn't show any spectral modification throughout the detected angle (from 5° to 30°), while the tuned opal is characterized by a strong spectral modification especially where the

high-energy band overlaps the PL, at 20°, 25° and 30°. Photonic properties of the inverse opal induces the intensity modification of the PL spectra. More in details, the PL intensity is enhanced in correspondence to the high-wavelength edge of the photonic bands, while it is partially suppressed within the photonic band gap. The ratio between the PL spectra of tuned and detuned opals, in figure 6.8, better emphasize the enhancement and suppression effect. According to the dispersion of the photonic band structure, both the enhancement and the suppression effects depend on the detection angle inducing a directionality to the observed effect. Increasing the collection angle, the enhancement red-shift from 480 nm to 550 nm and rise in intensity up to 40 % as the high-energy band better overlap the PL spectra.
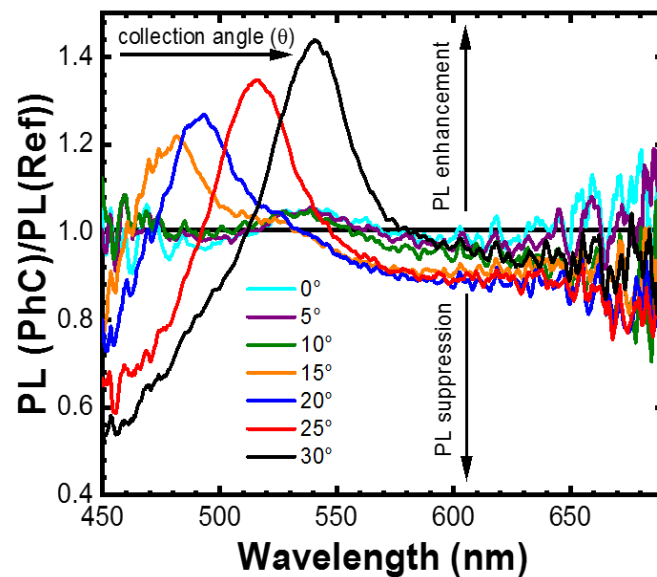
Figure 6.8. Ratio between the angle-dependent emission of the infiltrated tuned inverse opal (PhC) and the infiltrated detuned opal (reference).

To get further proofs of the photonic effect of these inverse opals on the PDPV radiative properties (i.e. radiative rate modification), I measured the PL efficiency and time-resolved PL measurements at 480 nm (where the PL enhancement is observed). There is a slight but clear increase of the PL efficiency with respect to detuned opal, In fact, the PL efficiency were measured to be 48.0 $\pm$ 0.7% for the detune opal, and 53.0 $\pm$ 2.4% for the tuned opal, (table 6.3). The PL efficiency of the detuned opal is in

agreement with the PL efficiency of PDPV solid films found in previous studies (~45%)[35,36].

Turning on the analysis of the PL-decay, both infiltrated and bare opals show bi-exponential kinetics with characteristic lifetime as reported in table 6.2. At 480 nm where the enhancement of the photoluminescence takes place, the lifetime values, τ_1, of both the detuned and tuned opals are almost the same, 0.47 ns and 0.42 ns, respectively. On the other hand, the long decay, τ_2, for the tuned opal, is sufficiently shorter compared to the τ_2 of the Ref, so that a variation of the radiative rate is observed going from detuned to tuned opals. As expected, considering the average lifetime and the PL efficiency, a modification of the radiative rate k_r from 2.30 (for the detuned opal) to 2.83 (for the tuned opal) is calculated, whereas the k_{nr} does not change significantly, which strongly support the observation of the Purcell effect. k_r and k_{nr} were calculated by using the equation 2.1 and 2.2. This effect is assigned to the variation of the density of photonic state in correspondence of the photonic band gap, as previously explained (see section 5.1.2).

Opal	λ = 480 nm – PL enhancement				
	τ_1 (ns)	%	τ_1 (ns)	%	$<\tau>$ (ns)
Detuned (Ref)	0.47 ± 0.01	34.69	2.90 ± 0.02	65.31	2.06 ± 0.01
Tuned	0.42 ± 0.01	32.96	2.59 ± 0.02	67.04	1.87 ± 0.01

Table 6.3. Lifetime (τ_1 and τ_2) and the average value $<\tau>$ for PDPV infiltrated into tuned and detuned silica inverse opals. The contribution for each lifetime is reported in percentage (%).

Opal	λ = 480 nm – PL enhancement		ϕ_{PL} (%)
	k_r (s^{-1}) x 10^8	k_{nr} (s^{-1}) x 10^8	
Detuned (Ref)	2.30 ± 0.07	2.55 ± 0.09	48.0 ± 0.7
Tuned	2.83 ± 0.15	2.52 ± 0.21	53.0 ± 2.4

Table 6.4. Values of the PL quantum efficiency (ϕ_{PL}), and of the radiative (k_r) and non-radiative (k_{nr}) constants of PDPV infiltrated into tuned and detuned inverse opals. K_r and K_{nr} were calculated by using equation 2.1 and 2.2.

6.4.2 Silica inverse opals for bio-sensing applications

3D photonic crystals and above all inverse opals span different area of technological application, such as optoelectronics, energy storage, and tissue engineering. Among others, a fashionable field of application where inverse opals are preferred with respect to other porous scaffold is sensors and bio-sensors. In this regard, my silica inverse opals where exploited as bio-sensor for monitoring bovine serum albumin (BSA) by using a technique namely interferogram average over wavelength reflectance spectroscopy (IAWRS). The experiments were carried out in the group of Prof. Barillaro in Pisa (Dipartimento di Ingegneria dell'Informazione, Università di Pisa, Italy), and the results where kindly shared with us giving the permission to report them on this chapter.

The popularity of inverse opals is due to their uniform and interconnected pores together with the reproducibility of their physical properties across different batches. Moreover, the dependence of the reflectance peak on the refractive index contrast between the PhCs materials (generally the porous matrix and the voids) makes inverse opals easy bio-sensors to monitor. However, most of the measurements performed in bio-sensing require water-based media which dramatically reduce the refractive index contrast and consequently decrease the ability to detect low concentration of analyte by tracking the reflection peak. Hence, to get all the best from inverse opals the alternative technique IAWRS come into play. This strategy of signal processing is based on the calculation of the average value over wavelength of spectral interferograms, obtained by subtracting (wavelength by wavelength) the reflection spectra of BSA infiltrated into the inverse opal from a reference reflection spectrum recorded in solely buffer (i.e. Acetate). In addition, IAWRS allows to reliably detect down to 100 pM of BSA without any label or signal amplification [77].
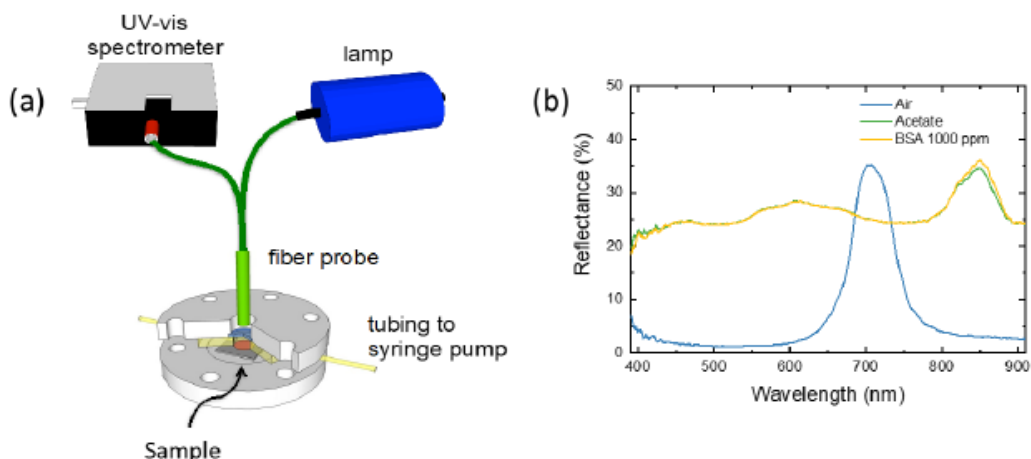
Figure 6.9. Schematic representation of the set-up used to infiltrate and characterised invers opals. The sample is located in a flow-cell connected with the reflectance probe and with a syringe pump for the flowing of the buffer and the analytes (a). Reflectance spectra of the inverse opals in air (blue line) and of the same sample into the flow-cell and infiltrated with the acetate buffer (green line) and with 1000 ppm of BSA (yellow line).

Silica inverse opals (see session 6.2.1 for the preparation technique), were first infiltrated with an acetate buffer (10 mM CH3COONa/CH3COOH and 100 mM NaCl in DI water, pH=4.7) and then with a BSA solution at rate of 20 µL/min for 30 minutes. After that the reference spectra were collected to verify the presence of the BSA in the scaffold. The solutions of bovine serum albumin was prepared in acetate buffer in different concentration, from 100 ppm (1.5 µM) to 1000 ppm (15 µM). Figure 6.9-a show the set-up used to perform the optical measurement. The reflectance probes connected to the lamp and the detector converge into a flow-cell that contain the sample and that is connected to a syringe pump for the injection of the analyte.

Figure 6.9-b shows the optical behaviour of inverse opals in air and into the flow-cell. The blue curve centred at 710 nm correspond to the photonic band gap of the bare PhC collected in air, while the green and the yellow curve are the reflection spectra of the inverse opal after the injection of acetate (reference) and the BSA (analyte), respectively. The reference spectrum has a photonic band gap higher in wavelength (at 853 nm) with respect to that of the bare opal due to a decreased refractive index contrast. This result is supported by the wavelength value calculated

by using the Bragg-Snell law (see equation 6.1). Considering the void diameters d = 380 nm, the refractive index for acetate and silica n_1 = 1.34 and n_2 = 1.47, respectively, and f_v = 0.74 and $(1 - f_v)$ = 0.26 for an ideal fcc-lattice, the peak of the photonic band gap is estimated to be 851 nm, only 2 nm lower with respect to the measured one. On the other hand, the BSA reflection spectra shows a slight but clear red-shift in wavelengths (reflectance peak at 857 nm) and increase in intensity with respect to the reference spectra. Those change is due to the BSA accumulation on the inverse opals microporous.
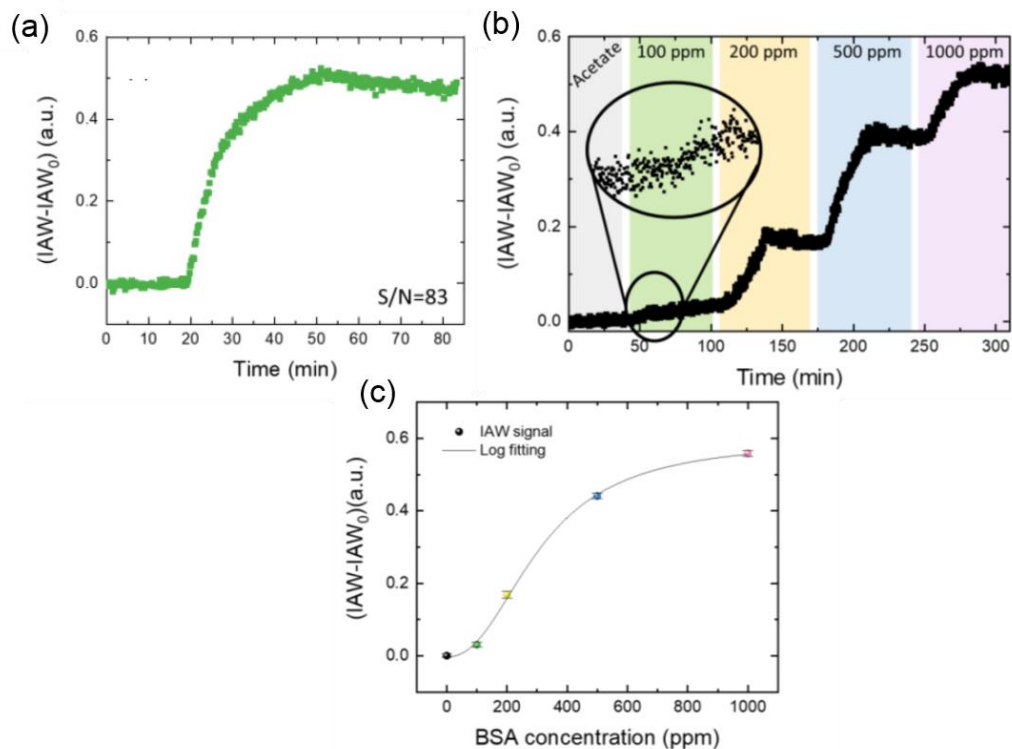
Figure 6.10. Time resolved IAW- IAW0 signal upon injection of BSA 1000 ppm. The signal-to-noise ratio is 83 (a). Time resolved IAW- IAW0 value for different concentration of BSA, 100 ppm (green sector), 200 ppm (yellow sector), 500 ppm (blue sector), and 1000 (ppm pink sector) (b). Fitting of the IAW- IAW0 values as a function of the BSA concentrations (c).

In order to bring to light the potential of inverse opals as efficient biosensors, the IAWRS signal processing strategy were used to evaluate the infiltration of the BSA inside the PhC. In figure 6.10 is reported the signal of BSA-infiltrated opal subtracted the signal of the reference (IAW- IAW_0) as a function of the injection time. The signal from 0 to 20 minutes is referred to the acetate buffer before the injection, the signal

from 20 to 60 minutes is referred to the injection of the BSA solution (solution concentration: 1000 ppm, rate of injection: 20 μL/min), and the signal between and 60 and 80 minutes is due to the rising step (acetate buffer was injected at a rate of 100 μL/min to remove any excess of analyte). Additionally, in figure 6.10-b the IAW- IAW_0 signal for different BSA concentration (from 100 ppm to 1000 ppm) is reported. In the grey sector the inverse opal were filtered with the acetate buffer until the collected signal was stable. Hence, the BSA solution was injected with a concentration of 100 ppm (green sector), 200 ppm (yellow sector), 500 ppm (blue sector) and 1000 ppm (pink sector), followed by a rising step with acetate buffer. For each BSA injection correspond a step in the signal demonstrating a fast response (10-20 min) of inverse opals to the presence of the analyte. Finally, the IAW- IAW_0 data were plotted in figure 6.10-c as a function of the BSA concentration and fitted with a sigmoidal function which match with the curves found in other experiments of bio-accumulation sensing.

The reported results confirm that inverse opals are competitive platform for bio-sensing, compared to other porous system. Thanks to their robust and well-defined porosity, inverse opals show a fast response in detecting analyte typical of biological systems. In conclusion, it has been demonstrate, once again, the efficiency of the developed vertical deposition as a technique used for the fabrication of silica inverse opals.

Chapter 7. Conclusions

In photonic crystals a complete understanding of the density of quantum states is the key for an accurate control of the optical properties of fluorescent molecules they host. The spontaneous emission of active materials can be in fact completely or partially suppressed by tailoring the density of states in correspondence of the photonic stop band of self-assembled structures [1,6,7,12,78]. Typically, in addition to the photonic stop band, face-centred cubic (fcc) photonic crystals also show photonic bands that result from the combination of complex diffraction phenomena [61,62]. Those are called high-energy photonic bands because of their position in the reflectance spectra with respect to the photonic stop band. Both photonic stop band and high-energy bands influence the emission of embedded active materials. However, the latter are expected to have a much higher impact due to a stronger variation of their density of states. An even better control of the spontaneous emission requires a high degree of order of the photonic structure. This is why the scientific community has intensively studied various self-assemble techniques for realising fluorescent photonic crystals with structural long-range order [73,74,79]. The co-growth of active materials and colloidal microparticles via vertical deposition is the self-assembly approach that guarantees superior crystalline quality of 3D photonic structures [72]. In the research project presented in this thesis, such technique is applied for achieving state of the art crystalline qualities of both direct and inverse opals.

In the first part of the thesis, I presented the benefits of the vertical deposition for the incorporation of a water-soluble polyrotaxane dye ($PDV_{10}Li \subset \beta - CD$) inside opals. The photoluminescence properties of this combined system are studied in correspondence of the photonic stop band and of the high-energy bands. The full

overlap of photonic bands in the reflectance spectra of the bare and luminescent opals proves that the fcc structure are preserved even after the incorporation of polyrotaxane. Since polyrotaxanes are sizeable molecules, their inclusion within the small voids of opals can be challenging [59]. In this context the results here presented demonstrate the power of the vertical deposition as a method for preparing fluorescent opals. The efficiency of this fabrication technique is underlined by the strong angle-dependent spontaneous emission of polyrotaxane. In particular the photoluminescence is suppressed within both the photonic stop band and the photonic high-energy bands, while it is enhanced at high-energy edge of the photonic stop band.

Self-assembling methods are the most affordable and they offer useful properties for various technological applications. However, the use of direct opals is limited by the small photonic interaction strength (only a pseudo photonic stop band is available). The most significant application of self-assembled structures is in the production of templates for high-refractive index materials, namely inverse opals, which have the potential to produce a full photonic stop band [75]. In this work, silica inverse opals are prepared firstly by incorporating the silica precursor TEOS (tetraethoxy silane) between the interparticle voids of the direct opals, and secondly by the thermal removal of the sacrificial template. More specifically, the TEOS incorporation takes place simultaneously to the growth of the direct opal. This method allows to tune the photonic band gap wavelengths up to 100 nm in silica inverse opals by simply controlling the amount of the silica precursor. The obtained fcc photonic structure is still highly ordered with the advantage of presenting different lattice constants depending on the TEOS amount. Additionally, in order to verify the effectiveness of such new method in tailoring the position of the photonic stop band, I implemented inverse opals as light manipulators and bio-sensors. After infiltration by dip-coating of the polymeric dye PDPV into the photonic structure, I observed a significant photonic control of the radiative rate and lifetime of the polymer in

correspondence of an enhancement of the photoluminescence. Moreover, inverse opals show a fast response in detecting analyte as bovine serum albumin. This confirms that co-growth inverse opals are also competitive for bio-sensing.

The results presented in this thesis demonstrate the resourceful versatility of the vertical deposition technique for producing infiltrated opals. This very same technique is indeed suitable both for direct opals fabrication and for inverse opals preparation. In the former for incorporating the luminescent materials [59], in the latter for the incorporation of high-refractive index materials [71]. All this achieved in just a single step of fabrication of the final structure, with the advantage of avoiding defects which could arise in multi-steps fabrication techniques. This is well known. The novelty of the work presented in this thesis can be summarised by the following distinct manners for exploiting such single-step co-growth technique: (i) for direct opals, I investigated the effect of the high-energy bands, which signal the high degree of order of the opal, on the spontaneous emission of polyrotaxane; (ii) for inverse opals, benefitting of the co-growth methods in ref. [71], I discovered that it is possible to tune the position of the photonic stop band by varying the lattice constant of the opal. The results achieved in controlling the optical properties of the photonic crystals promise to have important implications in light engineering and telecommunications [9,72]. This can deliver a widespread technological impact on optoelectronics, (bio)sensors and much more. The advantage of this technique is also likely to impact the new frontier of biopolymer-based photonic structures which are extensively implemented in the biomedical industry [80,81].

References

1 J. D. Joannopoulos, S. G. Johnson, J. N. Winn & Meade, R. D. *Photonic Crystals Molding the Flow of Light.* (Princeton University Press, 2007).

2 Tregnago, G. *Photophysics and applications of organic semiconductors* Doctor of Philosophy thesis, Univerity College London (UCL), (2015).

3 Teyssier, J., Saenko, S. V., van der Marel, D. & Milinkovitch, M. C. Photonic crystals cause active colour change in chameleons. *Nat Commun* **6**, 6368, doi:10.1038/ncomms7368 (2015).

4 J. Sun, B. Bhushan & Tonga, J. Structural coloration in nature. *RSC Advanced* **3**, 14862, doi:10.1039/C3RA41096J (2013).

5 Kinoshita, S., Yoshioka, S. & Miyazaki, J. Physics of structural colors. *Reports on Progress in Physics* **71**, 076401, doi:10.1088/0034-4885/71/7/076401 (2008).

6 John, S. Strong localization of photons in certain disordered dielectric superlattices. *Phys Rev Lett* **58**, 2486, doi:10.1103/PhysRevLett.58.2486 (1987).

7 Yablonovitch, E. Inhibited spontaneous emission in solid-state physics and electronics. *Phys Rev Lett* **58**, 2059, doi:10.1103/PhysRevLett.58.2059 (1987).

8 Wu, S., Xia, H., Xu, J., Sun, X. & Liu, X. Manipulating Luminescence of Light Emitters by Photonic Crystals. *Adv Mater* **30**, e1803362, doi:10.1002/adma.201803362 (2018).

9 Aguirre, C. I., Reguera, E. & Stein, A. Tunable Colors in Opals and Inverse Opal Photonic Crystals. *Advanced Functional Materials* **20**, 2565, doi:10.1002/adfm.201000143 (2010).

10 Peter Lodahl *et al.* Controlling the dynamics of spontaneous emission from quantum dots by photonic crystals. *Nature* **430**, 654, doi:https://doi.org/10.1038/nature02772 (2014).

11 Felici, M. *et al.* Broadband enhancement of light-matter interaction in photonic crystal cavities integrating site-controlled quantum dots. *Physical Review B* **101**, 205403, doi:10.1103/PhysRevB.101.205403 (2020).

12 Comoretto, D. *Organic and Hybrid Photonic Crystals.* 3 (Springer, 2015).

13 Sakoda, K. *Optical Properties of Photonic Crystals.* (Springer, 2001).

14 Kragh, H. The Lorenz-Lorentz Formula: Origin and Early History. *Substantia* **2**, 7, doi:10.13128/substantia-56 (2018).

15 M. T. Bernius, M. Inbasekaran & Wu, W. Progress with light-emitting polymers. *Advanced Materials* **12**, 1737, doi:0935-9648/00/2312-1738 (2000).

16   J. H. Burroughes *et al.* Light-emitting diodes based on conjugated polymers. *Nature* **347**, 539, doi:https://doi.org/10.1038/347539a0 (1990).

17   Tang, C. W. & VanSlyke, S. A. Organic electroluminescent diodes. *Applied Physics Letters* **51**, 913, doi:https://doi.org/10.1063/1.98799 (1998).

18   Li, G., Zhu, R. & Yang, Y. Polymer solar cells. *Nature Photonics* **6**, 153, doi:https://doi.org/10.1038/nphoton.2012.11 (2012).

19   Tang, C. W. Two-layer organic photovoltaic cell. *Applied Physics Letters* **48**, 183, doi: https://doi.org/10.1063/1.96937 (1998).

20   Muccini, M. A bright future for organic transistors. *Nature Materials* **5**, 605, doi:https://doi.org/10.1038/nmat1699 (2006).

21   Horowitz, G. Organic Field-Effect Transistors. *Advanced Materials* **10**, 365, doi:0935-9648/98/0503-0365 (1998).

22   O'Carroll, D. M. *et al.* Conjugated polymer-based photonic nanostructures. *Polymer Chemistry* **4**, 5181, doi:https://doi.org/10.1039/C3PY00198A (2013).

23   Chiang, C. K. *et al.* Electrical Conductivity in Doped Polyacetylene. *Physical Review Letters* **39**, 1472, doi:https://doi.org/10.1103/PhysRevLett.39.1098 (1977).

24   Schols, S. *Device Architecture and Materials for Organic Light-Emitting Devices*. (Springer Science + Business Media, 2011).

25   W.R. Salaneck, R.H. Friend & Das, J. L. B. Electronic structure of conjugated polymers: consequences of electron-lattice coupling *Physics Reports* **319**, 231, doi:https://doi.org/10.1016/S0370-1573(99)00052-6 (1999).

26   Barford, W. *Electronic and optical properties of conjugated polymers*. (Clarendon press, 2005).

27   M. Pope & Swemberg, C. E. *Electronic Processes in Organic Crystals and Polymers*. (Oxford Science Publications, 1999).

28   S. E. Debebe *et al.* Synthesis and Optical and Transport Properties of a Phenyl-Substituted Polythiophene. *Journal of Polymer science part A* **49**, 2693, doi:10.1002/pola.24701 (2011).

29   Y. Zhu, M. M. Alam & Jenekhe, S. A. Regioregular Head-to-Tail Poly(4-alkylquinoline)s: Synthesis, Characterization, Self-Organization, Photophysics, and Electroluminescence of New n-Type Conjugated Polymers. *Macromolecules* **36**, 8959, doi:10.1021/ma0348021 (2003).

30   T. Chen, X. Wu & Rieke, R. D. Regiocontrolled Synthesis of Poly(3-alkylthiophenes) Mediated by Rieke Zinc: Their Characterization and Solid-State Properties. *J. Am. Chem. Soc.* **117**, 233, doi:0002-7863/95/1517-0233 (1994).

31   Fraiji, L. K., Hayes, D. M. & Werner, T. C. Static and Dynamic Fluorescence Quenching Experiments for the Physical Chemistry Laboratory. *Journal of Chemical Education* **69**, 424, doi:https://doi.org/10.1021/ed069p424 (1992).

32   Lakowicz, J. R. & Weber, G. Quenching of Fluorescence by Oxygen. A Probe for Structural Fluctuations in Macromolecules. *Biochemistry* **12**, 4161, doi:https://doi.org/10.1021/bi00745a020 (1973).

33   Siddiqui, S. & Spano, F. C. H- and J-aggregates of conjugated polymers and oligomers A theoretical investigation. *Chemical Physics Letters* **308**, 99, doi:https://doi.org/10.1016/S0009-2614(99)00577-1 (1999).

34   Feast, W. J. *et al.* Optical absorbtion and luminescence in poly(4-4' - diphenylene diphenylenevinylene). *Synthetic Metals* **10**, 181, doi:https://doi.org/10.1016/0379-6779(85)90189-4 (1985).

35   Cacialli, F. *et al.* Efficient green light-emitting diodes from a phenylated derivative of poly(p-phenylene–vinylene). *Appl. Phys. Lett.* **69**, 3794, doi:https://doi.org/10.1063/1.117001 (1996).

36   Winroth, G., Brovelli, S., Daik, R., James Feast, W. & Cacialli, F. Stability of optical and electroluminescence properties of a semiconducting polymer over a decade. *Organic Electronics* **11**, 1445, doi:https://doi.org/10.1016/j.orgel.2010.06.012 (2010).

37   Brovelli, S. *et al.* White luminescence from single-layer devices of nonresonant polymer blends. *Appl. Phys. Lett.* **96**, 213301, doi: https://doi.org/10.1063/1.3387816 (2010).

38   T. Aida, E. W. Meijer & Stupp, S. I. Functional Supramolecular Polymers. *Science* **335**, 813, doi:10.1126/science.1205962 (2012).

39   V. Balzani, A. Credi & Venturi, M. *Molecular devices and machines*. Vol. 2 (2007).

40   A. Credi & Balzani, V. *Le macchine molecolari*. (2018).

41   R. H. Friend *et al.* Electroluminescence in conjugated polymers. *Nature* **397**, 121, doi:https://doi.org/10.1038/16393 (1999).

42   S., R. F. The path to ubiquitous and low-cost organic electronic appliances on plastic. *Nature* **428**, 911, doi:https://doi.org/10.1038/nature02498 (2004).

43   Samuel I. D. W. & A., T. G. Organic Semiconductor Lasers *Chemical Reviews* **107**, 1272, doi:https://doi.org/10.1021/cr050152i (2007).

44   Sauvage, J.-P. & Dietrich-Buchecker, C. *Molecular Catenanes, Rotaxanes and Knots. A journey Through the World of Molecular Topology.*, (WILE-VCH, 1999).

45   Toshikazu, T. Polyrotaxane and Polyrotaxane Network: Supramolecular Architectures Based on the Concept of Dynamic Covalent Bond Chemistry. *Polymer Journal* **38**, 1, doi:https://doi.org/10.1295/polymj.38.1 (2006).

46   Brovelli, S. *et al.* Ultra-broad optical amplification and two-colour amplified spontaneous emission in binary blends of insulated molecular wires. *Adv Mater* **22**, 3690, doi:10.1002/adma.201000895 (2010).

47   A. Petrozza *et al.* Control of Rapid Formation of Interchain Excited States in Sugar-Threaded Supramolecular Wires. *Adv Mater* **20**, 3218, doi:10.1002/adma.200800007 (2008).

48   S. Brovelli *et al.* Tuning Intrachain versus Interchain Photophysics via Control of the Threading Ratio of Conjugated Polyrotaxane. *Nano Lett.* **8**, 4546, doi:https://doi.org/10.1021/nl802775a (2008).

49   Cacialli, F. *et al.* Cyclodextrin-threaded conjugated polyrotaxanes as insulated molecular wires with reduced interstrand interactions. *Nat Mater* **1**, 160, doi:10.1038/nmat750 (2002).

50   Lopez, C. Materials Aspect of Photonic Crystals. *Advanced Materials* **15**, 1679, doi: https://doi.org/10.1002/adma.200300386 (2003).

51   Rybin, M. V. *et al.* Fano resonance between Mie and Bragg scattering in photonic crystals. *Phys Rev Lett* **103**, 023901, doi:10.1103/PhysRevLett.103.023901 (2009).

52   Pasquazi, A. *et al.* In situ tuning of a photonic band gap with laser pulses. *Applied Physics Letters* **93**, 091111, doi:10.1063/1.2977998 (2008).

53   Nikolaev, I. S., Lodahl, P. & Vos, W. L. Quantitative analysis of directional spontaneous emission spectra from light sources in photonic crystals. *Physical Review A* **71**, 053813, doi:10.1103/PhysRevA.71.053813 (2005).

54   Barth, M., Gruber, A. & Cichos, F. Spectral and angular redistribution of photoluminescence near a photonic stop band. *Physical Review B* **72**, 085129, doi:10.1103/PhysRevB.72.085129 (2005).

55   Morandi, V., Marabelli, F., Amendola, V., Meneghetti, M. & Comoretto, D. Colloidal Photonic Crystals Doped with Gold Nanoparticles: Spectroscopy and Optical Switching Properties. *Advanced Functional Materials* **17**, 2779, doi:10.1002/adfm.200600764 (2007).

56   P. Lodahl *et al.* Controlling the dynamics of spontaneous emission from quantum dots by photonic crystals. *Nature* **430**, 654, doi: https://doi.org/10.1038/nature02772 (2004).

57   L. Berti, M. C., F. Di Stasio, D. Comoretto, M. Galli, F. Marabelli, N. Manfredi, C. Marinzi, and A. Abbotto. Spectroscopic Investigation of Artificial Opals Infiltrated with a Heteroaromatic Quadrupolar Dye. *J. Phys. Chem. C* **114**, doi:https://doi.org/10.1021/jp906002q (2010).

58 E. P. Petrov, V. N. B., I. I. Kalosha, and S. V. Gaponenko. Spontaneous Emission of Organic Molecules Embedded in a Photonic Crystal. *PHYSICAL REVIEW LETTERS* **81**, doi:https://doi.org/10.1103/PhysRevLett.81.77 (1998).

59 Di Stasio, F. *et al.* Fluorescent polystyrene photonic crystals self-assembled with water-soluble conjugated polyrotaxanes. *APL Materials* **1**, 042116, doi:10.1063/1.4826544 (2013).

60 Míguez, H., Kitaev, V. & Ozin, G. A. Band spectroscopy of colloidal photonic crystal films. *Applied Physics Letters* **84**, 1239-1241, doi:10.1063/1.1644913 (2004).

61 Pavarini, E. *et al.* Band structure and optical properties of opal photonic crystals. *Physical Review B* **72**, 045102, doi:10.1103/PhysRevB.72.045102 (2005).

62 Galisteo-López, J. F. & López, C. High-energy optical response of artificial opals. *Physical Review B* **70**, 035108, doi:10.1103/PhysRevB.70.035108 (2004).

63 Wostyn, K. *et al.* Optical properties and orientation of arrays of polystyrene spheres deposited using convective self-assembly. *The Journal of Chemical Physics* **118**, 10752, doi:10.1063/1.1573173 (2003).

64 Romanov, S. G. *et al.* Diffraction of light from thin-film polymethylmethacrylate opaline photonic crystals. *Phys Rev E Stat Nonlin Soft Matter Phys* **63**, 056603, doi:10.1103/PhysRevE.63.056603 (2001).

65 Lukosz, W. Theory of optical-environment-dependent spontaneous-emission rates for emitters in thin layers. *Physical Review B* **22**, 3030, doi:10.1103/PhysRevB.22.3030 (1980).

66 B. Fuhrmann, H. S. L., H.-R. Höche, L. Schubert, P. Werner, U. Gösele. Array of Silicon Nanowires Produced by Nanosphere Lithography and Molecular Beam Epitaxy. *Nano Lett.* **5**, 2524, doi:https://doi.org/10.1021/nl051856a (2005).

67 A.S. Dimitrov & Nagayama, K. Continuous Convective Assembling of Fine Particles into Two-Dimensional Array on Solid Surface. *Langmuir* **12**, 1303, doi:https://doi.org/10.1021/la9502251 (1996).

68 Wiesmann, C., Bergenek, K., Linder, N. & Schwarz, U. T. Photonic crystal LEDs - designing light extraction. *Laser & Photonics Review* **3**, 262, doi:10.1002/lpor.200810053 (2009).

69 Tang, C. W. Two-layer organic photovoltaic cell. *Applied Physics Letters* **48**, 183, doi:10.1063/1.96937 (1986).

70 Mishchenko, L., Hatton, B., Kolle, M. & Aizenberg, J. Patterning hierarchy in direct and inverse opal crystals. *Small* **8**, 1904, doi:10.1002/smll.201102691 (2012).

71 Hatton, B., Mishchenko, L., Davis, S., Sandhage, K. H. & Aizenberg, J. Assembly of large-area, highly ordered, crack-free inverse opal films. *PNAS* **107**, 1, doi:10.1073/pnas.1000954107/-/DCSupplemental (2010).

72	Armstrong, E. & O'Dwyer, C. Artificial opal photonic crystals and inverse opal structures – fundamentals and applications from optics to energy storage. *Journal of Materials Chemistry C* **3**, 6109-6143, doi:10.1039/c5tc01083g (2015).

73	Kassim, S., Padmanabhan, S., McGrath, J. & Pemble, M. E. Preparation and Properties of Silica Inverse Opal via Self-Assembly. *Applied Mechanics and Materials* **699**, 318, doi:10.4028/www.scientific.net/AMM.699.318 (2014).

74	Galisteo-Lopez, J. F. *et al.* Self-assembled photonic structures. *Adv Mater* **23**, 30, doi:10.1002/adma.201000356 (2011).

75	Palacios-Lidón, E. *et al.* Optical study of the full photonic band gap in silicon inverse opals. *Applied Physics Letters* **81**, 4925, doi:https://doi.org/10.1063/1.1530752 (2002).

76	J. C. de Mello, H. F. Wittmann & Friend, R. H. An Improved Experimental Determination of External Photoluminescence Quantum Efficiency. *Adv. Mater.* **9**, 230, doi:10.1002/adma.19970090308 (1997).

77	Mariani, S., Strambini, L. M. & Barillaro, G. Femtomole Detection of Proteins Using a Label-Free Nanostructured Porous Silicon Interferometer for Perspective Ultrasensitive Biosensing. *Anal Chem* **88**, 8502-8509, doi:10.1021/acs.analchem.6b01228 (2016).

78	J.D. Joannopoulos, Pierre R. Villeneuve & Fan, S. Photonic crystals: putting a new twist on light. *Nature* **386** (1997).

79	von Freymann, G., Kitaev, V., Lotsch, B. V. & Ozin, G. A. Bottom-up assembly of photonic crystals. *Chem Soc Rev* **42**, 2528, doi:10.1039/c2cs35309a (2013).

80	Wu, P., Wang, J. & Jiang, L. Bio-inspired photonic crystal patterns. *Materials Horizons* **7**, 338, doi:10.1039/c9mh01389j (2020).

81	Xiong, R. *et al.* Biopolymeric photonic structures: design, fabrication, and emerging applications. *Chem Soc Rev* **49**, 983, doi:10.1039/c8cs01007b (2020).